

RICE UNIVERSITY

Enhanced sampling and applications in protein folding

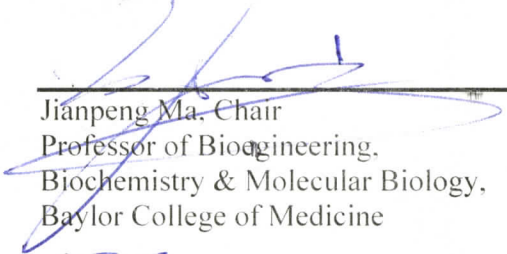
by

Cheng Zhang

A THESIS SUBMITTED
IN PARTIAL FULFILLMENT OF THE
REQUIREMENTS FOR THE DEGREE

Doctor of Philosophy

APPROVED, THESIS COMMITTEE



Jianpeng Ma, Chair
Professor of Bioengineering,
Biochemistry & Molecular Biology,
Baylor College of Medicine



Oleg Igoshin
Assistant Professor of Bioengineering



James McNew
Associate Professor of Biochemistry and
Cell Biology

HOUSTON, TEXAS
December, 2012

Reproduced in part from Cheng Zhang and Jianpeng Ma, *Enhanced sampling and applications in protein folding in explicit solvent*, J. Chem. Phys. (2010) **132**, 244101. Copyright © 2010 American Institute of Physics.

Reproduced in part from Cheng Zhang and Jianpeng Ma, *Folding helical proteins in explicit solvent using dihedral-biased tempering*, Proceedings of the National Academy of Sciences (2012) **109**, 8139-8144.

Reproduced in part from Cheng Zhang and Jianpeng Ma, *Estimating statistical distributions using an integral identity*, J. Chem. Phys. (2012) **136**, 204113.
Copyright © 2010 American Institute of Physics.

ABSTRACT

Enhanced sampling and applications in protein folding

by

Cheng Zhang

We show that a single-copy tempering method was useful in protein-folding simulations of large scale and high accuracy (explicit solvent, atomic representation, and physics-based potential). The method used a runtime estimate of the average potential energy from an integral identity to guide a random walk in the continuous temperature space. It was used for folding three mini-proteins, trpzip2 (PDB ID: 1LE1), trp-cage (1L2Y), and villin headpiece (1VII) within atomic accuracy.

Further, with a dihedral bias potential added on the roof temperature, the method was able to fold four larger helical proteins: α_3D (2A3D), α_3W (1LQ7), Fap1-NR $_{\alpha}$ (2KUB) and S-836 (2JUA).

We also discuss how to optimally use simulation data through an integral identity. With the help of a general mean force formula, the identity makes better use of data collected in a molecular dynamics simulation and is more precise than the common histogram approach.

ACKNOWLEDGMENTS

I thank Dr. Jianpeng Ma and members of the Ma lab for support.

I thank the members of the thesis committee, Drs. Jianpeng Ma, Oleg Igoshin and James McNew for guiding the thesis process. I also thank Drs. Jianpeng Ma, Oleg Igoshin and Bruce Johnson for guiding the previous master thesis.

I thank Drs. Michael Deem, Thomas Woolf, John Straub, Michael Shirts, Thomas Truskett, and Montgomery Pettitt for helpful discussions.

The computations were done on several computer clusters, the Shared University Grid at Rice (SUG@R) funded by NSF under Grant EIA-0216467, a 2010 IBM Shared University Research (SUR) Award on IBM's Power7 high performance cluster (BlueBioU) to Rice University, the Cyberinfrastructure for Computational Research (STIC) funded by NSF under Grant CNS-0821727, and the National Science Foundation through TeraGrid resources provided by Texas Advanced Computing Center under grant number TG-MCB100013. The computing resources were gratefully acknowledged.

Uses of the programs GROMACS [1-4], Visual Molecular Dynamics (VMD) [5] and other software are gratefully acknowledged.

CONTENTS

Acknowledgments	iv
Contents	v
List of Figures	ix
List of Tables	xii
Background	1
1.1. Statistical mechanics	1
1.1.1. Configuration, weight, and ensemble	2
1.1.2. Microcanonical ensemble.....	3
1.1.3. Canonical ensemble.....	3
1.1.4. Discussions.....	4
1.1.5. Two-dimensional Ising model.....	5
1.2. Molecular dynamics	6
1.2.1. Integrator	7
1.2.1.1. Leapfrog	7
1.2.1.2. Velocity-Verlet	8
1.2.2. Molecular force field	8
1.2.3. Periodic boundary condition	10
1.2.4. Potential cutoff	11
1.2.5. Ewald sum.....	11
1.2.6. Thermostat	13
1.3. Monte-Carlo simulation	14
1.3.1. Metropolis algorithm.....	14
1.3.2. Ergodicity	15
1.3.3. Detailed balance	15
1.3.4. Balance.....	16
1.4. Tempering	16

1.4.1. Parallel tempering	16
1.4.2. Simulated tempering	17
1.4.3. Realizing temperature change.....	18
1.5. Protein	18
1.5.1. Amino acid	19
1.5.2. Charge.....	19
1.5.3. Chirality.....	20
A continuous tempering	21
2.1. Introduction.....	21
2.2. Method.....	22
2.2.1. The procedure	23
2.2.2. A continuous temperature ensemble.....	25
2.2.3. Unbiased estimate of a partition function	27
2.2.4. Estimators based on integral identities.....	29
2.2.5. Adaptive averaging	31
2.3. Verification	32
2.4. Applications	35
2.4.1. Trpzip-2	36
2.4.2. Trp-cage	41
2.4.3. Villin headpiece.....	44
2.5. Conclusions and Discussions	48
2.6. Appendix.....	49
2.6.1. Fokker-Planck equation	49
2.6.2. Alternative fitting-based estimator	50
2.6.3. Overall temperature distribution	51
Folding helical proteins	52
3.1. Introduction.....	52
3.2. Dihedral-biased tempering.....	53

3.3. Results	54
3.3.1. Overview of folding of helical proteins	54
3.3.2. Geometry of parallel helix bundles	57
3.3.3. α_3D	57
3.3.4. α_3W	61
3.3.5. S-836	63
3.4. Conclusions.....	67
3.5. Appendix.....	68
3.5.1. Dihedral-biased tempering.....	68
3.5.1.1. Tempering with a bias potential	68
3.5.1.2. Dihedral bias	69
3.5.1.3. Adjusting dihedral modes	73
3.5.2. Performance of the dihedral-biased tempering.....	76
3.5.2.1. Test case.....	76
3.5.2.2. Convergence of tempering	76
3.5.2.3. Folding progress (RMSD).....	77
3.5.2.4. Folding progress (backbone dihedrals).....	79
3.5.2.5. Convergence in the dihedral space.....	80
3.5.3. Geometric measures.....	80
3.5.3.1. Representing rod of a helix.....	81
3.5.3.2. Chiral distance for packing helices.....	81
3.5.3.3. Helix distance	82
3.5.3.4. Helix angle	82
3.5.3.5. Hydrophobic contact number	82
3.5.4. Clustering method	83
3.5.4.1. The target function	83
3.5.4.2. Minimization of the target function	83
3.5.5. Initial structures.....	84

3.5.6. Representative structures at the room temperature	85
Improving statistical distribution.....	Error! Bookmark not defined.
4.1. Introduction.....	Error! Bookmark not defined.
4.2. Methods	Error! Bookmark not defined.
4.2.1. Integral identity	Error! Bookmark not defined.
4.2.2. Mean force.....	90
4.2.3. Optimal window size	92
4.2.4. Summary and practical notes	95
4.2.5. Extension to weighted histogram analysis method	96
4.3. Examples.....	98
4.3.1. Potential energy distribution.....	98
4.3.2. Volume distribution	103
4.3.3. Radial distribution function	106
4.4. Conclusions and discussions	111
4.5. Appendix.....	111
4.5.1. Alternative derivation of the fractional identity	111
4.5.2. Mean force improvement.....	114
4.5.3. Switched Lennard-Jones potential	116
4.5.4. Reference distributions	116
References	118

LIST OF FIGURES

Figure 1.1. Broken ergodicity. In classical mechanics, it is impossible to cross a potential-energy barrier higher than the total energy, for the kinetic energy would be negative. ..	7
Figure 1.2. Amino acid. R: side chain.	19
Figure 2.1. (a) $\phi(\beta)$, $\phi_s(\beta)$ and $\phi_t(\beta)$ for estimating $\tilde{E}(\beta)$. $\phi(\beta)$ is the sum of the smooth $\phi_s(\beta)$ and steep $\phi_t(\beta)$. (b) $\phi'_s(\beta)$ and $-\phi'_t(\beta)$	25
Figure 2.2. 32×32 Ising model. The method in 2.2 is labeled as Method 1, and that in 2.6.2 is labeled as Method 2. (a) Partition function, (b) heat capacity, (c) average energy, (d) $\tilde{E}(\beta)$	33
Figure 2.3. Reconstructed energy distribution at a few temperatures using Eq. (28) (solid), and results from averaging two neighboring bins (dashed). $\delta\beta = 0.0002$	34
Figure 2.4. Trpzip2. (a) Initial extended conformation; (b) a typical folded structure. The C_{α} - and the all heavy atom RMSDs are 0.25Å and 1.08Å respectively. Gray: native.	37
Figure 2.5. Trpzip2. Left: the first 200 ns of trajectory 1. Right: trajectory 3. (a) C_{α} -RMSD from the native structure, (b) C_{α} radius of gyration, (c) temperature, (d) potential energy.	38
Figure 2.6. Trpzip2. (a) RMSD distribution; (b) fraction P of the folded state. Inset: linear fitting of $\log(P_0/P - 1)$ versus β to the two-state model.....	39
Figure 2.7. Trpzip2: the heat capacity, computed from four independent trajectories. Bold solid line: empirical formula $C_V \approx 4.2 \times 10^3 / T$	41
Figure 2.8. Trp-cage. (a) Initial structure; (b) typical folded structure. The C_{α} and all heavy atom RMSDs were 0.44 Å and 1.54 Å respectively. Gray: native.....	42
Figure 2.9. Trp-cage. (a) C_{α} -RMSD; (b) C_{α} radius of gyration; (c) temperature; (d) potential energy.....	43
Figure 2.10. Villin headpiece. (a) Initial structure; (b) and (c) structures closest to the NMR (1VII) and x-ray (1YRF) structures (gray), respectively.	45

- Figure 2.11. Villin headpiece. Joint distributions of C_{α} -RMSD and C_{α} -RMSD_{core} (from residues 9~32). References: (a) NMR ; (b) x-ray. 47
- Figure 3.1. Best folded structures (blue) of four proteins. (a) α_3D , (b) α_3W , (c) Fap1-NR $_{\alpha}$, (d) S-836 compared with the respective NMR structures (red). 56
- Figure 3.2. The backbone root-mean-square deviation (RMSD) versus time. (a) α_3D , (b) α_3W , (c) Fap1-NR $_{\alpha}$, (d) S-836..... 56
- Figure 3.3. Packing-chirality D distributions for (a) α_3D and (b) a mutant α_3D_L . For α_3D , only the right-handed conformation exists, the left-handed one is hypothetical. The opposite is true for α_3D_L . Inset of panel (a): helix heptad. Crosses and dots in circles mean pointing into and out of the paper, respectively..... 59
- Figure 3.4. Packing-chirality D distributions for (a) α_3W and (b) LQLQ. The three helices are colored by blue, yellow and red, from N- to C-terminus. The shaded peaks (right scales) were obtained from regular MD started from the representative structures. 62
- Figure 3.5. The logarithm of the packing-chirality distribution $\log \rho(D_{ABC}, D_{BCD})$ of S-386. The colors of the four helices are blue, green, orange, and red, sequentially, from N- to C-terminus in representative structures. 65
- Figure 3.6. Packing patterns of the chiral images of S-836. LR, RR, RL and LL are classified by the signs of D_{ABC} and D_{BCD} . Only the first three were observed. Interactions of charged/polar residues between two helices are shown as two aligned arms with residues on the interface. Magenta bars: unfavorable interactions. Helix sliding are indicated by blue arrows. 66
- Figure 3.7. The potential of mean force and decomposed modes for (a) φ and (b) ψ . The maxima are shift to zero. 72
- Figure 3.8. Folding trajectory 7 of α_3D . (a) Instantaneous potential energy,(b) temperature versus time, (c) $H(\beta)/w(\beta)$, (d) energy histograms. 77
- Figure 3.9. For α_3D : (a) backbone RMSD versus time for a regular constant-temperature molecular dynamics (CTMD) starting from a fully-extended chain, CTMD from the native, unbiased (TP) and dihedral-biased (this method, trajectories 2, 5 and 7) tempering from the extended chain; (b) the fraction of correct backbone dihedrals versus time; (c) and (d): residue-averaged backbone dihedral distributions of φ (C-N-C $_{\alpha}$ -C) and ψ (N-C $_{\alpha}$ -C-N) respectively (reweighted to 300K); (e) and (f): the corresponding distributions at 580K.

We only included the folded state with $\text{RMSD} < 6\text{\AA}$ in (c)-(f) so that they represent only local dihedral equilibration, but not the true free energy landscape. 78

Figure 3.10. Initial extended conformations of (a) $\alpha_3\text{D}$, (b) $\alpha_3\text{W}$, (c) Fap1-NR $_{\alpha}$, (d) S-836. Water molecules are removed for clarity..... 85

Figure 3.11. Representative structures (reweighted to 300K) along (a) trajectory 7 of $\alpha_3\text{D}$ and (b) trajectory 2 of the mutant $\alpha_3\text{D}_L$ 86

Figure 4.1. The fractional identity express the ratio of a histogram sum $\int_{x_-}^{x_+} \rho(x) dx$ (shaded) to the distribution density $\rho(x^*)$ as an integral of $(\log \rho)'(x)$ 89

Figure 4.2. Potential energy distribution. (a) Histogram, fractional identity, and Adib-Jarzynski-like (AJ) identity. The same test sample were used for all methods. Symbol spacing $\Delta U = 5.0$. (b) and (c) Errors measured from the KS difference and entropic distance, respectively, as functions of window size ΔU . (d) The distributions from the original and improved weighted histogram method. (e) Canonical versus microcanonical ensembles. 99

Figure 4.3. Volume distributions. (a) $\rho(V)$ and (b) $\hat{\rho}(V)$ (adjusted) at $p = 0.115$ and $T = 1.24$. Inset of (a): the window size. Symbol spacing $\Delta V = 50.0$ 105

Figure 4.4. Radial distribution functions $g(r)$. (a) $T_1 = 0.85$; (b) $T_2 = 0.4$. Histogram, fractional identity, and original Adib-Jarzynski (AJ) identity. Symbol spacing $\Delta r = 0.1$ 109

Figure 4.5. The auxiliary function $\phi(x)$ and its derivative $\phi'(x)$ 113

Figure 4.6. Distributions from the reference samples. (a) Potential-energy distributions; (b) volume distributions; (c) and (d) radial distribution functions at $T_1 = 0.85$ and $T_2 = 0.4$ 117

LIST OF TABLES

Table 1.1. List of amino acids.....	20
Table 2.1. Lowest RMSDs in folding trajectories of trpzip2.....	37
Table 2.2. Lowest RMSDs in folding trajectories of villin headpiece.....	46
Table 3.1. The amino acid sequences of α_3D , α_3W , Fap1-NR $_{\alpha}$, S-836 and the mutants..	55
Table 3.2. Simulation conditions for α_3D , α_3W , Fap1-NR $_{\alpha}$ and S-836 and the mutants..	55
Table 3.3. Geometry measures of various conformations of three-helical bundles.....	60
Table 3.4. Parameters of the dihedral modes (A, B, and C) for φ and ψ .	73
Table 3.5. Trajectory parameters of α_3D , α_3W , Fap1-NR $_{\alpha}$ and S-836 and the mutants. .	75

Chapter 1

Background

We briefly review some key concepts in statistical mechanics [6-9], how they are used in molecular simulations [10, 11], and how to work with proteins.

1.1. Statistical mechanics

In thermodynamics, we assume that a macroscopic system can reach a unique equilibrium under any external condition specified by the temperature, pressure, etc. Therefore any change of a system can be traced back to the change of the external condition. The only remaining question is,

What does a system look like under a certain condition?

Statistical mechanics is a set of computational tools to answer the question. We review the key concepts below. We shall use an O_2 molecule in a box as a simple example (although it is not macroscopic) along the way to avoid abstraction.

1.1.1. Configuration, weight, and ensemble

We define a configuration as coordinates and velocities of all atoms in the system. For the oxygen molecule, we specify a configuration by $\mathbf{x} = \{\mathbf{r}_1, \mathbf{r}_2, \mathbf{v}_1, \mathbf{v}_2\}$, where \mathbf{r}_1 and \mathbf{r}_2 are the coordinates of the two oxygen atoms, \mathbf{v}_1 and \mathbf{v}_2 velocities. The question now is what are the *probable* configurations?

An ensemble is a collection of all *possible* configurations. If we further know the occurring frequency, or weight, of each configuration, then we can compute any static property from averaging over configurations in the ensemble. In the O₂ case, the distance between the two oxygen atoms, for example, can be computed as

$$\langle d \rangle = \sum_{\mathbf{x}} w(\mathbf{x}) d(\mathbf{x}). \quad (1)$$

where $w(\mathbf{x})$ is its weight, $d(\mathbf{x})$ the distance computed from the configuration \mathbf{x} , and $\langle d \rangle$ is its ensemble average. Obviously, all weights sum to unity,

$$\sum_{\mathbf{x}} w(\mathbf{x}) = 1. \quad (2)$$

So all we need to know is the weight $w(\mathbf{x})$. All complex phenomena, such as water boiling, protein folding/unfolding, are results of the weight change.

Note that we have assumed a discrete or quantum system in Eq. (2). For a classical system, we replace the sum by a phase-space integral over coordinates and momenta.

1.1.2. Microcanonical ensemble

It is therefore surprising that the weight $w(\mathbf{x})$, at least the one needed to explain everything we know, is very simple. If the system is isolated, then the total energy E is conserved, and statistical mechanics posits

The weight of a configuration depends only on its total energy.

In other words, configurations sharing the same total energy also share the same weight. Thus $w(\mathbf{x}) = 1/\Omega(E)$, where $\Omega(E)$ is the number of configurations with the energy being E , or the density of states. This is the microcanonical ensemble.

Once the energy function $H(\mathbf{x})$ is known, we can collect configurations with the same energy $E = H(\mathbf{x})$ and then all statistical properties are determined. Since $H(\mathbf{x})$ is determined by physical laws, our problem is formally solved.

The microcanonical ensemble is mathematically inconvenient. First, to collect configurations with the same energy E , we need a δ -function $\delta[H(\mathbf{x}) - E]$, which is infinity if $H(\mathbf{x}) = E$ but zero otherwise. Handling the singular function is often tricky. Secondly, the parameter E that characterized the ensemble is less intuitive and harder to measure than the temperature.

1.1.3. Canonical ensemble

A more commonly used ensemble is the canonical ensemble, in which

$$w_T(\mathbf{x}) = \frac{\exp[-H(\mathbf{x})/(k_B T)]}{Z(T)}, \quad (3)$$

where k_B is the universal Boltzmann constant, T is the temperature and $Z(T)$ is a factor (called the partition function) that normalizes the weight, cf. Eq. (3), i.e.,

$Z(T) = \sum_{\mathbf{x}} \exp[-H(\mathbf{x})/(k_B T)]$. For later convenience, we also define a reciprocal temperature $\beta = 1/(k_B T)$, so Eq. (3) is $w_{\beta}(\mathbf{x}) = \exp[-\beta H(\mathbf{x})]/Z(\beta)$.

Eq. (3) means that a configuration with a higher energy, or larger $H(\mathbf{x})$, is less likely to occur in the ensemble, hence smaller $w(\mathbf{x})$. This is especially so at a low temperature T . In the O_2 case, the potential energy is low when the two oxygen atoms are bonded. But if the temperature is very high, the energetic benefit from the weight diminishes, so the bond breaks.

Since the total energy is the sum of the potential energy $U(\mathbf{r})$ and kinetic energy $K(\mathbf{v})$, we can factorize the weight as

$$w(\mathbf{x}) \propto \exp[-\beta U(\mathbf{r})] \exp[-\beta K(\mathbf{v})]. \quad (4)$$

This means that the distributions for \mathbf{r} and \mathbf{v} are independent. So we can ignore the velocities and focus on the coordinates alone.

1.1.4. Discussions

A key difference between the two ensembles is that the canonical ensemble is parameterized by the temperature T , while the microcanonical one by the total energy E . Since we know the temperature better, the former is more convenient.

Note that the temperature T or β is just a leverage to *control* the total energy. Similarly, if we wish to control some other quantity $X(\mathbf{x})$, which is a function of configuration \mathbf{x} , we change the weight to $w(\mathbf{x}) \propto \exp[-\beta H(\mathbf{x}) - \beta_X X(\mathbf{x})]$.

An interesting inverse problem is to measure the controlling parameters in cases where they are not specified explicitly by the ensemble, e.g., the temperature in the microcanonical ensemble [12, 13], see 4.2.2.

1.1.5. Two-dimensional Ising model

The two-dimensional (2D) Ising model is one of the simplest but nontrivial models in statistical mechanics. It is composed of $L \times L$ sites on a 2D rectangular lattice. Each site has a spin, which is either up or down. The potential energy is the sum of horizontal and vertical interactions of adjacent spins. Two aligned (same) or anti-aligned (different) spins contribute $-J$ or J respectively to energy.

Different from molecular configurations, spin configurations are discrete and countable: there are exactly $2^{L \times L}$ of them. Despite its simplicity, the 2D Ising model has a second-order phase-transition, in which the heat capacity $C = d\langle U \rangle_T / dT$ (where $\langle U \rangle_T$ is average potential energy at T) undergoes a sudden change at $T_c = 2J / \log(1 + \sqrt{2}) \approx 2.269J$. This is remarkable since the singularity is created by a simple and rather innocent-looking energy function.

In the canonical ensemble, the model can be solved exactly [14]; so we know the partition function, average energy, etc., at any temperature. For this reason, it is often used to validate a simulation method.

1.2. Molecular dynamics

Molecular dynamics (MD) is a way of populating an ensemble by following Newton's second law (also known as the equation of motion),

$$\mathbf{F} = m\mathbf{a}, \quad (5)$$

where \mathbf{F} , m , and \mathbf{a} are the force, mass and acceleration, respectively. The force is just the negative derivative of potential energy $\mathbf{F} = -\nabla U(\mathbf{r})$, and the acceleration the rate of change of the velocity $\mathbf{a} = d\mathbf{v}/dt$. Newton's equation keeps the total energy constant, for $K(\mathbf{v}) = \frac{1}{2}m\mathbf{v}^2$ and

$$d[U(\mathbf{r}) + K(\mathbf{v})]/dt = \nabla U \cdot d\mathbf{r}/dt + m\mathbf{v} \cdot d\mathbf{v}/dt = \mathbf{v} \cdot (-\mathbf{F} + m\mathbf{a}) = 0.$$

It is thus tempting to assume that

Following Newton's equation, the trajectory covers all configurations of the same energy with equal frequency, and thus fulfills a microcanonical ensemble.

But we have to apply some restrictions to make the statement true. For example, the Newton's equation also conserves the total linear and angular momenta. The assumption is also false, if there was a barrier that divides the configuration space, a problem called broken ergodicity, see Fig. 1.1.

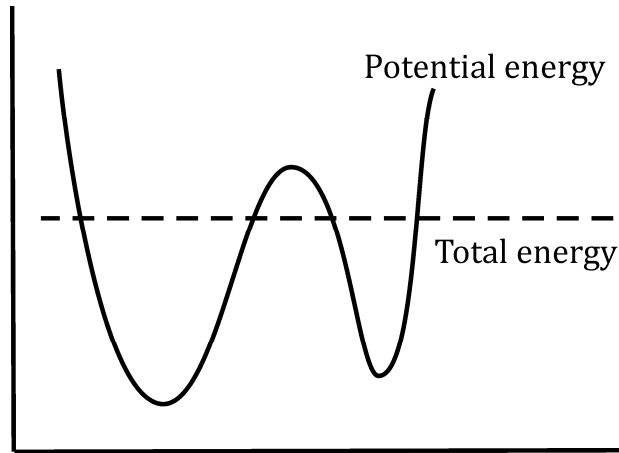


Figure 1.1. Broken ergodicity. In classical mechanics, it is impossible to cross a potential-energy barrier higher than the total energy, for the kinetic energy would be negative.

Despite the limitations, the statement is commonly assumed, because if the system is regularly disturbed, the trajectory will be properly randomized.

Note that MD also contains time information, e.g., how fast a protein folds, but this information is unused in the ensemble theory.

1.2.1. Integrator

There are several ways [10] to integrate Eq. (5) numerically. A good integrator ensures the energy not to blow up after a large number of steps because of the accumulated numeric errors. It will also ensure the conservation of the volume element of the phase space, i.e., the space spanned by all coordinates \mathbf{r}_i and momenta $m_i \mathbf{v}_i$. We show two commonly-used examples below.

1.2.1.1. Leapfrog

The leapfrog integrator reads

$$\begin{aligned}\mathbf{v}^{(n+1)} &= \mathbf{v}^{(n)} + (\mathbf{F}^{(n)} / m) \Delta t, \\ \mathbf{r}^{(n+1)} &= \mathbf{r}^{(n)} + \mathbf{v}^{(n+1)} \Delta t,\end{aligned}$$

where the number of iterations is shown on the superscripts, and $\mathbf{F}^{(n)}$ is the force evaluated at $\mathbf{r}^{(n)}$. Note that when we are changing \mathbf{v} , \mathbf{r} is fixed; but when we are changing \mathbf{r} , \mathbf{v} is fixed. In this way, the phase-space volume element $d\mathbf{r}d\mathbf{v}$ (assuming a uniform mass) is conserved even though the integrator is approximate (sliding a rectangle to a parallelogram along an edge keeps the area a constant). Although it is simple, the time frames of $\mathbf{x}^{(n)}$ and $\mathbf{v}^{(n)}$ differ by $\Delta t/2$. This is fixed in following velocity-Verlet integrator.

1.2.1.2. Velocity-Verlet

The velocity-Verlet integrator reads

$$\begin{aligned}\mathbf{v}^{(n+1/2)} &= \mathbf{v}^{(n)} + (\mathbf{F}^{(n)} / m) \Delta t, \\ \mathbf{r}^{(n+1)} &= \mathbf{r}^{(n)} + \mathbf{v}^{(n+1/2)} \Delta t, \\ \mathbf{v}^{(n+1)} &= \mathbf{v}^{(n+1/2)} + (\mathbf{F}^{(n+1)} / m) \Delta t,\end{aligned}$$

where $\mathbf{v}^{(n+1/2)}$ is the intermediate velocity. So it splits the first step of the leapfrog integrator into two halves (the first and last here), such that $\mathbf{x}^{(n)}$ and $\mathbf{v}^{(n)}$ represent the two quantities at the same time frame: $\mathbf{v}^{(n+1/2)}$ here is $\mathbf{v}^{(n+1)}$ in the leapfrog case.

1.2.2. Molecular force field

A molecular force field means a potential energy function $U(\mathbf{r})$. Although $U(\mathbf{r})$ should be determined from first principle, we always use an approximate one in practice. The classical mechanics version of the statistical mechanics is accurate

only up to atomic level, and fails if the motion of electrons plays a critical role. Fortunately, electrons often move so fast that their contribution can be somehow absorbed in an effective $U(\mathbf{r})$, which only describes the motion of nuclei. We shall assume this case. Such a force field usually has the following terms

$$U(\mathbf{r}) = U_{\text{bond}} + U_{\text{angle}} + U_{\text{dihedral}} + U_{\text{vdw}} + U_{\text{charge}}.$$

We explain the terms below.

Bond: for the length of two atoms involved in a chemical bond. The potential is

$u(r) = (k/2)(r - r_0)^2$, where r is the distance between the two atoms, r_0 the reference value, k spring constant.

Angle: for the angle of three atoms in an sp^2 or sp^3 bond. The potential is

$u(\theta) = (k_\theta/2)(\theta - \theta_0)^2$, where θ is the angle, θ_0 the reference value, e.g., 120° for H-C-C atoms in ethylene, and k_θ some constant.

Dihedral: for the dihedral ϕ of four steric atoms. The potential can be harmonic

$u(\phi) = (k_\phi/2)(\phi - \phi_0)^2$, where ϕ_0 is a single reference value, k_ϕ some constant

(improper dihedral), or a Fourier series $u(\phi) = \sum_{k=0} a_k \cos(k\phi)$, where a_k are

constants (proper dihedral). More sophisticated forms are also used.

Van der Waals: ubiquitous long range interaction. The simple Lennard-Jones

potential $u(r) = 4\varepsilon[(\sigma/r)^{12} - (\sigma/r)^6]$ is often used, where ε and σ are the units for

energy and length, respectively. The r^{-6} term models the long-range attraction due to the induced dipole-dipole interaction, i.e., the weak attraction produced by the

mutually-polarized electrons in the two atoms. Since the electric field \mathbf{E} from a dipole (polarized electrons + nucleus) is proportional to r^{-3} , and the perturbation is of second-order, the energetic addition is proportional to $\mathbf{E}^2 \propto r^{-6}$. The r^{-12} terms models the short-range repulsion, and is mainly for practical convenience, as r^{-12} is the square of r^{-6} . The minimal of the potential is reached at $r = \sqrt[6]{2}\sigma$, where $u(r) = -\epsilon$.

Charge: Coulomb interactions of charged atoms or $u(r) = Kq_1q_2/r$, where q_1 and q_2 are the charges of the two atoms, r is their distance, and $K = 1/(4\pi\epsilon_0)$ the Coulomb constant. Since chemical bonds tend to distort the electron distribution, the *effective* charge on an atom can be a fraction of the elementary charge.

Further, for implicit solvent simulations, we have terms to compensate the missing solvent, i.e., surrounding water molecules.

Parameters of a force field are usually semi-empirical. Its construction often involves comparison with experimental data and quantum mechanical calculations.

1.2.3. Periodic boundary condition

Although we usually simulate a finite system, we try to mimic an infinitely large one by assuming the periodic boundary condition.

Here is what we do. We assume the system is in a (e.g. cubic) box. We now reproduce the box in three dimensions, and stack them to an infinite lattice. In this way, even an atom at the corner is surrounded by atoms from other periodic images of the box, and thus has the same environment as an atom in the middle of the box.

1.2.4. Potential cutoff

The van der Waals interaction, see 1.2.2, decays quickly with the pair distance r . It is therefore common to cut off the potential at some short distance r_c , i.e., $u(r) = u'(r) = 0$ for $r > r_c$, to accelerate the computation of potential energy $u(r)$ and force. The potential for $r \leq r_c$ is also shifted such that it is continuous at r_c , i.e., $u(r_c^-) = 0$ to avoid an infinite force, although the force will still be discontinuous at r_c . In practice, the discontinuous force might not make MD unstable if r_c is large, but a more careful way is to turn the potential gradually to zero, see e.g. 4.5.3.

When used with the periodic boundary condition, the cutoff distance r_c is usually shorter than the half of the shortest box length. In this way, no pair of atoms is counted more than once.

1.2.5. Ewald sum

The charge interaction decays very slowly ($\sim 1/r$ with r being the distance between two charged particles). Thus a simple cutoff of the potential is erroneous and dangerous. An elegant solution is the Ewald sum [10]. The idea is that since the system is periodic (see 1.2.3), so are the charge distribution $\rho(\mathbf{r})$ and electric potential $\phi(\mathbf{r})$, which can be expanded by a Fourier series. Recall the electric energy can be computed from

$$U_{\text{charge}} = \frac{1}{2} \int \rho(\mathbf{r})\phi(\mathbf{r})d\mathbf{r} = \frac{1}{2} \sum_i q_i \phi(\mathbf{r}_i). \quad (6)$$

But a long-range $\phi(\mathbf{r})$ corresponds to a $\tilde{\phi}(\mathbf{k}) = \int \phi(\mathbf{r}) \exp(-i\mathbf{k} \cdot \mathbf{r}) d\mathbf{r}$ (i.e., Fourier transform) that decays quickly with $|\mathbf{k}|$. So it is easy to compute $\tilde{\phi}(\mathbf{k})$ first. We also recall $\phi(\mathbf{r})$ can be computed from either a Coulomb sum $\phi(\mathbf{r}_i) = \sum_j q_j / (4\pi\epsilon_0 r_{ij})$ or solving the Poisson equation $\nabla^2 \phi(\mathbf{r}) = -\rho(\mathbf{r})/\epsilon_0$, and both strategies will be used below.

The original $\rho(\mathbf{r})$ is a set of discrete point charges, or $\rho(\mathbf{r}) = \sum_i q_i \delta(\mathbf{r} - \mathbf{r}_i)$. We first replace each point distribution $\delta(\mathbf{r} - \mathbf{r}_i)$ by a smoothly-varying cloud distribution $g(\mathbf{r} - \mathbf{r}_i) \propto \exp[-\alpha^2(\mathbf{r} - \mathbf{r}_i)^2]$, and define the result as $\rho_l(\mathbf{r})$, and the difference as $\rho_s(\mathbf{r}) = \rho(\mathbf{r}) - \rho_l(\mathbf{r})$. The electric potential $\phi_l(\mathbf{r})$ for $\rho_l(\mathbf{r})$ can be readily solved in the reciprocal \mathbf{k} space, where the Poisson equation is simply $\tilde{\phi}_l(\mathbf{k}) = \tilde{\rho}_l(\mathbf{k})/(\epsilon_0 k^2)$. An inverse transform of $\tilde{\phi}_l(\mathbf{k})$ then gives $\phi_l(\mathbf{r})$.

On the other hand, each point charge in $\rho_s(\mathbf{r})$ is wrapped around by a cloud of opposite charge, so its corresponding electric potential $\phi_s(\mathbf{r})$ decays quickly. We

can thus compute it as a modified Coulomb sum as $\phi_s(\mathbf{r}_i) = \frac{1}{4\pi\epsilon_0} \sum_j \frac{\text{erfc}(\alpha r_{ij})}{r_{ij}} q_j$.

For each point charge, the contribution from its own cloud charge is not included in

the Coulomb sum. The correction $\phi_c(\mathbf{r}_i) = -\frac{q_i}{4\pi\epsilon_0} \frac{2\alpha}{\sqrt{\pi}}$ should be applied.

Finally, the electric potential $\phi(\mathbf{r}) = \phi_l(\mathbf{r}) + \phi_s(\mathbf{r}) + \phi_c(\mathbf{r})$, and we obtain the potential energy from Eq. (6); the force is similarly computed.

Practically, we must ensure the entire system is charge neutral to use the Ewald sum. Ions are often added to neutralize a charged system, e.g. a protein.

1.2.6. Thermostat

Newton's equation works natively for a microcanonical ensemble. We can, however, use an artificial thermostat to design an MD for the canonical ensemble [10]. The idea is to regularly adjust the velocities of atoms to satisfy the distribution $\exp[-\beta K(\mathbf{v})]$; the potential energy will then be forced to adopt $\exp[-\beta U(\mathbf{r})]$.

A simple and efficient thermostat is the velocity rescaling thermostat [15], in which we regular rescale the velocity according to a Langevin equation as

$$\frac{dK}{dt} = \frac{1}{2} N k_B T - K + \sqrt{2K k_B T} \xi, \quad (7)$$

where K is the kinetic energy, N is the number of degrees of freedom, ξ is the Gaussian white noise satisfying $\langle \xi(t) \cdot \xi(t') \rangle = \delta(t - t')$.

In implementation, we obtain a new K' by integrating Eq. (7) with a time step Δt as $K' = K + (\frac{1}{2} N k_B T - K) \Delta t + \sqrt{2K k_B T \Delta t} \xi_G$ (where ξ_G is Gaussian random number of zero mean and unit variance), then scale the velocity by $\sqrt{K'/K}$.

1.3. Monte-Carlo simulation

A Monte-Carlo (MC) simulation is another way of populating configurations. The basic idea is to build a Markov chain, following which the system will eventually travel through most probable configurations no matter where it starts from.

Note that the dynamics in a MC simulation, however, is usually artificial and is of no physical consequence. The strength of MC lies in its flexibility that allows us to devise configuration changes in any fashion as long as the distribution is correctly populated. Enhanced sampling methods, and some thermostat methods are in fact MC algorithms, although many of them are designed for MD.

In MC, the velocity components are usually not needed, so a configuration simply means coordinates, and the energy means the potential energy.

An MC algorithm is often designed to satisfy two conditions: ergodicity and detailed balance (or more generally balance). But let us first see an example.

1.3.1. Metropolis algorithm

A typical MC simulation proceeds as follows. In each step, we change the current configuration \mathbf{x} to a different one \mathbf{x}' . For example, in a molecular system, we can randomly pick an atom, then displace it by a random amount (mean-zero). In the Ising model, we can flip the spin at a random site. The modification should be unbiased such that the probability of generating \mathbf{x}' from \mathbf{x} is equal to that from \mathbf{x}' to \mathbf{x} . We then decide whether to accept \mathbf{x}' by the probability

$$A(\mathbf{x} \rightarrow \mathbf{x}') = \min\{1, w(\mathbf{x}')/w(\mathbf{x})\}, \quad (8)$$

where $w(\mathbf{x})$ the ensemble weight or the distribution density. Particularly, for the canonical ensemble, we have $w(\mathbf{x}) \propto \exp[-\beta U(\mathbf{x})]$, so

$$A(\mathbf{x} \rightarrow \mathbf{x}') = \min\{1, \exp[-\beta \Delta U]\}, \quad (8')$$

where $\Delta U = U(\mathbf{x}') - U(\mathbf{x})$. This is the Metropolis algorithm [16].

1.3.2. Ergodicity

Ergodicity means there is a nonzero probability (or probability density) to go from an arbitrary configuration \mathbf{x} to another one \mathbf{x}' by a finite number of steps. In practice, this condition is often easily satisfied.

For example, in a molecular system, we can connect any two configurations by displacing particles of different coordinates in finite number of steps.. In the Ising model, there is a probability that all different spins in the two configurations are flipped after a finite number of steps.

1.3.3. Detailed balance

It is readily shown that Eq. (8) satisfies detailed balance:

$$w(\mathbf{x})A(\mathbf{x} \rightarrow \mathbf{x}') = w(\mathbf{x}')A(\mathbf{x}' \rightarrow \mathbf{x}). \quad (9)$$

For a set of the configurations satisfying $w(\mathbf{x})$, then the new distribution after a MC step would be $\sum_{\mathbf{x}} w(\mathbf{x})A(\mathbf{x} \rightarrow \mathbf{x}') = w(\mathbf{x}') \sum_{\mathbf{x}} A(\mathbf{x}' \rightarrow \mathbf{x}) = w(\mathbf{x}')$, i.e., a MC step keeps the distribution unchanged, if it is already $w(\mathbf{x})$. Further, if we start with a distribution that deviates from $w(\mathbf{x})$, the deviation diminishes after a MC step.

Detailed balance often serves as the golden rule for designing MC algorithms. But an MC algorithm does not have to look like the Metropolis one: there are cluster algorithms [17, 18] that are much more sophisticated and efficient.

1.3.4. Balance

Detailed balance can be relaxed to a more general balance condition [19]:

$$\sum_{\mathbf{x}} w(\mathbf{x}) A(\mathbf{x} \rightarrow \mathbf{x}') = w(\mathbf{x}'),$$

i.e., the desired distribution is preserved. Balance plus ergodicity are also sufficient to guarantee a correct MC algorithm.

Practically, it often means that as long as there is some random component in all moves, we can change some moves from random ones to sequential ones. For example, in the molecular system, instead of randomly choosing a particle to move, we can also sequentially move particles [19].

1.4. Tempering

Tempering is a Monte Carlo technique to accelerate sampling by exploiting a fast dynamics at a high temperature. Tempering is often formulated in the canonical ensemble, and we assume so below.

1.4.1. Parallel tempering

In a parallel tempering, or replica exchange [20-23], we run several copies of the system in parallel, with each assuming a different temperature. In simulation,

we randomly attempt to swap the temperatures of two copies according to the following acceptance probability

$$A(\beta, \beta') = \min \{1, \exp[-(\beta - \beta')(U - U')]\},$$

where U and β are the potential energy and the reciprocal temperature (before the swap) of one copy, and U' and β' those of the other.

1.4.2. Simulated tempering

In simulated tempering [24, 25], the system changes the temperature according to the potential energy fluctuation: if the current potential energy is above a certain value, the temperature tends to increase; otherwise, it tends to decrease. A temperature transition $\beta \rightarrow \beta'$ is accepted according to the probability

$$A(\beta \rightarrow \beta') = \min \{1, \exp[(\beta - \beta')U] Z(\beta) / Z(\beta')\},$$

where U is the potential energy, β and β' are the old and new temperatures, and $Z(T) = \sum_{\mathbf{x}} \exp[-\beta U(\mathbf{x})]$ is the partition function. It can be shown that in an equivalent setting, a single-copy tempering is always more efficient than the parallel tempering counterpart [26, 27].

The difficulty, however, is to estimate the value of the partition function at every temperature. This is nontrivial for the partition function can easily change by several orders of magnitude. Fortunately, there is an iterative scheme [28] that can automate the process, as illustrated in reference [29].

1.4.3. Realizing temperature change

In MC, the temperature is part of the acceptance probability, see Eq. (8'), so the change is trivial. In MD, the temperature is controlled by the thermostat (see 1.2.6). Frequently changing the temperature of a thermostat might destabilize it. Thus a common practice is to simultaneously scale the velocities $\sqrt{\beta/\beta'}$ and change the temperature of the thermostat from β to β' .

An alternative approach is to scale the force. If the current temperature is β and the thermostat temperature β_0 , then the effective force should be $(\beta/\beta_0)\mathbf{F}$. The practice is based on the following ensemble weight

$$w(\mathbf{r}, \mathbf{v}) \propto \exp\left[-\beta_0 \frac{\beta}{\beta_0} U(\mathbf{r})\right] \exp[-\beta_0 K(\mathbf{v})].$$

Thus the velocities, and hence the thermostat, see no change of the temperature, but the equation of motion will experience a change in the potential, and hence force.

1.5. Protein

A protein (polypeptide) is a linear chain of amino acids linked by peptide bonds. A natural protein can often automatically find a unique three dimensional structure from an open chain [30-35]. A challenge is to understand this by physical laws and to mimic the process on a computer by simulation [36-49].

1.5.1. Amino acid

The basic structure of an amino acid is $^+H_3N-CHR-COO^-$, see Fig. 1.2, where R denotes the side chain group. The middle carbon is called the alpha carbon (C_α), and those on R are C_β , C_γ , ..., according to the number of chemical bonds away from C_α . There are 20 common amino acids with different R groups, as shown in Table 1.1.

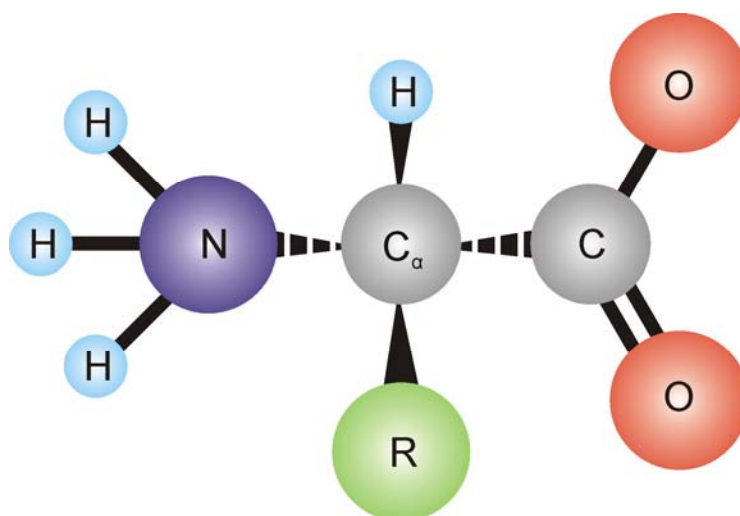


Figure 1.2. Amino acid. R: side chain.

1.5.2. Charge

The total charge of a protein is the sum of all amino acids. Typical values at $pH \approx 7$ are listed in Table 1.1. Generally it can be computed from **pKa**, which measures the ability of gaining a variable proton (H^+). A residue is likely to have the proton (**protonated**) if the pKa is greater than the pH, or to lose it otherwise.

In preparing an explicit-solvent simulation, the total charge of the protein should be computed in advance, so that the solution can be neutralized by adding ions of the equal but opposite charges in order to use Ewald sum, see 1.2.4.

1.5.3. Chirality

In preparing the initial configuration of a protein, one should pay attention to its chemical chirality, for it does not change during simulation. The C_{α} atom is a chirality center and is always left-handed (L-). Further the C_{β} atoms of isoleucine and threonine are also chiral, usually left- (L-) and right-handed (D-), respectively.

Table 1.1. List of amino acids.

Amino acid	3-letter	1-letter	Charge [†]	pKa [‡]	Polar	Hydrophathy [§]
Glycine	Gly	G	0			-0.4
Alanine	Ala	A	0			1.8
Valine	Val	V	0			4.2
Leucine	Leu	L	0			3.8
Isoleucine	Ile	I	0			4.5
Proline	Pro	P	0			-1.6
Serine	Ser	S	0		P	-0.8
Threonine	Thr	T	0		P	-0.7
Methionine	Met	M	0			1.9
Cysteine	Cys	C	0	8.2 (-SH)	P	2.5
Phenylalanine	Phe	F	0			2.8
Tyrosine	Tyr	Y	0	10.1 (-OH)	P	-1.3
Tryptophan	Trp	W	0			-0.9
Histidine	His	H	0 (+1)	6.1 (-N _δ H ⁺)	P	-3.2
Lysine	Lys	K	+1	10.5 (-NH ₃ ⁺)	P	-3.9
Arginine	Arg	R	+1	12.8 (-NH ₂ ⁺)	P	-4.5
Aspartic acid	Asp	D	-1	3.9 (-OH)	P	-3.5
Glutamic acid	Glu	E	-1	4.1 (-OH)	P	-3.5
Asparagine	Asn	N	0		P	-3.5
Glutamine	Gln	G	0		P	-3.5

[†] For pH = 7.

[‡] Values for side chains; larger pKa means easier to gain the highlighted proton (H⁺).

[§] Values from [50], being larger means less likely to interact with water.

Chapter 2

A continuous tempering

2.1. Introduction

The objective of this chapter is to present a tempering method in which the temperature is a continuous variable, as well as its application in folding proteins in explicit solvent. The contents are largely identical to those in reference [42].

Molecular dynamics (MD) simulations at room temperature can be slow for large complex systems, such as proteins in explicit solvent. A promising solution is tempering, which exploits a fast dynamics at higher temperatures by a generalized ensemble with a variable temperature. Tempering can be based on a single copy (simulated tempering) [24, 25, 29, 51, 52], or multiple copies (parallel tempering) [20-23].

In traditional tempering methods, the temperature is a discrete with a few predefined values. In the canonical ensemble, as system size grows, the success rate of a transition between two neighboring temperatures depends on the overlap of energy distributions of the two temperatures and decays as the system size grows [27]. Thus, to maintain sampling efficiency, we need more temperatures to narrow down the spacing. In parallel tempering, more temperatures mean more copies and hence more computational resources. In simulated tempering, the number of parameters, the values of the partition function [29], to be estimated also increases with the number of temperatures. Therefore, it is desirable to have a method that abandons the discrete setting.

We present a continuous tempering method that is intended to overcome the above drawbacks. In 2.2, we describe the method. In 2.3, we verify it on a 2D Ising model. In 2.4 we apply it to fold three mini proteins, trpzip2 (12 residues), trp-cage (20 residues), and villin headpiece (36 residues), in explicit solvent. In a more recent study, Liu *et al.* folded a λ -repressor (80 residues) by the method [48].

2.2. Method

We describe how to use the method in 2.2.1. The rest of the section gives details on its derivation and improvements.

2.2.1. The procedure

The method works this way. We wish to simulate a system for a temperature range $(\beta_{\min}, \beta_{\max})$ according to a predefined distribution $w(\beta)$, which is roughly proportional to $1/\beta$ for a molecular system, see 2.6.3.

In each simulation step, we first change the system configuration according to either a constant temperature molecular dynamics (MD) or some Monte Carlo (MC) method. Next, we update the temperature according to

$$\frac{d(1/\beta)}{dt} = \frac{d(k_B T)}{dt} = E - \tilde{E}(\beta) - \frac{\partial \log w(\beta)}{\partial \beta} + \frac{\sqrt{2}}{\beta} \xi, \quad (10)$$

where E is the current potential energy, $\tilde{E}(\beta)$ the estimated potential energy at β (discussed later), and ξ a Gaussian white noise satisfying $\langle \xi(t) \cdot \xi(t') \rangle = \delta(t - t')$.

Note that t here needs not to be the same as the real time in MD. In implementation, we first compute $1/\beta$, update it according to Eq. (10), then invert it back to β . The effect of the temperature change can be realized as a scaling of velocity or force in MD (see 1.4.3). We repeat the process until the simulation ends.

The remaining task is to compute $\tilde{E}(\beta)$. We will compute the average energies from two windows (β_-, β) and (β, β_+) surrounding β , and then linearly combine them to form an unbiased estimate.

First, we divide the entire range to many bins (β_i, β_{i+1}) . The bin size should be much smaller than the temperature spacing in the traditional tempering. Each

bin i collects independent statistical moments of the potential energy whenever the current β falls in (β_i, β_{i+1}) . We then compute two parameters a_+ and a_- by solving

$$a_+ + a_- = 1, \quad (11)$$

$$\left\langle \phi(\beta') \left\langle \Delta E^2 \right\rangle_{\beta'} \right\rangle_{(\beta_-, \beta_+)} = 0. \quad (12)$$

where $\phi(\beta) = \phi_s(\beta) + \phi_t(\beta)$ and

$$\phi_s(\beta) = \begin{cases} a_- (\beta - \beta_-) / (\beta_{j+1} - \beta_-), & \beta \in (\beta_-, \beta_{i+1}) \\ a_+ (\beta - \beta_+) / (\beta_+ - \beta_{j+1}), & \beta \in (\beta_{i+1}, \beta_+) \end{cases} \quad (13)$$

$$\phi_t(\beta) = \begin{cases} -(\beta - \beta_i) / (\beta_{i+1} - \beta_i), & \beta \in (\beta_i, \beta_{i+1}) \\ 0, & \text{otherwise} \end{cases} \quad (14)$$

respectively, see Fig. 2.1(a). Note that $\langle \dots \rangle_{\beta'}$ is the configuration average at a fixed β' . Since the bin is small, we replace it by the corresponding value computed from the bin containing β' , while $\langle \dots \rangle_{(\beta_-, \beta_+)}$ is the average over the window (β_-, β_+) or bins within it. After the averaging, Eq. (12) is a linear equation of a_+ and a_- . By solving Eqs. (11) and (12), we determine a_+ and a_- . Neither a_+ or a_- should be negative, and zero is used in case a negative value occurs. Basically, a_+ or a_- are the relative weights for combining the average energies from (β_-, β) and (β, β_+) , respectively. $\tilde{E}(\beta)$ is then calculated as

$$\tilde{E}(\beta) = \sum_j \phi'_s(\beta_j) \delta \beta_j \langle E \rangle_j, \quad (15)$$

where $\delta\beta_j = \beta_{j+1} - \beta_j$, $\langle E \rangle_j$ is the average energy from the bin (β_j, β_{j+1}) . $\phi'_s(\beta_j)$ is shown in Fig. 2.1(b).

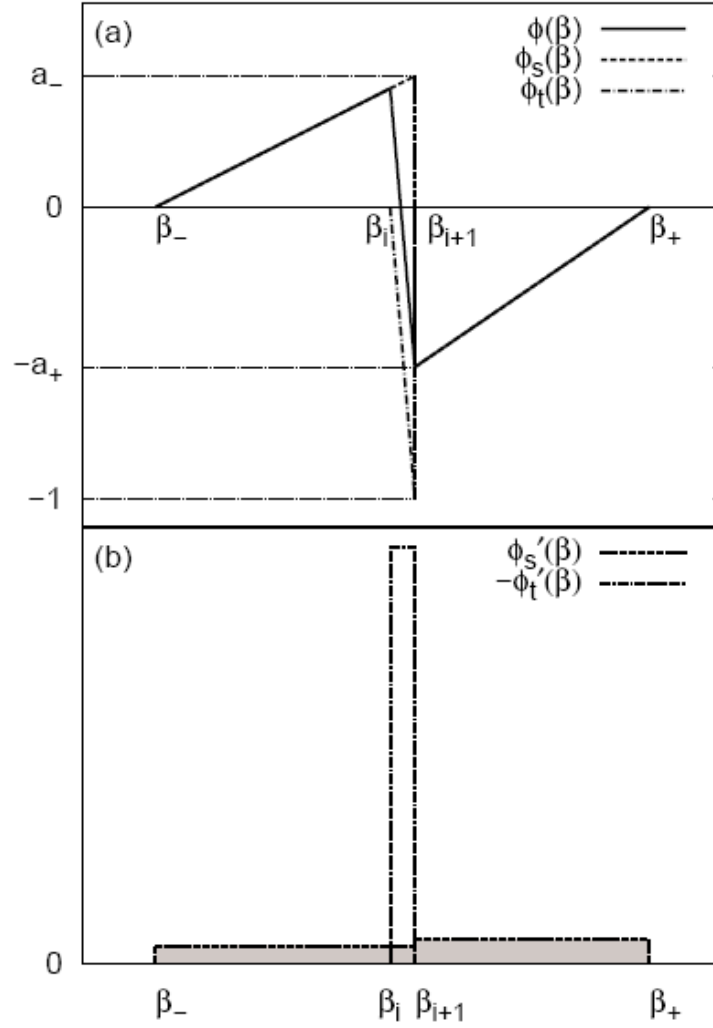


Figure 2.1. (a) $\phi(\beta)$, $\phi_s(\beta)$ and $\phi_t(\beta)$ for estimating $\tilde{E}(\beta)$. $\phi(\beta)$ is the sum of the smooth $\phi_s(\beta)$ and steep $\phi_t(\beta)$. (b) $\phi'_s(\beta)$ and $-\phi'_t(\beta)$.

2.2.2. A continuous temperature ensemble

We now explain the algorithm. The underlying apparatus is a generalized ensemble, in which the temperature β is a *continuous* variable in a given range

$(\beta_{\min}, \beta_{\max})$. The configuration distribution at a fixed β is identical to the canonical one. The aim is to correctly sample the distribution.

First, once the overall temperature distribution $p(\beta)$ is given, the joint distribution $p(\beta, \mathbf{x})$ of configuration \mathbf{x} and β is determined:

$$p(\beta, \mathbf{x}) = \frac{\exp[-\beta E(\mathbf{x})]}{Z(\beta)} p(\beta), \quad (16)$$

where $E(\mathbf{x})$ is the potential energy, and $Z(\beta) = \int \exp[-\beta E(\mathbf{x})] d\mathbf{x}$ is the canonical partition function. At a fixed β , Eq. (16) can be sampled by a constant temperature MD/MC. Similar, at a fixed configuration \mathbf{x} , Eq. (16) gives the distribution of β , which is sampled by Eq. (10), see more below.

If $Z(\beta)$ is known, we replace $p(\beta)$ by the desired weight $w(\beta)$, and the job is done. But since $Z(\beta)$ is usually unknown, we construct it on the fly. We use an approximate $\tilde{Z}(\beta)$ in Eq. (16):

$$p(\beta, X) = \frac{\exp[-\beta E(\mathbf{x})]}{\tilde{Z}(\beta)} w(\beta), \quad (17)$$

to conduct sampling. The new $p(\beta)$ is

$$p(\beta) = \int p(\beta, \mathbf{x}) d\mathbf{x} = \frac{Z(\beta)}{\tilde{Z}(\beta)} w(\beta). \quad (18)$$

In simulation, as we adaptively adjust $\tilde{Z}(\beta)$, $p(\beta)$ changes too. Upon convergence, $\tilde{Z}(\beta) \rightarrow Z(\beta)$, so $p(\beta) \rightarrow w(\beta)$.

Given a configuration \mathbf{x} , the sampling along β can be performed by Eq. (10).

Note that $\tilde{Z}(\beta)$ enters Eq. (10) through $\tilde{E}(\beta) \equiv -\partial \log \tilde{Z}(\beta) / \partial \beta$, see 2.6.1 for a proof.

The remaining task is to converge $\tilde{Z}(\beta)$, or $\tilde{E}(\beta)$.

2.2.3. Unbiased estimate of a partition function

We want to obtain an $\tilde{Z}(\beta)$ that converges to $Z(\beta)$. In implementation, we divide the range $(\beta_{\min}, \beta_{\max})$ to small bins (β_i, β_{i+1}) , and demand that at any bin boundary β_i , $\tilde{Z}(\beta_i) \rightarrow Z(\beta_i)$:

$$\tilde{Z}(\beta_i) / \tilde{Z}(\beta_{i+1}) = Z(\beta_i) / Z(\beta_{i+1}). \quad (19)$$

This ratio form avoids the arbitrary constant. With a small bin size, the difference between $\tilde{Z}(\beta)$ and $Z(\beta)$ is negligible for practical purposes.

We arrange Eq. (19) as [53],

$$\begin{aligned} \frac{Z(\beta)}{\tilde{Z}(\beta)} \Big|_{\beta_i}^{\beta_{i+1}} &= \int_{\beta_i}^{\beta_{i+1}} d\beta \left[\frac{d \log Z(\beta)}{d\beta} - \frac{d \log \tilde{Z}(\beta)}{d\beta} \right] \frac{Z(\beta)}{\tilde{Z}(\beta)} \\ &= \int_{\beta_i}^{\beta_{i+1}} d\beta \left[\tilde{E}(\beta) - \langle E \rangle_{\beta} \right] \frac{p(\beta)}{w(\beta)} = \left\langle \frac{\tilde{E}(\beta) - \langle E \rangle_{\beta}}{w(\beta)} \right\rangle_i, \end{aligned}$$

where $\langle E \rangle_{\beta}$ denotes the canonical average energy at β ; and we have used Eq. (18),

and rewritten the integral to a bin average: $\langle A \rangle_i \equiv \int_{\beta_i}^{\beta_{i+1}} d\beta p(\beta) A$.

During simulation, if we adaptively force the right hand side to zero:

$$\left\langle \frac{\tilde{E}(\beta)}{w(\beta)} \right\rangle_i = \left\langle \frac{\langle E \rangle_\beta}{w(\beta)} \right\rangle_i, \quad (20)$$

the left hand side vanishes too, so $\tilde{Z}(\beta_{i+1})/Z(\beta_{i+1}) = \tilde{Z}(\beta_i)/Z(\beta_i)$, and Eq. (19) is satisfied [53].

We proceed by assuming a sufficiently small bin size and (i) $\tilde{E}(\beta)$ being a constant \tilde{E}_i within a bin i , and correspondingly, $\log \tilde{Z}(\beta)$ varies linearly with β , and (ii) $p(\beta)/w(\beta)$ can be treated as a constant. Eq. (20) is then simplified as

$$\tilde{E}_i = \frac{\int_{\beta_i}^{\beta_{i+1}} d\beta \langle E \rangle_\beta p(\beta)/w(\beta)}{\int_{\beta_i}^{\beta_{i+1}} d\beta p(\beta)/w(\beta)} \approx \left\langle \langle E \rangle_\beta \right\rangle_i, \quad (21)$$

and the ratio of the partition function is estimated as

$$\ln[Z(\beta_i)/Z(\beta_{i+1})] = \tilde{E}_i \Delta\beta_i,$$

where $\Delta\beta_i = \beta_{i+1} - \beta_i$.

Eq. (21) means that one can estimate \tilde{E}_i from the data saved in bin i . The approach is correct, but slightly inefficient because the amount of data within a bin shrinks with the width. On the other hand, a large bin leads to a significant distribution error within a bin, for $\tilde{E}(\beta)$ is a constant. We solve the problem by an integral identity.

2.2.4. Estimators based on integral identities

We now present a method for drawing an unbiased estimate \tilde{E}_i from a large temperature window instead of a single bin. A similar technique for improving distributions is presented in **Error! Reference source not found.**

We now transform the right hand side of Eq. (21) from an average over a single bin (β_i, β_{i+1}) to that over a larger window (β_-, β_+) that encloses the bin:

$$0 = \phi(\beta) \langle E \rangle_\beta \Big|_{\beta_-}^{\beta_+} = \int_{\beta_-}^{\beta_+} d\beta \phi'(\beta) \langle E \rangle_\beta - \int_{\beta_-}^{\beta_+} d\beta \phi(\beta) \langle \Delta E^2 \rangle_\beta, \quad (22)$$

where $\phi(\beta)$ is a function that satisfies $\phi(\beta_-) = \phi(\beta_+) = 0$. We have also converted the difference to an integral, and used $\partial \langle E \rangle_\beta / \partial \beta = -\langle \Delta E^2 \rangle_\beta$.

We choose $\phi(\beta)$ as a superposition of a smooth $\phi_s(\beta)$ that spans over the entire window (β_-, β_+) and a local $\phi_l(\beta)$ limited in the bin (β_i, β_{i+1}) , see Fig. 2.1 and Eqs. (13) and (14), in which a_+ and a_- are nonnegative, and satisfy $a_+ + a_- = 1$. At $\beta = \beta_{i+1}$, the sudden jump in $\phi_s(\beta)$ is cancelled by that in $\phi_l(\beta)$; we therefore ignore the δ -functions in $\phi'_s(\beta)$ and $\phi'_l(\beta)$ in actual computation.

The purpose of the decomposition of $\phi(\beta)$ into $\phi_s(\beta)$ and $\phi_l(\beta)$ is to replace the average over a bin (β_i, β_{i+1}) in Eq. (21) by that over a larger window (β_-, β_+)

$$\tilde{E}_i = \frac{1}{\Delta\beta_i} \int_{\beta_i}^{\beta_{i+1}} d\beta \langle E \rangle_\beta = \int_{\beta_-}^{\beta_+} d\beta \left[\phi'_s(\beta) \langle E \rangle_\beta - \phi(\beta) \langle \Delta E^2 \rangle_\beta \right]. \quad (23)$$

The energy fluctuation $\langle \Delta E^2 \rangle_\beta$ is somewhat unreliable. To avoid this, we choose the a_+ and a_- such that

$$\int_{\beta_-}^{\beta_+} d\beta \phi(\beta) \langle \Delta E^2 \rangle_\beta = 0. \quad (24)$$

Solving Eq. (24) and $a_+ + a_- = 1$ yields a_+ and a_- , and thus $\phi'_s(\beta)$. So,

$$\tilde{E}_i = \int_{\beta_-}^{\beta_+} d\beta \phi'_s(\beta) \langle E \rangle_\beta. \quad (25)$$

Since $\phi'_s(\beta)$ is a constant within a bin, it can be moved out of the integral, and

$$\tilde{E}_i = \sum_j \phi'_s(\beta_j) \int_{\beta_j}^{\beta_{j+1}} d\beta \langle E \rangle_\beta = \sum_j \phi'_s(\beta_j) \Delta\beta_j \langle \langle E \rangle_\beta \rangle_j. \quad (26)$$

A comparison with Eq. (21) shows that Eq. (26) is just a linear combination of \tilde{E}_i 's obtained from different bins. The auxiliary function $\phi'_s(\beta)$ serves as the coefficients of combination, whereas Eq. (24) ensures the convergence.

The integral identity can be used for other quantities, such as the average energy, heat capacity, and energy histogram. Thus, we can calculate quantities at a single temperature, although the simulation is performed on the continuous range.

The formula for the average energy $\langle E \rangle_\beta$ is obtained by the limit $\beta_{i+1} \rightarrow \beta_i$ in Eq. (23). For the heat capacity $C(\beta) = k_B \beta^2 \langle \Delta E^2 \rangle_\beta$, we write

$$\langle \Delta E^2 \rangle_\beta = \int_{\beta_-}^{\beta_+} d\beta' \phi'(\beta') \langle \Delta E^2 \rangle_{\beta'} - \int_{\beta_-}^{\beta_+} d\beta' \phi(\beta') \langle \Delta E^3 \rangle_{\beta'}, \quad (27)$$

where we have substituted $-\langle \Delta E^3 \rangle_\beta$ for $\partial \langle \Delta E^2 \rangle_\beta / \partial \beta$.

For the energy histogram, we show in the appendix that the optimal $\phi(\beta)$ yields the continuous version of the multiple histogram method [54-56].

$$h_\beta(E, E + \Delta E) \equiv \int_E^{E+\Delta E} p_\beta(E') dE' = \frac{\int_{\beta_-}^{\beta_+} \int_E^{E+\Delta E} p(\beta', E') dE' d\beta'}{\int_{\beta_-}^{\beta_+} w(\beta') \frac{\tilde{Z}(\beta')}{\tilde{Z}(\beta)} \int_E^{E+\Delta E} \exp[-(\beta - \beta')E'] dE' d\beta'} , \quad (28)$$

where $h_\beta(E, E + \Delta E)$ is the energy histogram at β , which is equal to the integral of the joint temperature-energy distribution $p(\beta, E)$ over a small bin $(E, E + \Delta E)$.

For other quantities, we use

$$\langle A \rangle_\beta = \frac{\int_{\beta_-}^{\beta_+} A \exp[-(\beta - \beta')E] \tilde{Z}(\beta') / \tilde{Z}(\beta) d\beta'}{\int_{\beta_-}^{\beta_+} \exp[-(\beta - \beta')E] \tilde{Z}(\beta') / \tilde{Z}(\beta) d\beta'} , \quad (29)$$

where $\exp[-(\beta - \beta')E] \tilde{Z}(\beta') / \tilde{Z}(\beta)$ serves as the effective weight. Eq. (29) is unbiased even if $\tilde{Z}(\beta)$ has error.

2.2.5. Adaptive averaging

We use an adaptive averaging scheme to improve the convergence of $\tilde{E}(\beta)$ during equilibration. The idea is to assign large weights to new data points to refresh the average.

For a sample of size n , the normal average formula is $\langle A \rangle = S_A^{(n)} / S_1^{(n)}$, where

$S_A^{(n)} = \sum_{i=1}^n A_i$ is the sum of A and $S_1^{(n)}$ is the sample size n . To discount old data

points, we redefine $S_A^{(n)}$ and $S_1^{(n)}$ as

$$\begin{aligned} S_A^{(n)} &= \gamma^{n-1} A_1 + \gamma^{n-2} A_2 + \cdots + A_n, \\ S_1^{(n)} &= \gamma^{n-1} + \gamma^{n-2} + \cdots + 1, \end{aligned}$$

with $\gamma < 1$. The formula can be implemented as recursions,

$$\begin{aligned} S_A^{(n)} &= \gamma S_A^{(n-1)} + A_n, \\ S_1^{(n)} &= \gamma S_1^{(n-1)} + 1. \end{aligned} \tag{30}$$

With a constant γ , the sample size S_1 would saturate to a fixed value $1/(1-\gamma)$. To prevent this, we use

$$\gamma = 1 - C_\gamma / n, \tag{31}$$

to gradually increase γ to 1.0 (C_γ is a constant). In the end, the averaging scheme becomes the conventional one.

The adaptive averaging also accelerates the temperature space random walk. This is because it reduces the difference $E - \tilde{E}(\beta)$, which is the deterministic part of Eq. (10), by biasing towards recent data.

2.3. Verification

We first tested the method on a 32×32 Ising model [14]. Results from the alternative method of estimating $\tilde{E}(\beta)$, described in 2.6.2, were also included. Parameters common to the two methods were set to be the same.

The temperature range was $\beta \in (0.35, 0.55)$ or $T = (1.818, 2.857)$, which covered the critical temperature $T \approx 2.27$ of the phase transition. Here we used a

constant $w(\beta)$, or a flat- β histogram. The bin size was $\delta\beta = 0.0002$. For each (β_i, β_{i+1}) , the window for Eq. (26) was $(\beta_-, \beta_+) = (\beta_i - \Delta\beta, \beta_{i+1} + \Delta\beta)$ with $\Delta\beta = 0.02$; but near the boundaries, we used the largest possible $\Delta\beta$. The Langevin equation was integrated after every 100 Monte Carlo moves, with $\Delta t = 2.0 \times 10^{-5}$. The simulation was performed for 10^6 Monte Carlo steps per site.

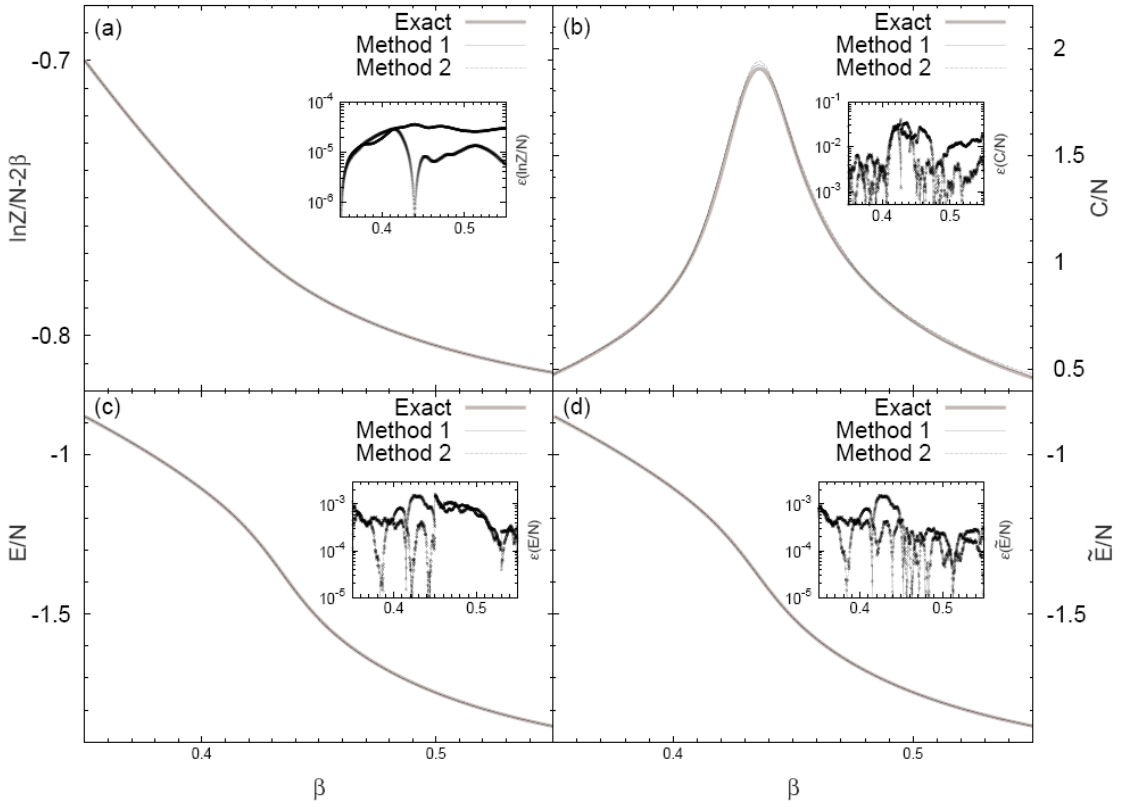


Figure 2.2. 32×32 Ising model. The method in 2.2 is labeled as Method 1, and that in 2.6.2 is labeled as Method 2. (a) Partition function, (b) heat capacity, (c) average energy, (d) $\tilde{E}(\beta)$.

The calculated partition function, average energy and heat capacity are shown in Fig. 2.2. The thin solid lines and dashed lines are for the method introduced in section II.D (method 1), and that described in 2.6.2 (method 2), respectively. In most cases, both results for the partition function and the average

energy coincide with exact results [14], see Figs. 2.2(a), 2.2(c), and 2.2(d). Even for the heat capacity, which is the second order derivative of the partition function and is harder to compute, the deviations in both cases are small. This indicates that the method is unbiased and it delivers exact thermodynamics quantities asymptotically.

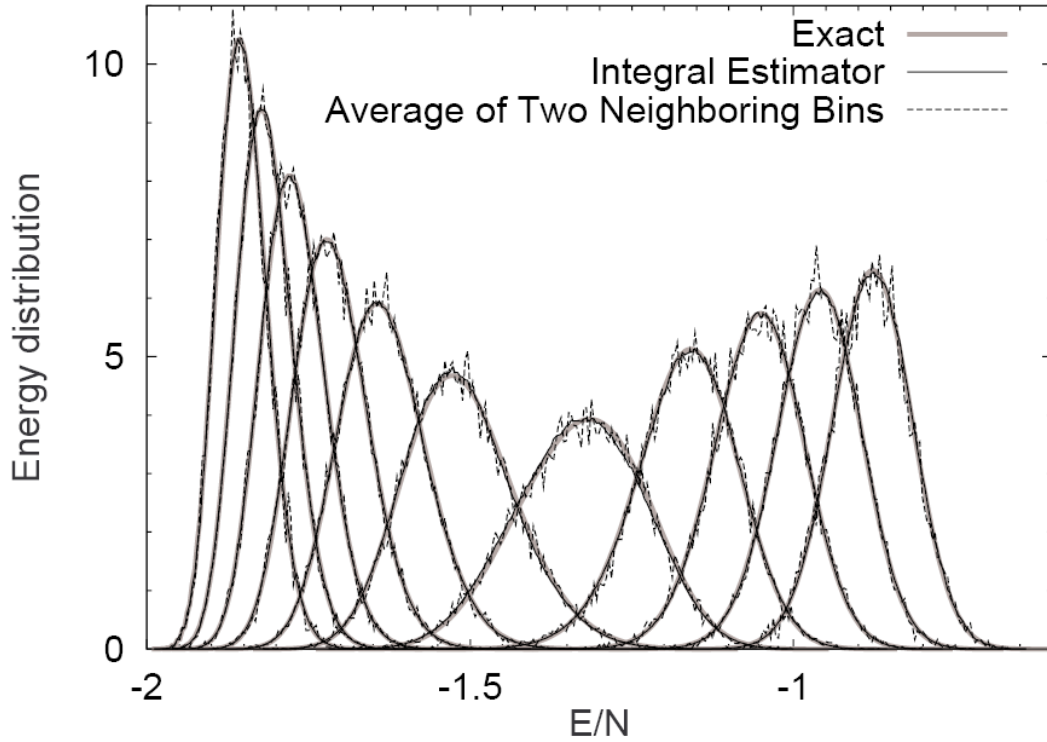


Figure 2.3. Reconstructed energy distribution at a few temperatures using Eq. (28) (solid), and results from averaging two neighboring bins (dashed). $\delta\beta = 0.0002$.

We can also show that the correct energy distribution can be reconstructed from Eq. (28). During simulation, the current potential energy was registered into the histogram every 100 Monte Carlo moves, thus there were roughly 10^5 samples in the entire histogram. The reconstructed energy distributions at representative temperatures are shown in Fig. 2.3. The temperature window for estimating the energy distribution at β was $(\beta - \Delta\beta, \beta + \Delta\beta)$ with $\Delta\beta = 0.02$. One can see a good

agreement between the integral identity Eq. (28), and the exact distribution, which was computed from the exact density of states [57]. For comparison, distributions constructed by averaging energy distributions of two neighboring bins yielded more noisy results.

2.4. Applications

We applied the method to the folding of several small proteins. The method was implemented in a modified GROMACS 4.0.6 [1-4], using AMBER force field ports [58] with TIP3P water model [59]. In all cases, the particle-meshed Ewald method [60] was used for handling long range electrostatic interaction, and the velocity-rescaling method was used as the thermostat [15]. For constraints, we used the SETTLE algorithm for water molecules [61], and the parallel LINCS algorithm [62] for proteins. As proteins drastically changed their configuration during simulation, dynamic load balancing was turned on when using domain decomposition.

All simulations were performed in a constant (N, V, T) ensemble. A 10 Å cutoff was used for Lennard-Jones interactions, electrostatic interactions and neighboring list. Since the temperature in our method is a variable, the temperature change was realized by scaling the force according to $\mathbf{F}' = (\beta/\beta_0)\mathbf{F} = (T_0/T)\mathbf{F}$, with \mathbf{F}' and \mathbf{F} being the scaled and the original force, respectively (see 1.4.3). On the other hand, the thermostat temperature T_0 , which controls the kinetic energy, is unaffected and can be maintained at a fixed value $T_0=480$ K. Three separate

thermostats were applied to protein, solvent and ion groups, and the coupling time τ_T for the thermostats was 0.1 ps.

The MD time step was 0.002 ps. The center of mass motion was removed every step. Trajectory was saved every 2 ps. Since the force and energy calculation was much more time-consuming than estimating $\tilde{E}(\beta)$, we applied the Langevin equation in every MD step using an integrating step of $\Delta t = 10^{-4}$. The parameter C_γ in adaptive averaging Eq. (31) was 0.1 in all cases.

2.4.1. Trpzip-2

The first system was a 12 amino acid β -hairpin tryptophan zipper, whose Protein Data Bank (PDB) ID code is 1LE1, and its sequence is SWTWENGKWTWK [63]. A unique feature of this short hairpin is that its four tryptophan side chains form a pattern that stabilizes the structure.

Previously, the system was intensively studied both in explicit [64, 65] and implicit solvent [66-71]. But *de novo* folding in explicit solvent from an extended chain, see Fig. 2.4(a), is more challenging. We used AMBER99SB as the force field, which updated the φ and ψ dihedrals [72] of the AMBER99 force field [73].

We report four simulation trajectories. All of them reached atomic accuracy within in a time scale of 1 μ s. We used a cubic 45 \times 45 \times 45 \AA^3 box, filled with 2968 water molecules as well as two Cl^- ions. The β range was (0.20,0.41), which corresponded to $T = 293.6\text{K}\sim 601.9\text{K}$. The grid spacing for Fourier transform was 1.15 \AA , and the alpha parameter was 0.3123 \AA^{-1} for the Ewald method. For the

integral identities Eqs. (26), (27) and (28), the window was $(\beta - \Delta\beta, \beta + \Delta\beta)$, with $2\Delta\beta$ was 8% of β , e.g., at $\beta = 1.0/(k_b 500\text{K}) \approx 0.241$, $\Delta\beta = 4\% \times \beta \approx 0.010$, so $T = (480.8, 520.8)$ K. At boundaries, we used the largest possible $\Delta\beta$ that permits a symmetrical window.

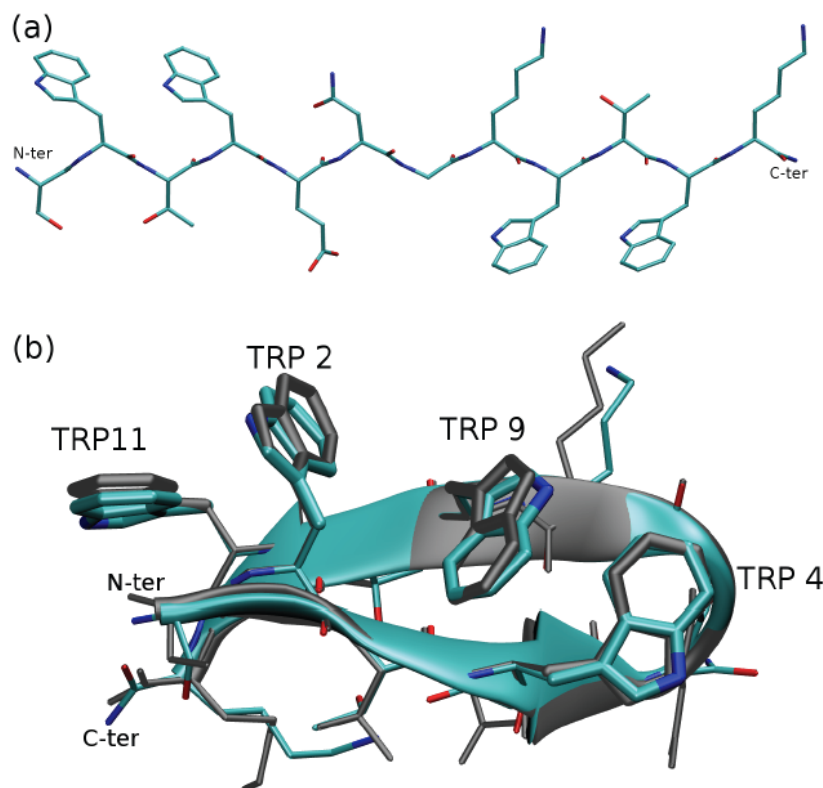


Figure 2.4. Trpzip2. (a) Initial extended conformation; (b) a typical folded structure. The C_α - and the all heavy atom RMSDs are 0.25Å and 1.08Å respectively. Gray: native.

Table 2.1. Lowest RMSDs in folding trajectories of trpzip2.

Traj. ID	C_α -RMSD (Å)	Heavy atom RMSD (Å)	t_1 (ns) *
1	0.20	1.00	20
2	0.25	0.84	520
3	0.20	0.88	530
4	0.25	1.31	1080

* First time of stably reaching atomic accuracy of the native state (C_α -RMSD < 0.5 Å).

The snapshot of reaching the lowest C_α -RMSD can differ slightly from that of reaching the lowest heavy atom RMSD.

A typical folded structure is shown in Fig. 2.4(b), with its root mean square deviations (RMSD) for alpha-carbon (C_α) and heavy atoms being 0.25 Å and 1.08 Å, respectively. The lowest C_α and heavy atom RMSD found in the four trajectories are listed in Table 2.1. Even among structures with lowest RMSDs, tryptophan side-chains can still adopt different conformations. For example, in trajectories 1 and 3, there were native-like structures with one of the tryptophan side-chain (TRP9 or TRP4) flipped 180° with respect to the native conformation. We also show the time series of trajectories 1 and 3 in Fig. 2.5.

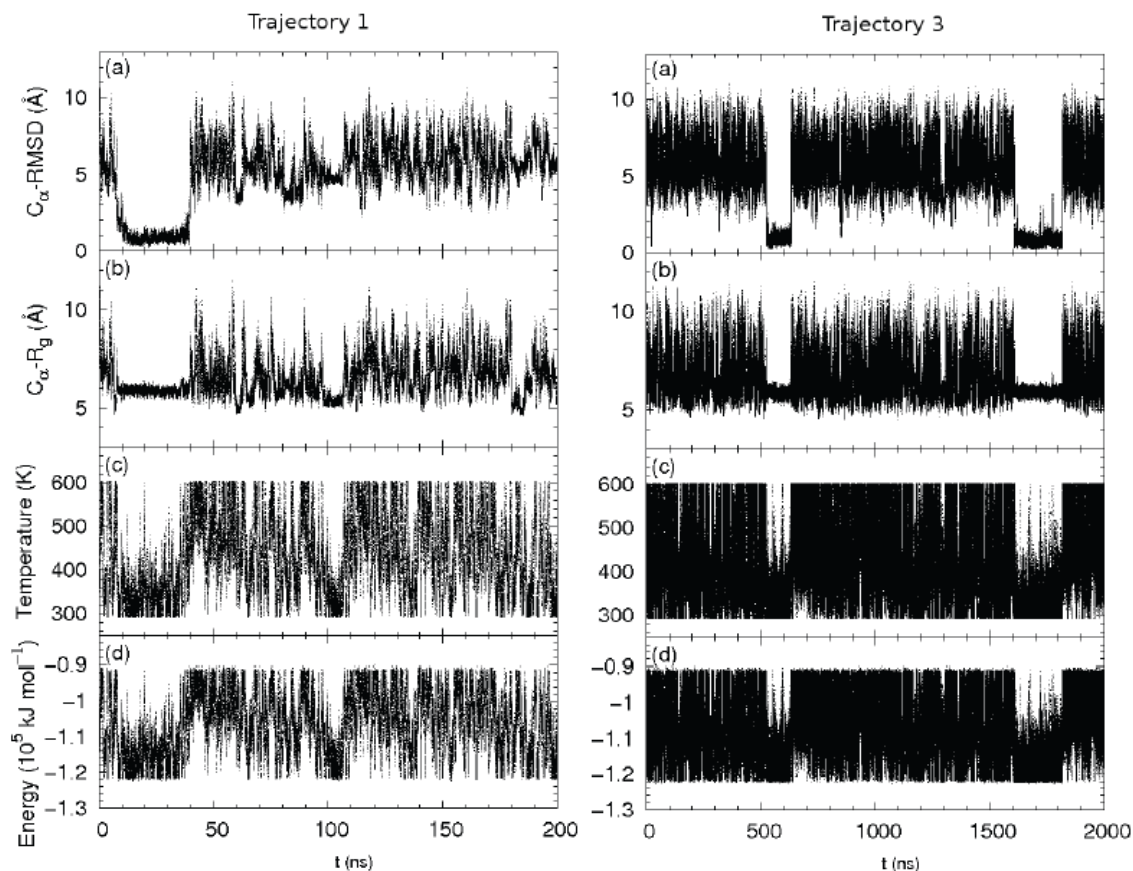


Figure 2.5. Trpzp2. Left: the first 200 ns of trajectory 1. Right: trajectory 3. (a) C_α -RMSD from the native structure, (b) C_α radius of gyration, (c) temperature, (d) potential energy.

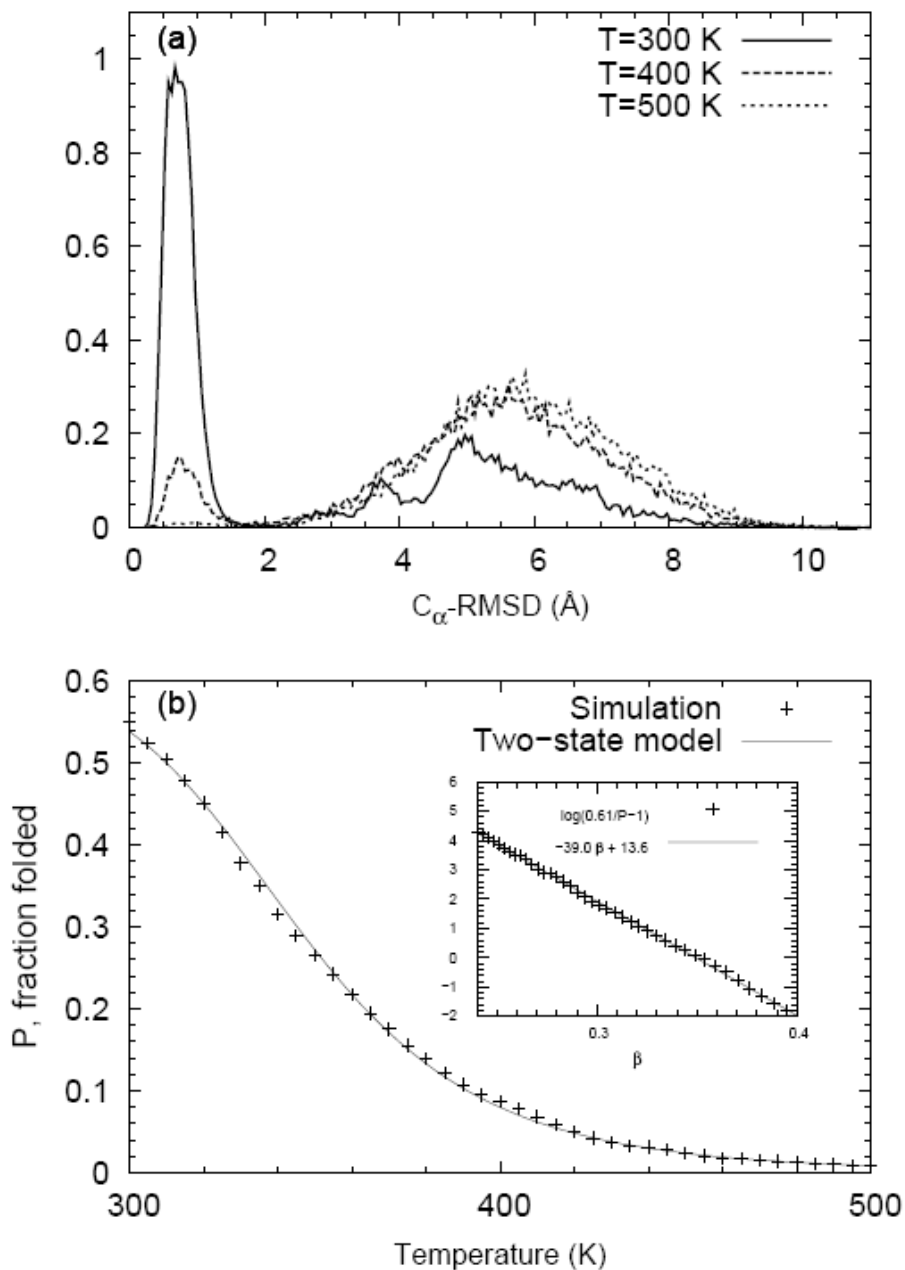


Figure 2.6. Trpzip2. (a) RMSD distribution; (b) fraction P of the folded state. Inset: linear fitting of $\log(P_0/P - 1)$ versus β to the two-state model.

Fig. 2.6(a) shows the distribution along the C_α-RMSD at three different temperatures calculated from trajectory 3. The distribution shows a two-peak structure, corresponding to the folded and the unfolded states, respectively.

The folding temperature can be computed by assuming a two-state model. The folding fraction $P(\beta)$ was first calculated as the fraction of states with C_α -RMSD less than 2.0 Å at different β . $P(\beta)$ was then fitted against a two-state model in the range $\beta \in (0.24, 0.4)$, or $T \in (300.9 \text{ K}, 501.5 \text{ K})$, as

$$P = \frac{P_0}{1 + \exp[\Delta E(\beta_m - \beta)]}, \quad (32)$$

where the parameters were $P_0 = 0.61$, $\Delta E = 38.96 \text{ kJ}\cdot\text{mol}^{-1}$, and $\beta_m = 0.350 \text{ kJ}^{-1}\cdot\text{mol}$, see Fig. 2.6(b). Here, ΔE is the energy difference between the folded state and the unfolded state; β_m is the melting temperature. In the simplest two-state model, the folding fraction should reach unity as the temperature approaches zero. But, here, the maximal fraction was changed from 1.0 to an adjustable parameter P_0 .

The enthalpy change ΔH was $39.0 \text{ kJ}\cdot\text{mol}^{-1}$ (ignoring the volume effect); and the entropy change $\Delta S = \beta_m \Delta E = 113 \text{ J}\cdot\text{mol}^{-1}$. The figures were too small compared with the experimental values $\Delta H^{\text{exp}} = 70.2 \text{ kJ}\cdot\text{mol}^{-1}$, $\Delta S^{\text{exp}} = 203.3 \text{ J}\cdot\text{mol}^{-1}$ [63]. The computed folding temperature 344 K was, however, close to the experimental result 345 K [63]. Even from trajectory 3, which yielded the highest folding fraction, the fraction of folded states at 300 K was roughly 55%, which still differed significantly from the experimental value 91% [63]. For the other trajectories, the fractions were even smaller. The difference was likely because of insufficient sampling and/or force field inaccuracy.

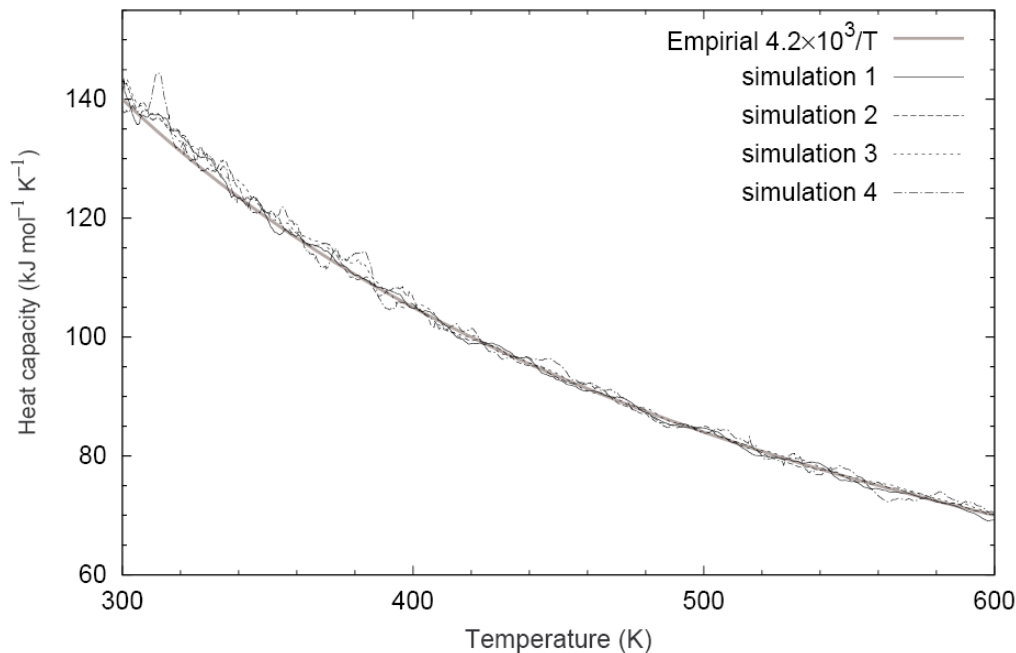


Figure 2.7. Trpzip2: the heat capacity, computed from four independent trajectories. Bold solid line: empirical formula $C_V \approx 4.2 \times 10^3 / T$.

Fig. 2.7 shows the heat capacity C_V versus temperature from Eq. (27). The difference among trajectories was small, suggesting convergence. We also observe that $C_V \approx 4.2 \times 10^3 / T$ kJ·mol⁻¹·K⁻¹. This highlights the strong electrostatic interaction that makes the system resemble an electrolyte [74].

2.4.2. Trp-cage

The second application was a 20 amino acid alpha helical protein, tryptophan cage (trp-cage) [75]. The PDB code is 1L2Y, and the amino acid sequence is NLYIQWLKDGGPSSGRPPPS. It was extensively studied by experiments [75, 76] and simulations, either in explicit [77-79] or implicit solvent [68, 80-84]. We again used AMBER99SB as the force field [72].

We simulated the system in a cubic $46 \times 46 \times 46 \text{ \AA}^3$ box, filled with 3161 water molecules and a Cl^- ion. The grid spacing for Fourier transform was 1.19 \AA , and the alpha parameter was 0.3123 \AA^{-1} . The initial structure was an open chain, as shown in Fig. 2.8(a).

We report three independent $1 \mu\text{s}$ simulation trajectories. The temperature range for trajectory 1 was $\beta \in (0.24, 0.41)$, or $T \in (293.6 \text{ K}, 501.5 \text{ K})$. In trajectories 2 and 3, we used $\beta \in (0.20, 0.41)$, or $T \in (293.6 \text{ K}, 601.9)$. The bin size $\delta\beta$ was 0.0005, 0.0005 and 0.0002, respectively. For the integral identity, the temperature windows were 10%, 10% and 8% of β for trajectories 1, 2, and 3, respectively. In all cases, we used the alternative estimator introduced in 2.6.2.

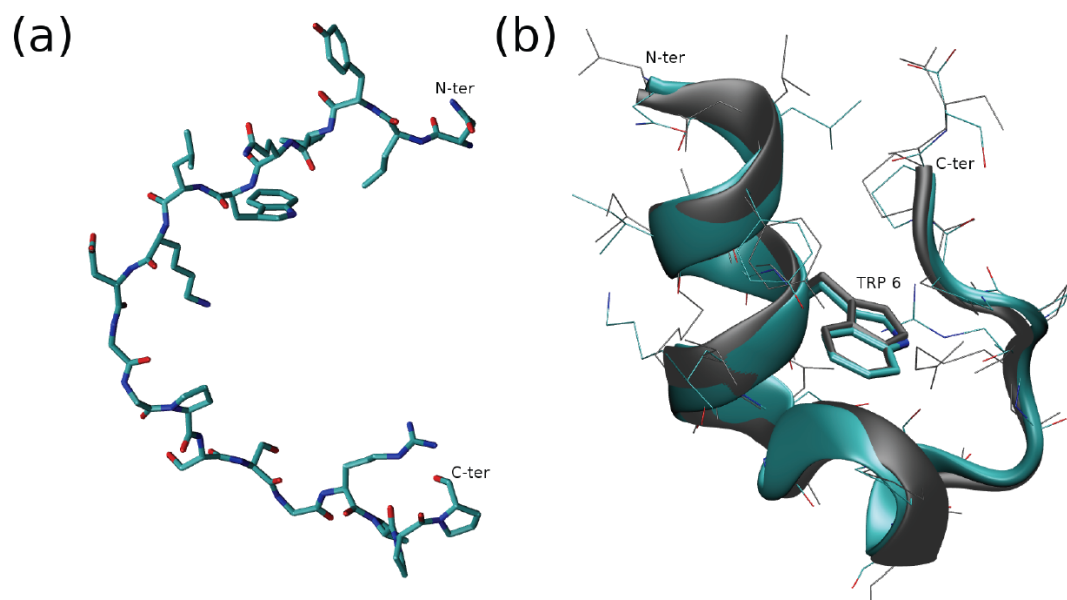


Figure 2.8. Trp-cage. (a) Initial structure; (b) typical folded structure. The C_α and all heavy atom RMSDs were 0.44 \AA and 1.54 \AA respectively. Gray: native.

All simulations independently reached the native state. A typical folded structure in trajectory 1 is shown in Fig. 2.8(b). The minimal alpha-carbon root

mean square deviations (C_{α} -RMSDs) from the three trajectories were 0.43 Å, 0.48 Å, and 0.44 Å respectively. The average C_{α} -RMSD for the native state was around 0.8 Å. The lowest RMSDs for all heavy atoms were 1.34 Å, 1.47 Å and 1.46 Å, respectively.

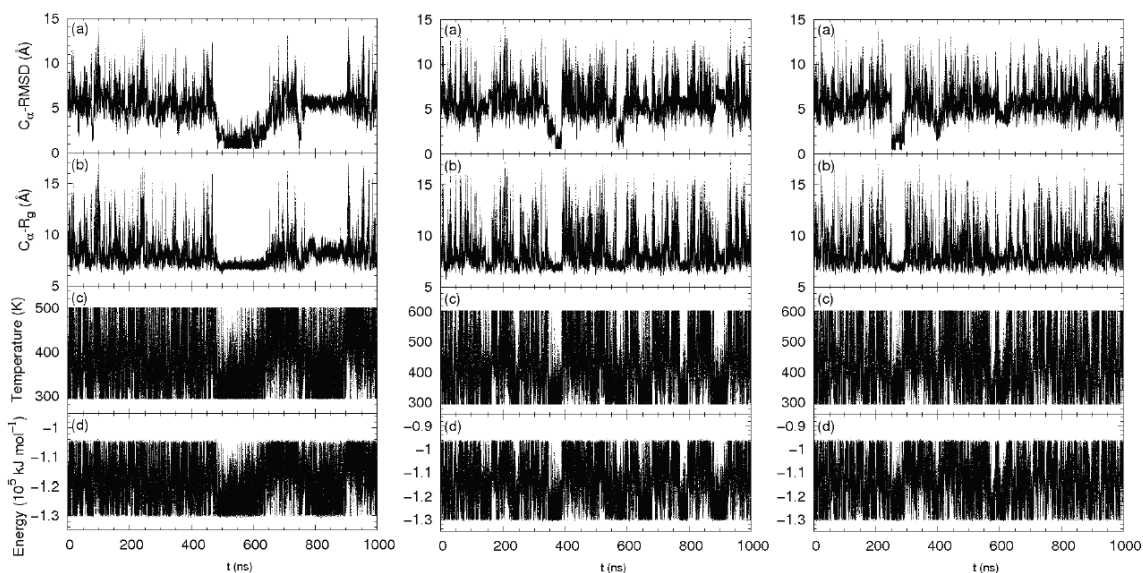


Figure 2.9. Trp-cage. (a) C_{α} -RMSD; (b) C_{α} radius of gyration; (c) temperature; (d) potential energy.

The C_{α} -RMSD, radius of gyration, instantaneous temperature and potential energy along trajectory are shown in panels (a), (b), (c) and (d), respectively, of Fig. 2.9, for the three independent simulations. In each trajectory, there were two folding events reaching an atomic accuracy. For the folding speed, it appears that simulations 2 and 3, with a higher $T_{\max} = 600\text{K}$, found the native structures sooner than simulation 1, whose $T_{\max} = 500\text{K}$. But in simulation 1, the system was able to stay in the native states longer.

Trajectory 1 yielded the largest fraction of the folded state at 300 K, 19%, which was much lower than experiment value 70% [75, 85]. By fitting the folding fraction, computed from the fraction of states with C_{α} -RMSD less than 2.2 Å, to the

two-state formula Eq. (32), the parameters were $P_0 = 0.50$, $\Delta E = 21.1 \text{ kJ}\cdot\text{mol}^{-1}$, and $\beta_m = 0.367 \text{ kJ}^{-1}\cdot\text{mol}$. The enthalpy change is thus $\Delta H \approx 21 \text{ kJ}\cdot\text{mol}^{-1}$, which was relatively small compared with the experimental values $\Delta H^{\text{exp}} = 56.2 \text{ kJ}\cdot\text{mol}^{-1}$ [85]. The computed folding temperature $T_m = 328 \text{ K}$, was higher than the experimental result 315 K [85].

2.4.3. Villin headpiece

The last application was the villin headpiece, a 36 residue helical protein HP36. The PDB ID is 1VII, and the amino acid sequence is **MLSDEDFKAVFGMTRSAFANLPLWKQQLKKEKGLF**. This system was the first protein partially folded in explicit solvent [36]. Recently, a high resolution crystal structure of slightly modified protein HP35, PDB ID 1YRF, was available [86], and its sequence is **LSDEDFKAVFGMTRSAFANLPLWKQ**HL**KKEKGLF**, in which the N-terminal Met is removed and the 28th residue Asn was replaced by His. Both sequences were studied, by either simulations [41, 87-91] or experiments [92, 93]. However, the NMR structure of HP36 differed from the x-ray structure of HP35 by 1.62 \AA in C_α -RMSD.

We chose AMBER03 [94] as the force field, which was previously used to fold HP35 in implicit solvent [88]. We used a dodecahedron simulation box with edge length being 24.1 \AA to accommodate the protein as well as 3343 water molecules, and two Cl^- ions. The volume of the box was $53.3 \times 53.3 \times 37.6 \text{ \AA} = 1.069 \times 10^5 \text{ \AA}^3$. The initial conformation was a fully-extended chain, see Fig. 2.10(a). The grid spacing for Fourier transform was 1.19 \AA , and the alpha parameter was 0.3123 \AA^{-1} .

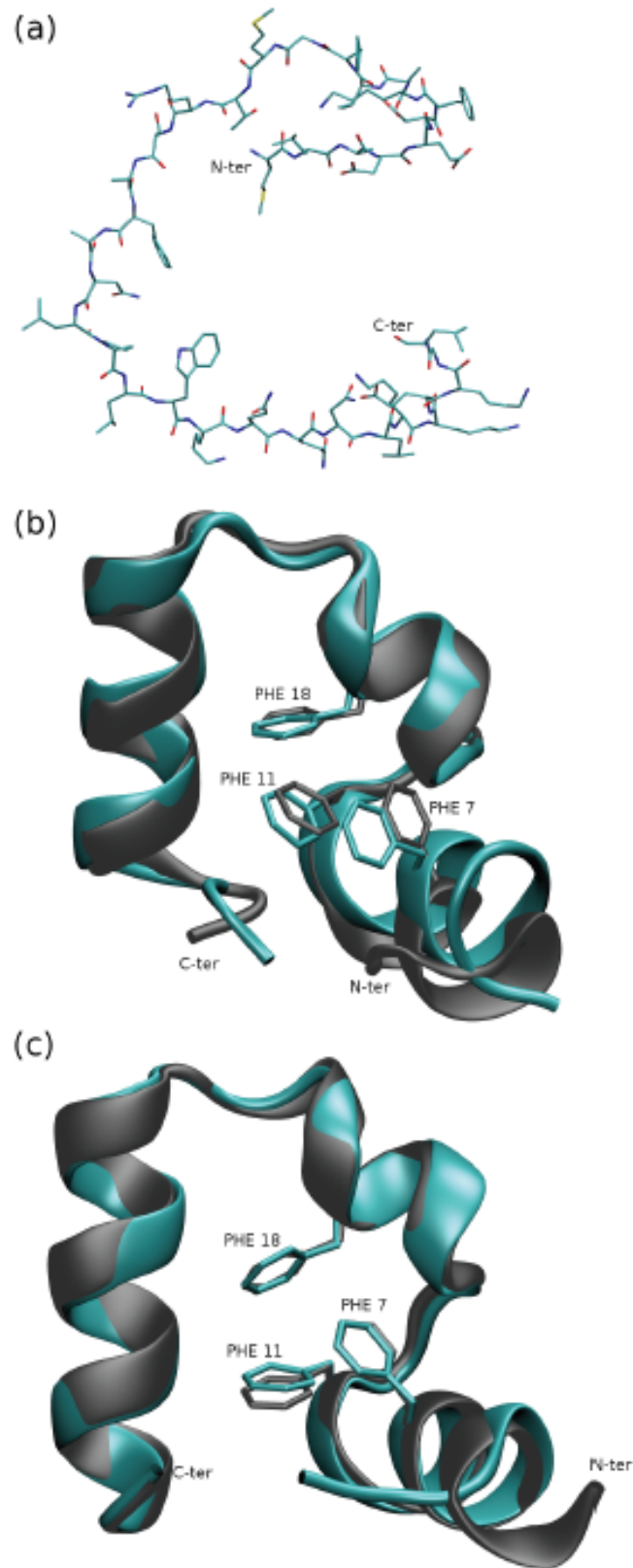


Figure 2.10. Villin headpiece. (a) Initial structure; (b) and (c) structures closest to the NMR (1VII) and x-ray (1YRF) structures (gray), respectively.

We report two 1 μ s simulation trajectories. In trajectory 1, $\beta \in (0.18, 0.41)$. In trajectory 2, $\beta \in (0.20, 0.41)$. The bin size $\delta\beta = 0.0002$. The windows size $2\Delta\beta$ for the integral identity was 8% of β .

The alpha-carbon root mean square deviation (C_{α} -RMSD) was computed from the NMR and x-ray structures. In both cases, the N-terminal Met and Leu as well as the C-terminal Phe were not included in the calculation [95]. We further exclude terminal flexibility, by computing C_{α} -RMSD for residues 9 to 32 of HP36 [36, 87], denoted as $\text{RMSD}_{\text{core}}$. Note: even for C_{α} - $\text{RMSD}_{\text{core}}$, there was an 0.87 Å difference between the NMR and x-ray experimental structures.

Table 2.2. Lowest RMSDs in folding trajectories of villin headpiece.

Traj. ID	$\text{RMSD}_{\text{core}}$ (NMR)	RMSD (NMR)	$\text{RMSD}_{\text{core}}$ (x-ray)	RMSD (x-ray)	t_1 (ns) *
1	0.72	1.32	0.30	0.42	310
2	0.78	1.16	0.36	0.66	26

* First time of reaching atomic accuracy of the native state

The frame reaching the lowest C_{α} -RMSD differed slightly from that reaching the lowest heavy atom RMSD.

We list the lowest C_{α} -RMSDs in the two simulations in Table 2.2. The lowest C_{α} - $\text{RMSD}_{\text{core}}$ from the NMR structure were 0.72 Å and 0.78 Å. The figures were smaller than those from a previous study on HP36, in which the lowest $\text{RMSD}_{\text{core}}$ was around 1.5 Å [87]. In both cases, the best folded structures were more similar to the x-ray structure than to the NMR one, even though we simulated the latter.

Table 2.2 also lists the first time of reaching the native structure. In both cases, the time (310 ns for trajectory 1 and 26 ns for trajectory 2) was significantly shorter than those in a very recent study (where the folding occurs in 5 to 6 μ s) [41].

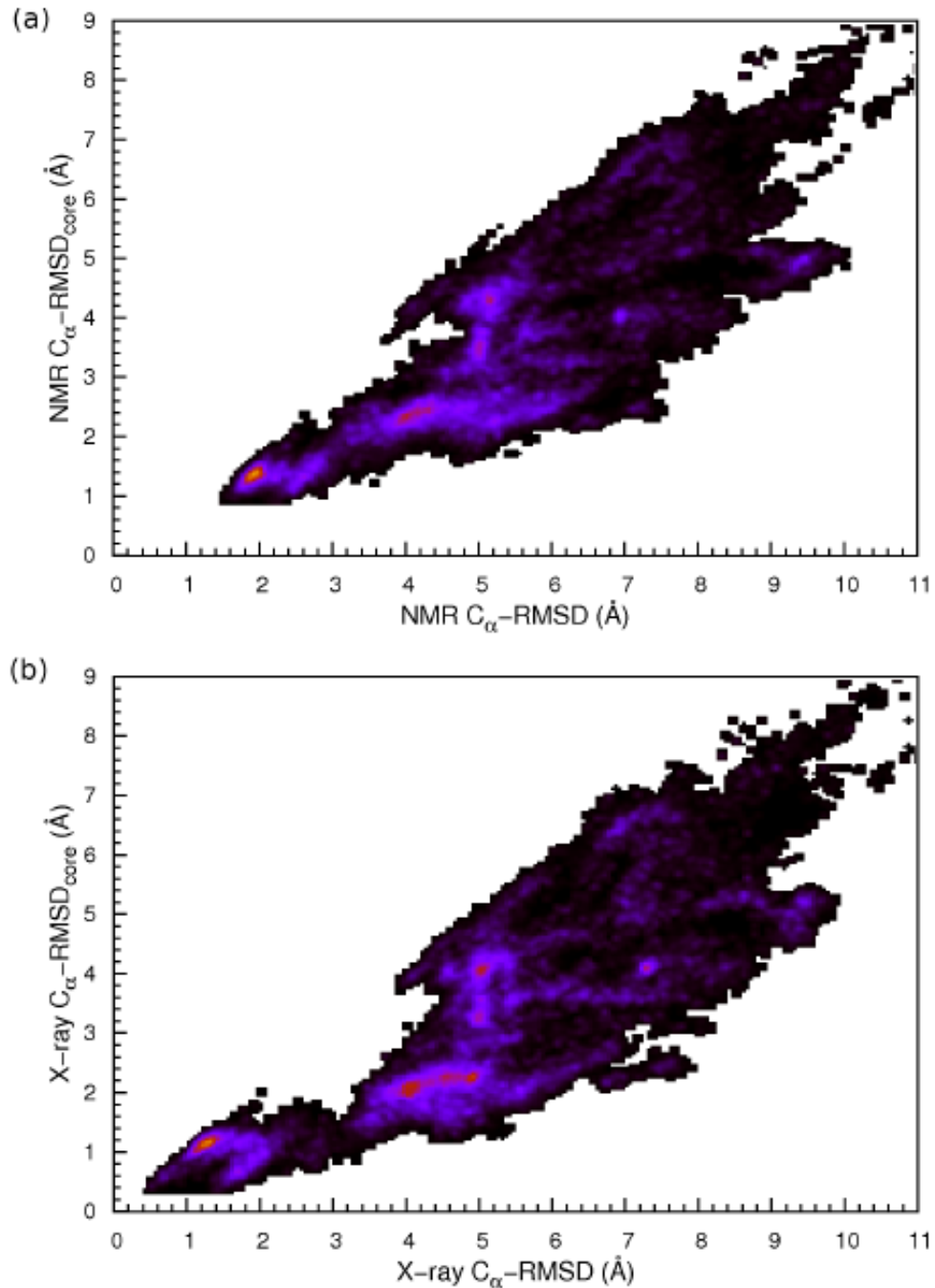


Figure 2.11. Villin headpiece. Joint distributions of C_{α} -RMSD and C_{α} -RMSD_{core} (from residues 9~32). References: (a) NMR ; (b) x-ray.

In Figs. 2.10(b) and 2.10(c), we show the superposition of typical folded structures to the NMR and x-ray structures, respectively, from simulation 1. The

position of the N-terminal helix differed appreciably from the NMR native structure, whereas the difference was much smaller compared with the x-ray structure.

Fig. 2.11(a) and (b) show the C_{α} -RMSD_{core} versus the C_{α} -RMSD for the NMR and x-ray reference structures, respectively. The native state had larger RMSD from the NMR structure than from the x-ray one.

The folding fraction, computed from the C_{α} -RMSD from the x-ray structure with a 3.0 Å cutoff, was fitted against Eq. (32). The parameters were $P_0 = 0.21$, $\Delta E = 20.9 \text{ kJ}\cdot\text{mol}^{-1}$, and $\beta_m = 0.349 \text{ kJ}^{-1}\cdot\text{mol}$. The enthalpy change $\Delta H = 20.9 \text{ kJ}\cdot\text{mol}^{-1}$, and the folding temperature $T_m = 345 \text{ K}$. Although the latter agreed well with the experimental value 342 K, the former was too small: $\Delta H^{\text{exp}} = 113 \text{ kJ}\cdot\text{mol}^{-1}$ [92].

2.5. Conclusions and Discussions

A single-copy enhanced sampling method was successfully applied to folding three small proteins, trpzip2, trp-cage and villin headpiece, in explicit solvent. We reversibly reached accurate native structures in an order of a microsecond.

The computed folding enthalpy and folding temperature still showed discrepancies from experimental results. This was likely due to insufficient sampling in limited simulation time or errors in the force field [96].

2.6. Appendix

2.6.1. Fokker-Planck equation

We derive the Langevin equation Eq. (10) below. First, if τ satisfies

$$\frac{d\tau}{dt} = A(\tau) + \sqrt{2}B(\tau)\xi,$$

where ξ is a white noise satisfying $\langle \xi(t)\xi(t') \rangle = \delta(t-t')$, then the distribution of τ satisfy the following Fokker-Planck equation [97]

$$\frac{\partial \rho(\tau)}{\partial t} = \frac{\partial}{\partial \tau} [-A(\tau)\rho(\tau)] + \frac{\partial^2}{\partial \tau^2} [B(\tau)^2 \rho(\tau)].$$

The stationary distribution of $\partial \rho(\tau)/\partial t = 0$ is

$$\rho(\tau) = \frac{1}{B(\tau)^2} \exp \left[\int^\tau \frac{A(\tau')}{B(\tau')^2} d\tau' \right].$$

Eq. (10) can be written as $d(1/\beta)/dt = -d \log p(\beta, \mathbf{x})/d\beta + \sqrt{2}(1/\beta)\xi$, since

$-\partial \log p(\beta, \mathbf{x})/\partial \beta = E + \partial \log \tilde{Z}(\beta)/\partial \beta - \partial \log w(\beta)/\partial \beta$. We therefore identify

$\tau = 1/\beta$, $A = -d \log p(\beta, \mathbf{x})/d\beta$, and $B = \tau = 1/\beta$. So

$$\rho(\tau) = \frac{1}{\tau^2} \exp \left[\int^\tau \frac{d \log p(1/\tau', \mathbf{x})}{d\tau'} d\tau' \right] \propto \frac{1}{\tau^2} \log p(1/\tau, \mathbf{x}).$$

Finally, since $|\rho(\beta)d\beta| = |\rho(\tau)d\tau|$, and $d\tau = \tau^2 d\beta$, $\rho(\beta) \propto \tau^2 \rho(\tau) = p(\beta, \mathbf{x})$, which proves that Eq. (17) is the stationary solution.

2.6.2. Alternative fitting-based estimator

We used an alternative estimator for $\tilde{E}(\beta)$ based on linear extrapolation.

Let us first generalize Eq. (23). For

$$f(\beta) = \langle E \rangle_{\beta} + k(\bar{\beta}_i - \beta), \quad (33)$$

where $\bar{\beta}_i = (\beta_i + \beta_{i+1})/2$ and k is a constant, we have

$$\begin{aligned} \tilde{E}_i &= \frac{1}{\Delta\beta_i} \int_{\beta_i}^{\beta_{i+1}} d\beta \langle E \rangle_{\beta} = \frac{1}{\Delta\beta_i} \int_{\beta_i}^{\beta_{i+1}} d\beta f(\beta) \\ &= \int_{\beta_-}^{\beta_+} d\beta \phi'_s(\beta) f(\beta) + \int_{\beta_-}^{\beta_+} d\beta \phi(\beta) f'(\beta). \end{aligned} \quad (34)$$

where the linear term in Eq. (33) vanishes after the integral in the second step. Eq. (23) can be considered as a special case for $k = 0$.

Eqs. (33) and (34) allow a properly extrapolation for the average energy $\langle E \rangle_{\beta}$ from β to $\bar{\beta}_i$ before applying the integral identity, or the temperature averaging. If we assume that $\langle E \rangle_{\beta}$ is roughly linear function of β in the window (β_-, β_+) , the slope k of $\langle E \rangle_{\beta}$ vs. β can be obtained by linear regression as

$$k = \langle \Delta\beta\Delta E \rangle_+ / \langle \Delta\beta^2 \rangle_+, \quad (35)$$

where the angular bracket $\langle \dots \rangle_+$ denotes an average over (β_-, β_+) .

Eq. (34) reduces the magnitude of the second integral and thus makes the estimator somewhat more robust. If the relation of $\langle E \rangle_{\beta}$ and β is perfectly linear,

$f'(\beta) = \partial \langle E \rangle_{\beta} / \partial \beta - k$ vanishes everywhere; so the second integral is zero.

In practice, we used a $\phi(\beta)$ parameterized with $a_+ = a_- = 1/2$, and restrain the magnitude of the second integral within $\sqrt{\langle \Delta E^2 \rangle_+}$ to ensure stability.

2.6.3. Overall temperature distribution

We used $w(\beta) \approx p(\beta) \sim 1/\beta$ for the overall temperature distributions. We justify the choice below. Consider the canonical energy distributions from two close temperatures. The peaks separation $|\Delta E| \approx \langle \Delta E^2 \rangle |\Delta\beta|$ should be proportional to the distribution width $\sqrt{\langle \Delta E^2 \rangle}$. So $|\Delta\beta| \propto \langle \Delta E^2 \rangle^{-1/2}$. But in the continuous ensemble, we have $p(\beta) \propto 1/|\Delta\beta|$, so

$$p(\beta) \propto \sqrt{\langle \Delta E^2 \rangle} \propto \sqrt{C}/\beta.$$

where we have used $\beta^2 \langle \Delta E^2 \rangle_\beta = C$, with C being the heat capacity.

For a Lennard-Jones like system, the heat capacity C is roughly a constant, accordingly the optimal $w(\beta)$ is proportional to $1/\beta$. On the other hand, protein simulations involve strong electrostatic interaction; and $C \propto \beta$, see Fig. 2.7. Thus, the optimal $w(\beta)$ should be proportional to $1/\sqrt{\beta}$. Although we still used $1/\beta$ for $w(\beta)$, which favored the high temperature end, the slightly suboptimal choice might be beneficial as it helped overcome broken ergodicity.

Chapter 3

Folding helical proteins

3.1. Introduction

The objective of this chapter is to present a modification of the tempering method introduced in the previous chapter for helical proteins. The contents are largely identical to those in reference [98].

The modification basically adds a temperature-dependent dihedral bias [40, 99, 100] to the generalized ensemble in a way that preserves the room temperature properties [42]. We folded four helical proteins of 67 to 102 amino acid residues, along with their mutants, by the method.

The four proteins in Protein Data Bank (PDB) are α_3 D (PDB ID: 2A3D, 73 residues) [101, 102], α_3 W (1LQ7, 67 residues) [103, 104], Fap1-NR $_{\alpha}$ (2KUB, 81 residues) [105] and S-836 (2JUA, 102 residues) [106]. The first three are parallel

three-helix bundles, and the last is a parallel four-helix bundle. Among the four, only Fap1-NR $_{\alpha}$ is a natural domain, the rest are artificially designed.

3.2. Dihedral-biased tempering

We sketch the methods below, see Appendix for details. We start with the continuous tempering method described in the previous chapter. The temperature T is a continuous variable in (T_L, T_H) covering the room temperature T_0 . Here, T_L is slightly below T_0 , while T_H is around 600K.

We now introduce a bias potential V through a temperature-dependent Hamiltonian, i.e., energy function, $H(T) = H_0 + (T/T_0 - 1)V$, where H_0 is the unbiased Hamiltonian. Since $H(T_0) = H_0$, unbiased room temperature T_0 properties can be recovered through a modification of the multiple histogram method [54-56].

The bias potential V specifically targets the two backbone dihedral angles, i.e., φ (C-N-C $_{\alpha}$ -C) and ψ (N-C $_{\alpha}$ -C-N), as they critically influence protein dynamics [40, 99, 100]. It is parameterized in terms of three intrinsic dihedral modes, one of which corresponds to the helical conformation. The magnitudes of the modes are adjustable in each trajectory. The bias potential V applies uniformly to all except glycine and proline residues.

The method was coded to GROMACS 4.0.7 [4]. We used a modified version [107] of AMBER03 [58, 94] as the force field (the modification slightly *reduced* helical content), TIP3P [59] as the water model, the particle-meshed Ewald (PME)

method [60] for long range electrostatic interaction, the velocity-rescaling method for thermostat [15]; SETTLE [61] and the parallel LINCS [62] as constraint algorithms for waters and proteins, respectively.

3.3. Results

3.3.1. Overview of folding of helical proteins

Protein sequences, simulation conditions and parameters for the dihedral bias are listed in Tables 3.1, 3.2 and 3.5, respectively. In Fig. 3.1, we show the structures with the lowest backbone root-mean-square deviations (RMSDs) 1.9 (α_3D), 1.4 (α_3W), 1.0 (Fap1-NR $_{\alpha}$), and 2.1 Å (S-836) from the respective experimentally-determined structures, which will be referred to as the “native” structures here. By comparison, the control simulations using regular MD starting from the native conformations yielded higher average RMSDs, 3.2, 2.2, 1.5, and 3.2 Å, respectively, at 300K, suggesting that the native state were stably reached.

Without using the experimental structures, cluster analyses (see 3.5.4) showed that the native conformations occupied the largest clusters in most trajectories for α_3D , α_3W , and S-836, see Table 3.5. For Fap1-NR $_{\alpha}$, the native conformation was, however, found in the second largest cluster, possibly due to limited sampling and/or force field inaccuracy.

Table 3.1. The amino acid sequences of α_3D , α_3W , Fap1-NR $_{\alpha}$, S-836 and the mutants.

Protein	Sequence
α_3D	MGSWAEFKQRLAAIKTRLQALGGSEAEAAFEKEIAAFESELQAYKKGKNPEVEALRKEAAAIRDQLQAYRHN
$\alpha_3D_L^\dagger$	MGSWEAFKQRLAAIKTRLQALGGSEAEAAFEKEIAAFESELQAYKKGKNPEVA <u>E</u> <u>A</u> <u>L</u> <u>E</u> <u>K</u> <u>R</u> <u>A</u> <u>A</u> <u>A</u> <u>I</u> <u>E</u> <u>D</u> <u>R</u> <u>L</u> <u>Q</u> <u>A</u> <u>Y</u> <u>N</u> <u>H</u> <u>R</u> [†] Residues different from α_3D are underlined.
α_3W	GSRVKALEEKVKALEEKVKALGGGGRIEELKKKWEELKKKIEELGGGGEVKKVVEEVKKLEEEIKKL
LQLQ	GSGLQQLQQQLQQQLQQQLQQLGSGGGLQQLQQQLQQQLQQQLQQLGSGGGLQQLQQQLQQQLQQQLQQQL
Fap1-NR $_{\alpha}$	ENLDKMISEAEVLNDMAARKLITLDAEQQLELMKSLVATQSQLEATKNLIGDPNATVADLQIAYTTLGNNTQALGN ELIKL
S-836	MYGKLNLDLLEDLQEVVKHVNQHWQGGQKNMNKVDHHLQNVIEDIHDQFMQGGGSGGKLQEMMKFEQQVLDEIKQQQLQ GGDNSLHNVHENIKEIFHHLEELVHR

For each protein, we show the time series of RMSD for a typical trajectory in Fig. 3.2. All simulations started from fully-extended conformations with large RMSDs. Folding and unfolding events, as indicated by the rises and falls of RMSD, typically occurred on a time scale of 0.5 to 2 μ s. We have accumulated around 10 folding events in each of α_3D , α_3W , and S-836, although longer and/or more simulations may be needed to further improve statistics.

Table 3.2. Simulation conditions for α_3D , α_3W , Fap1-NR $_{\alpha}$ and S-836 and the mutants.

Protein	PDB ID	$N_{res.}$	charge [§]	box [*]	N_{water}	RMSD _{bb} ^{min †}	RMSD _{bb} ^{300K ‡}	$t^{300K \#}$
α_3D	2A3D	73	-1	68	6989	1.9	3.2 \pm 0.2	410
α_3D_L		73	-1	68	6971	n/a	n/a	423
α_3W	1LQ7	67	+2	65	6055	1.4	2.2 \pm 0.3	436
LQLQ		67	0	65	6096	n/a	n/a	n/a
Fap1-NR $_{\alpha}$	2KUB	81	-6	70	7515	1.0	1.5 \pm 0.2	500
S-836	2JUA	102	+2	80	11440	2.1	3.1 \pm 0.4	400

[§] The total charge of the protein; sodium (Na⁺) and chloride (Cl⁻) ions were added to neutralize the respective system, e.g., two chloride ions were added to α_3W .

^{*} The box size represented by the side length of the bottom square of the dodecahedron in Å.

[†] The minimal backbone root mean square deviation (RMSD) in Å from the native structure. Since the experimental structures of the designed proteins α_3D_L and LQLQ are unknown, we put “n/a” there.

[‡] The average backbone RMSD in the native simulation performed at 300K using regular MD.

[#] The simulation time in nanoseconds using regular MD from the native conformation. No unfolding was observed in any of the studied proteins.

Since the simulation method used a variable temperature, only a fraction of trajectory frames were pertinent to the room temperature. We only report results after reweighted to 300K using the multiple histogram method [54-56], see 3.5.1.1.

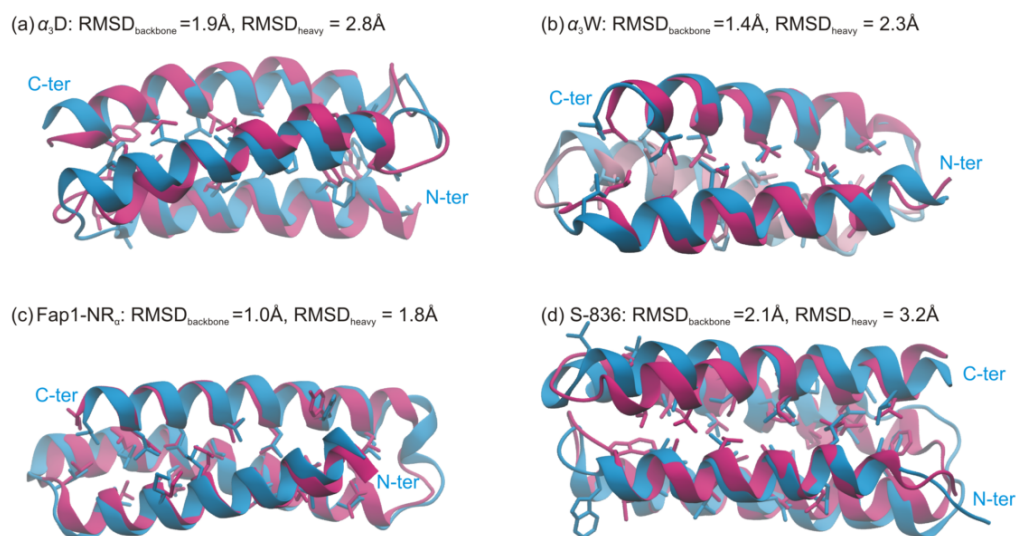


Figure 3.1. Best folded structures (blue) of four proteins. (a) α_3D , (b) α_3W , (c) Fap1-NR $_{\alpha}$, (d) S-836 compared with the respective NMR structures (red).

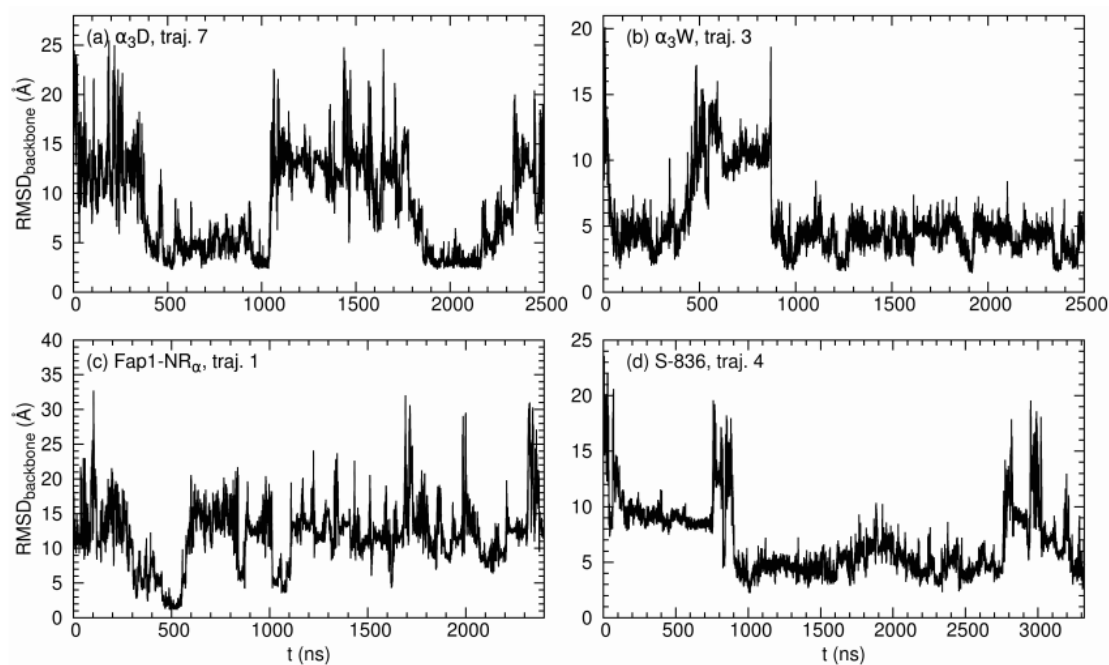


Figure 3.2. The backbone root-mean-square deviation (RMSD) versus time. (a) α_3D , (b) α_3W , (c) Fap1-NR $_{\alpha}$, (d) S-836.

3.3.2. Geometry of parallel helix bundles

Helical proteins present different ways of packing helices. We study two features in packing helices by using the three proteins α_3D , α_3W , S-836 as examples (we omit Fap1-NR $_{\alpha}$ as it is geometrically similar to α_3W , but was less well folded).

The first feature is the packing “chirality.” If a parallel three-helix bundle protein is viewed as three connected rods, after the first two helices are aligned, the third one can be packed against either side of the plane extended by the former two. We call the bundle right-handed, if the first helix, when viewed along the middle helix from N- to C-terminus, can be rotated clockwise to overlap with the third one by an angle less than 180°; or left-handed otherwise. A three-helix bundle of either chirality exists, e.g., α_3D is right-handed, while α_3W , Fap1-NR $_{\alpha}$ are left-handed.

Another feature is the helix orientation: although two successive helices are often aligned anti-parallel, a parallel alignment by a long loop is also possible.

From the folding trajectories, we found several compact but less stable nonnative conformations, which differed from the native one by the packing chirality or helix orientation. We wish to see what determines the natural geometry.

3.3.3. α_3D

We start with the first three-helix bundle α_3D [101, 102]. The three helices are labeled as A, B and C from N- to C-terminus. In Fig. 3.3(a), we show the distributions of the chiral distance D (see 3.5.3.2, positive for a right-handed bundle, negative a left-handed one) from three independent folding trajectories, as well as a

300K regular MD trajectory starting from the native structure. The distributions were dominated by a right-handed (native) peak around $D = 9\sim 10$ Å, coinciding with that at $D = 9.7$ Å from the native simulation.

The dominance of the right-handed conformation can be explained by the inter-helical charge interaction [101]. In the protein, residues in all three helices follow the heptad repeat $a-b-c-d-e-f-g$, see the left inset of Fig. 3.3(a), in which the a and d residues are hydrophobic, while the e and g ones charged or polar. The inter-helix interactions among the e and g residues help secure the skeleton.

For α_3D , the e and g residues on helix A are all positively charged, while those on helix B are negatively charged; on helix C, the e residues are positively charged but the g ones are negatively charged. In the center diagram of Fig. 3.3(a), we show schematically this charge interaction favors the right-handed conformation, but not the left-handed one.

We further show that the packing chirality can be reversed by a mutation, in which, we flipped the charges on the e, g residues of helix C through two local swaps: R57E-E59R, R64E-E66R (R57E means mutating Arg57 to Glu57). We also made three local swaps A5E-E6A, E54A-A55E, R71N-N73R to help stabilizing the left-handed conformation. The mutant is referred to as α_3D_L . A sequence comparison with α_3D is shown in the middle of Fig. 3.3.

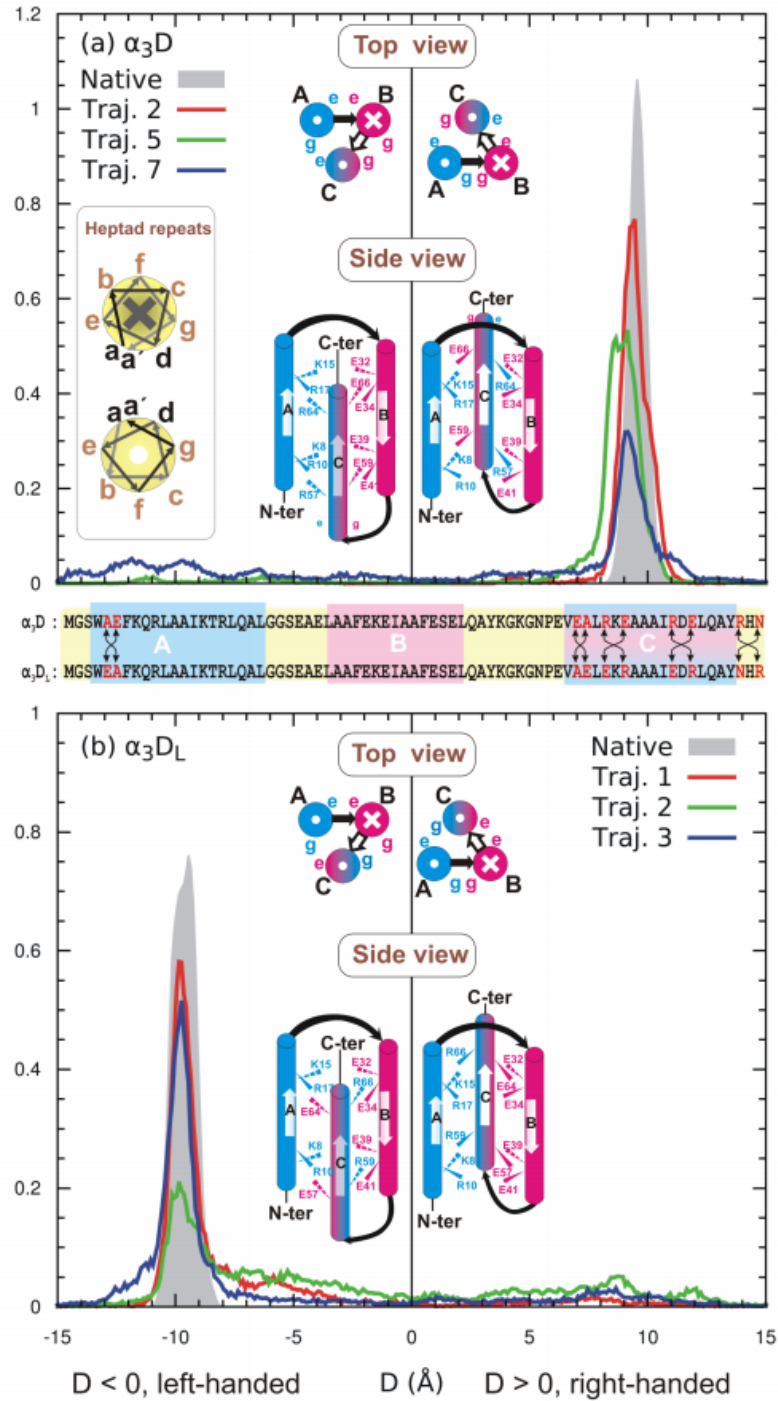


Figure 3.3. Packing-chirality D distributions for (a) α_3D and (b) a mutant α_3D_L . For α_3D , only the right-handed conformation exists, the left-handed one is hypothetical. The opposite is true for α_3D_L . Inset of panel (a): helix heptad. Crosses and dots in circles mean pointing into and out of the paper, respectively.

We simulated the mutant α_3D_L in three trajectories. As shown in Fig. 3.3(b), the left-handed conformation became dominant with a signature peak at $D = -9.7\text{\AA}$, while the right-handed one almost vanished. Cluster analyses confirmed that the left-handed conformation occupied the largest cluster in 300K.

Table 3.3. Geometry measures of various conformations of three-helical bundles.

	t (ns)	NC [§]	D_{ABC} [*]	d_{AB} [†]	d_{AC} [†]	d_{BC} [†]	θ_{AB} [‡]	θ_{AC} [‡]	θ_{BC} [‡]
α_3D , native	410	49±2	9.6±0.4	9.8±0.3	9.7±0.4	9.8±0.6	168±5	11±4	167±4
α_3D_L , native	423	50±2	-9.6±0.5	9.6±0.4	9.8±0.3	9.6±0.5	174±3	8±4	168±4
α_3W , native	436	49±2	-9.0±0.4	9.9±0.3	9.6±0.3	9.6±0.4	163±4	20±5	165±5
α_3W , conf. 2	240	40±3	9.6±0.6	9.6±0.5	9.3±0.5	10.0±0.4	152±10	20±8	168±5
α_3W , conf. 3	236	32±2	9.7±1.1	12.0±0.4	8.5±0.3	15.0±0.4	72±7	168±6	108±9
LQLQ, conf. 1	205	51±2	-9.4±0.3	9.6±0.2	9.8±0.3	9.4±0.3	165±4	14±3	172±4
LQLQ, conf. 2	216	51±2	9.8±0.4	9.2±0.3	10.2±0.9	9.6±0.8	171±4	13±5	165±5
LQLQ, conf. 3	197	47±2	9.1±0.5	10.6±0.6	9.2±0.4	10.2±0.5	29±8	160±4	165±6

[§] The total number of contacting hydrophobic residues between different helices with a 12Å cutoff distance.

^{*} The chiral distance in Å.

[†] The inter-helical distances in Å between helices A-B, A-C, and B-C.

[‡] The inter-helical angles in degrees between helices A-B, A-C, and B-C.

Residues that define helices A, B and C: for α_3D and α_3L , A: 4-21, B: 28-45, C: 53-70; α_3W , LQLQ, A: 4-21, B: 27-44, C: 50-67. Numbers followed ± are standard deviations.

We investigated the local stability of the mutant α_3D_L in comparison with that of the original α_3D . The cluster center from trajectory 1 was extracted and energy minimized as the putative native structure of α_3D_L . We then ran a separate 300K regular MD simulation starting from here for local properties, the local chiral distribution was shown as the shaded peak in Fig. 3.3(b). The average RMSD was 2.0 Å, which was comparable to that of α_3D , 2.1 Å, suggesting similar structural stability. Further, as shown in Table 3.3, the hydrophobic contact number, inter-helical distances and angles were similar to the native conformation of α_3D . Thus, the mutations might not affect the stability of the hydrophobic core significantly, and the charge interaction should be responsible for the chirality.

The comparison of α_3D and α_3D_L also suggested that the stability of the native right-handed conformation of α_3D was limited by the energy of a few favorable pairs of charged residues. Other energy contributions, such as hydrophobic interactions, were unlikely to inhibit the chirality flip.

3.3.4. α_3W

We now turn to the second protein α_3W (PDB ID: 1LQ7) [103, 104], which was previously simulated in implicit solvent [108-110]. Our trajectories, however, revealed in addition to the native conformation, two compact, geometrically different, albeit less populated, conformations.

Like α_3D , α_3W is also a parallel bundle of three helices, again labeled as A, B and C from N- to C-terminus. Its strategy to secure the chirality is similar to that of α_3D [103]: the heptad pattern is also followed in all three helices; the *e* and *g* residues on helix B are positively charged; those on helix C are negatively charged; the *e* and *g* residues on helix A are negatively and positively charged, respectively. As shown in the top inset of Fig. 3.4(a), the arrangement now favors the left-handed conformation.

The chiral distribution computed from the folding trajectories indeed had a prominent left-handed ($D < 0$) peak as well as a suppressed right-handed ($D > 0$) one, as seen in Fig. 3.4(a). The right-handed peak in fact covered two different conformations, both of which had corresponding clusters under cluster analyses, cluster centers are shown in Fig. 3.4(a). We ran respective 300K MD simulations

starting from the two nonnative conformations as well as the native one. The chiral distributions of the three conformations are shown as shaded peaks in Fig. 3.4(a).

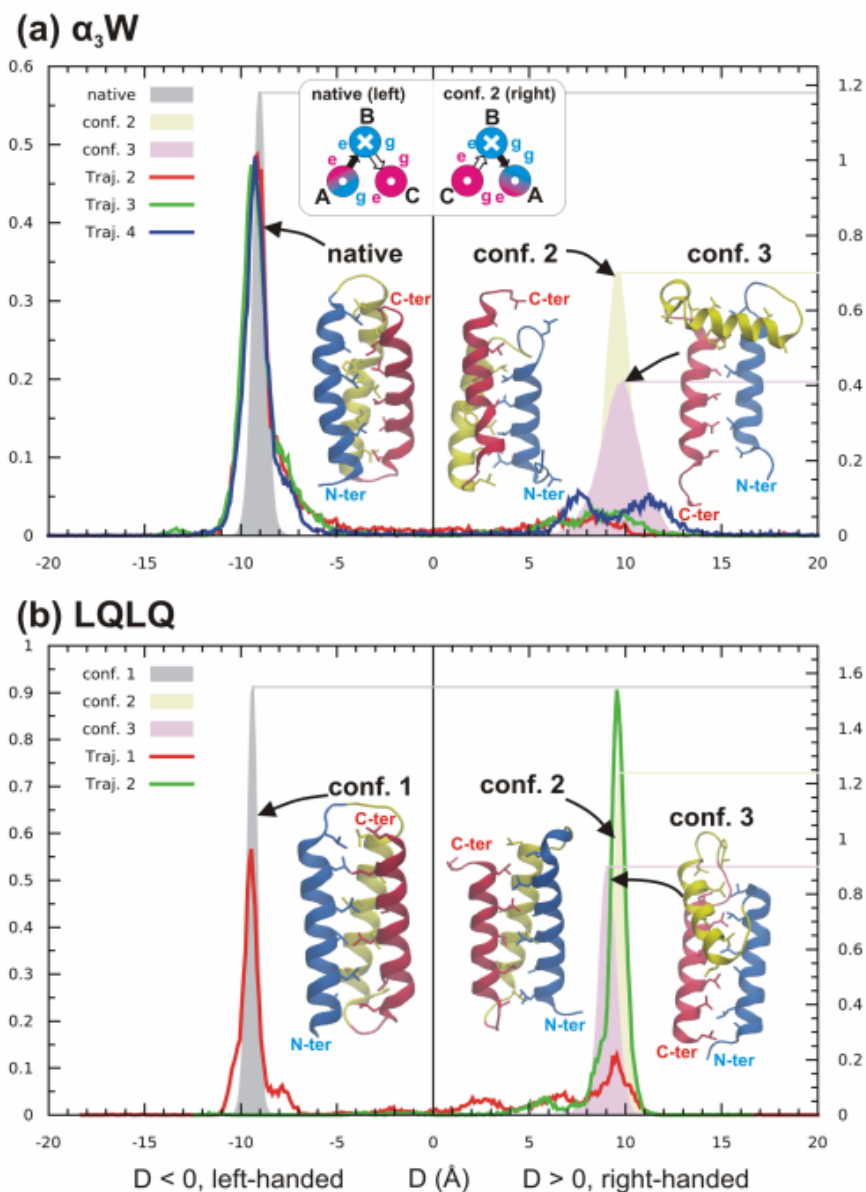


Figure 3.4. Packing-chirality D distributions for (a) α_3W and (b) LQLQ. The three helices are colored by blue, yellow and red, from N- to C-terminus. The shaded peaks (right scales) were obtained from regular MD started from the representative structures.

The first nonnative conformation (conf. 2), had the opposite chirality to the native one. The conformation had similar inter-helical distances and angles as the

native one, but a lowered contact number, from 49 (native) to 40, among hydrophobic residues, as shown in Table 3.3. The second nonnative conformation (conf. 3) differed from both the native one and conf. 2 by a reversely-oriented helix C, see Fig. 3.4(a).

We further demonstrate that if all charged residues on the helices were turned to polar or neutral ones, the protein can indeed switch among conformations of different geometries. We simulated a highly symmetric three-helix bundle, named LQLQ, in which all *a, d* residues were Leu's, and all *b, c, e, f, g* ones Gln's, in two independent trajectories. Cluster analyses revealed three clusters, referred to as conf. 1, 2, 3 below, as shown in Fig. 3.4(b).

Due to the symmetric sequence, conf. 1 and 2 (left- and right-handed, respectively) of LQLQ were geometrically similar, except the opposite chirality, as shown in Table 3.3. They represented the two most populated clusters with similar populations. Conf. 3 (a smaller cluster) was similar to, but more compact than the conf. 3 in α_3W , with the middle helix B being almost parallel, instead of orthogonal, to the other two helices.

3.3.5. S-836

The last protein is the four-helix bundle S-836 (PDB ID: 2JUA) [106]. The four helices are labeled as A, B, C and D from N- to C-terminus. In five trajectories, the total simulation time was 17 μ s, the first four reached the native conformation, while the last sampled two different nonnative ones.

To describe the geometry of the protein, we first extend the packing chirality for a three-helix bundle to a four-helix one. We view the four helices as two successive three-helix groups, A-B-C and B-C-D, each of which is thus equivalent to a three-helix bundle and has its own chirality. We partition the conformation space to four quadrants according to the signs of the two chiral distances D_{ABC} and D_{BCD} , denoted as LR ($D_{ABC} < 0$, $D_{BCD} > 0$), RR ($D_{ABC} > 0$, $D_{BCD} > 0$), RL ($D_{ABC} > 0$, $D_{BCD} < 0$) and LL ($D_{ABC} < 0$, $D_{BCD} < 0$). A quadrant is attached to either the native (LR) conformation, or some hypothetical one that differs from the native one only by chirality, e.g., the RR conformation differs from the native one by the chirality of the A-B-C helix group.

We computed the joint distribution of D_{ABC} and D_{BCD} after combining data from all trajectories. As shown in Fig. 3.5, the distribution revealed four major clusters. The four corresponding conformations were the native one (LR), conf. 2 (RR) and 3 (RL) and conf. 4 which differed from conf. 3 by a reversely-oriented helix A. Although the competing conformations existed, the native one still occupied the most populated cluster in the first four folding trajectories, and the population ratios to the first runner-up clusters were 2.1, 3.8, 1.1 and 1.9, respectively.

Except conf. 4 (which is not a chiral image of the native), the other three follow the order LR (native) > RR and RL (conf. 2 and 3) > LL (missing) by their populations. We attempt to explain the order by Fig. 3.6. LL was missing, possibly because of the inescapable repulsion between His83, His86, Lys90, His94 on helix D and Lys32, His36 on helix B (all His's were positively charged). Helices A and D in

the RL conformation encountered a similar but less severe problem, causing a kink in helix D to avoid direct repulsion between His86 and Lys17. Unfavorable interactions between helices B and D in RR could bend or dislocate helix D. LR (native) appeared to have the best pairing pattern, although unfavorable contacts existed, e.g., Glu91 and Asp11.

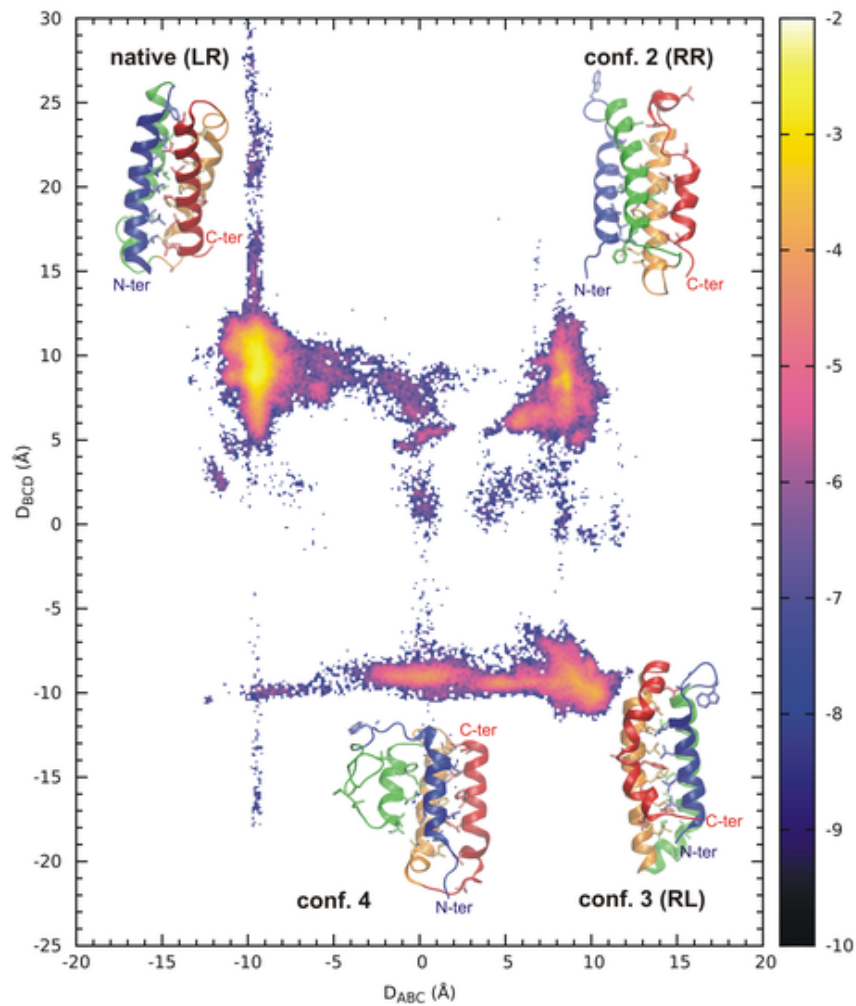


Figure 3.5. The logarithm of the packing-chirality distribution $\log \rho(D_{ABC}, D_{BCD})$ of S-386. The colors of the four helices are blue, green, orange, and red, sequentially, from N- to C-terminus in representative structures.

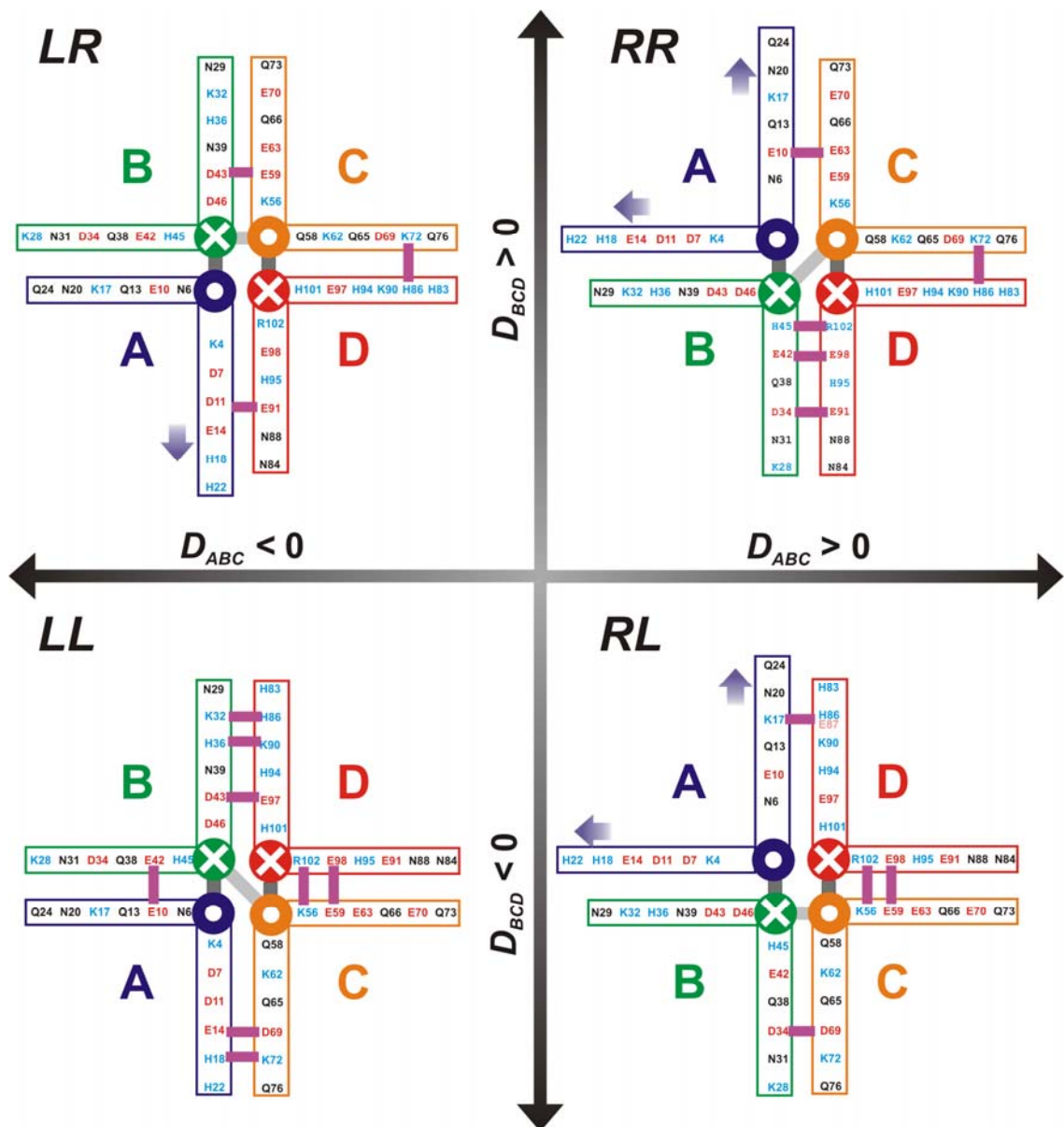


Figure 3.6. Packing patterns of the chiral images of S-836. LR, RR, RL and LL are classified by the signs of D_{ABC} and D_{BCD} . Only the first three were observed. Interactions of charged/polar residues between two helices are shown as two aligned arms with residues on the interface. Magenta bars: unfavorable interactions. Helix sliding are indicated by blue arrows.

In Nature, four-helix bundles adopting the RR, RL, and LL conformations do exist. In fact, the majority, e.g., cytochrome *c*' (PDB ID: 3ZTM) [111] and cytochrome *b*₅₆₂ (PDB ID: 1QPU) [112], adopt the RL conformation, the opposite of the native LR conformation of S-836. Two examples of the RR and LL conformations are the C-

terminal domain of KaiA (PDB ID: 1Q6A) [113] and domain I of the transcription factor TFIIIS (PDB ID: 1E00) [114], respectively.

3.4. Conclusions

We have shown that the single-trajectory-based tempering with a dihedral bias was useful in studying helical proteins in explicit solvent. We folded, within a few microseconds, four helical proteins, with the native conformation usually found in the largest cluster in simulation trajectories, as well as their mutants.

Our trajectories showed that a parallel helix bundle, especially one with a symmetric sequence, often has competing conformations that differ from the native one only by packing chirality and/or helix orientation. Similarly, the existence of competing conformations was previously reported for the Rop-dimer and its mutants [115-117]. While the ability to identify the native geometry is essential in studying helical proteins, the competing conformations can help to design new proteins, either as targets or as pitfalls to avoid [118].

Despite continuous improvement, the current force field might have yet reached perfection. As suggested by Best and Hummer [107], the current AMBER force field still underestimates both the enthalpy of hydrogen bonds (rendering helical conformations less energetically favorable) and the entropy of unfolded states. Our sampling strategy, which used a helical bias and a high temperature motion, could hopefully alleviate both problems.

3.5. Appendix

3.5.1. Dihedral-biased tempering

In this section, we describe a dihedral-biased tempering technique that combines the virtues of a tempering method introduced in Chapter 2 and a dihedral bias [40, 99, 100, 119]. The dihedral bias improves sampling helical conformations and accelerates the dynamics in the dihedral space. To preserve room temperature properties, the dihedral bias is added only on higher temperatures.

3.5.1.1. Tempering with a bias potential

On top of the tempering method, a bias potential $V(\mathbf{x})$, as a function of configuration \mathbf{x} , can be added to the generalized ensemble without disturbing room temperature properties. This is achieved via a temperature-dependent Hamiltonian

$$H(\beta, \mathbf{x}) = H_0(\mathbf{x}) + \left(\frac{\beta_0}{\beta} - 1 \right) V(\mathbf{x}), \quad (\text{S1})$$

where $H_0(\mathbf{x})$ is the unbiased potential energy. Thus the magnitude of $V(\mathbf{x})$ is full at the β_H , but zero at $\beta = \beta_0$. The distribution of the generalized ensemble becomes

$$\rho(\beta, \mathbf{x}) = w(\beta) \frac{\exp[-\beta H(\beta, \mathbf{x})]}{Z(\beta)} = w(\beta) \frac{\exp[-\beta H_0(\mathbf{x}) - (\beta_0 - \beta)V(\mathbf{x})]}{Z(\beta)}, \quad (\text{S2})$$

where $Z(\beta) = \int \exp[-\beta H(\beta, \mathbf{x})] d\mathbf{x}$ is the configuration space partition function. A regular tempering is recovered if $V(\mathbf{x}) = 0$.

No matter what the bias potential is, we have $H(\beta_0, \mathbf{x}) = H_0(\mathbf{x})$. The biased Hamiltonian also preserves a linear relation between $\beta H(\beta, \mathbf{x})$ and β , i.e.,

$$\beta H(\beta, \mathbf{x}) = \beta_0 V(\mathbf{x}) + [H_0(\mathbf{x}) - V(\mathbf{x})]\beta.$$

Thus room temperature properties can be readily recovered via the multiple histogram method [54-56]. The only modification is to substitute $H_0(\mathbf{x}) - V(\mathbf{x})$ for $H_0(\mathbf{x})$ in the method [also for E in Eq. (10)], for

$$\langle H_0(\mathbf{x}) - V(\mathbf{x}) \rangle_\beta = -\partial \log \rho(\beta, \mathbf{x}) / \partial \beta.$$

3.5.1.2. Dihedral bias

In our case, the bias potential $V(\mathbf{x})$ applies only to the two backbone dihedrals of amino acid residues in a protein.

For each residue i , the potential handles the two dihedrals φ_i (C-N-C α -C) and ψ_i (N-C α -C-N) separately by two functions $V_\varphi(\varphi_i)$ and $V_\psi(\psi_i)$. Thus

$$V(\mathbf{x}) = \sum_{a_i \neq G, P} V_\varphi[\varphi_i(\mathbf{x})] + V_\psi[\psi_i(\mathbf{x})],$$

where a_i denotes the one-letter amino acid name of residue i , $\varphi_i(\mathbf{x})$ and $\psi_i(\mathbf{x})$ are the two backbone dihedrals as functions of molecular coordinates \mathbf{x} . After excluding all glycine (G) and proline (P) residues, the two functions V_φ and V_ψ apply to all residues without the distinction of residue type or index.

The problem now is to find $V_\varphi(\varphi)$ and $V_\psi(\psi)$ that properly bias towards the helical conformation. Since the “helical conformation” is hard to define precisely (especially at a high temperature), we directly learn it from the force field.

First, we obtain the dihedral modes from decomposing the potentials of mean force (PMFs) along the two dihedrals. In this way, the modes are intrinsic to the force field and are usually smooth functions suitable for MD.

Second, we allow both $V_\varphi(\varphi)$ and $V_\psi(\psi)$ to be linear combinations of a few dihedral modes, each of which roughly corresponds to a basin in the dihedral space towards a typical secondary structure. The coefficients of combination are adjustable, e.g., a larger coefficient of the helical mode increases the bias towards the helical conformation.

The PMFs were obtained by a special simulation on a helical protein α_3D , PDB ID: 2A3D, also the first folding system [102], at $\beta_H = 0.2 \text{ mol}\cdot\text{k}^{-1}$ ($T_H \approx 600 \text{ K}$) for 50ns. The special simulation started from a fully-extended chain (hence it did not use the native structure), and was independent of folding simulations. We achieved flat distributions along both dihedrals by adaptively offsetting the projection of the force along each dihedral by its runtime-averaged value, or the mean force. After the simulation, the PMFs for φ and ψ were obtained by integrating the respective mean forces. In our implementation, the histogram along a dihedral was not completely flat due to a small missing force component from constraints; the corresponding correction was thus applied based on the histogram. The above approach allowed a comprehensive sampling of the entire dihedral space, covering

otherwise rarely-visited barrier regions. But since we only sampled extended conformations, the PMFs obtained were expected to deviate from the actual ones, which were dominated by the highly helical folded state. The deviations are, however, unimportant, as the PMFs served only as a rough guide.

We then decompose the PMF, using φ as example, to three modes as

$$V_{\varphi}^0(\varphi) \approx V_{\varphi}(\varphi) = - \sum_{k=A, B, C} M_k u_k(\varphi),$$

where $V_{\varphi}^0(\varphi)$ is the intrinsic PMF along φ ; $V_{\varphi}(\varphi)$ is its best approximation by a superposition of modes; M_k is the amplitude of mode k ; $u_k(\varphi)$ specifies mode k as a function of φ . Note that before the decomposition, we shift the PMF such that $V_{\varphi}^0(\varphi)$ is always negative, and all $u_k(x)$'s are positive definite.

Each $u_k(\varphi)$ is a bell-shaped function, asymmetric for $\varphi > \varphi_c$ and $\varphi < \varphi_c$ (φ_c being the center), and with up to 6th order moments on the exponent:

$$u_k(\varphi) = \exp[-a_2^{\pm}(\varphi - \varphi_c)^2 - a_4^{\pm}(\varphi - \varphi_c)^4 - a_6^{\pm}(\varphi - \varphi_c)^6],$$

where the superscripts '+' and '-' denote parameters for $\varphi > \varphi_c$ and $\varphi < \varphi_c$, respectively. The parameters a_2^{\pm} , a_4^{\pm} , a_6^{\pm} , φ_c of different modes are determined via a least square fitting in minimizing the difference between $V_{\varphi}^0(\varphi)$ and $V_{\varphi}(\varphi)$

$$(\delta V_{\varphi})^2 = \frac{1}{2\pi} \int_0^{2\pi} [V_{\varphi}^0(\varphi) - V_{\varphi}(\varphi)]^2 d\varphi.$$

The resulting parameters are listed in Table 3.4. As shown in Fig. 3.7, the decompositions authentically recovered the original PMFs: the average differences δV_φ and δV_ψ were $0.048 \text{ kJ mol}^{-1}$ and $0.030 \text{ kJ mol}^{-1}$ respectively, representing about 0.2% relative error compared with the magnitudes of intrinsic PMFs.

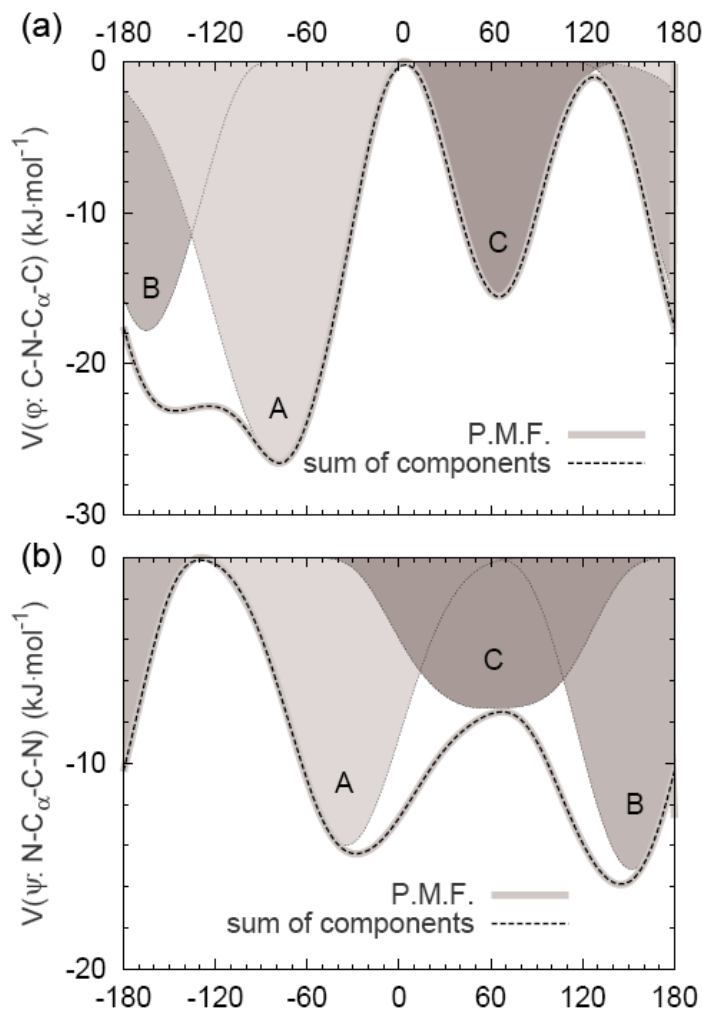


Figure 3.7. The potential of mean force and decomposed modes for (a) φ and (b) ψ . The maxima are shift to zero.

For the dihedral φ , the three decomposed modes roughly corresponded to α -helix, β -strand, and left-handed helix conformations. The first two modes, however, shared a large overlap in the dihedral space due to the broadening at the high

temperature $T_H \approx 600$ K. For the dihedral ψ , the first two modes corresponded to α -helix, β -strand conformations, with the last one lying in the transition region.

For convenience, we used the above PMFs and decomposed dihedral modes in simulations of all proteins, although ideally one could repeat the above procedure for every target protein.

Table 3.4. Parameters of the dihedral modes (A, B, and C) for φ and ψ .

	M (kJ mol ⁻¹)	φ_c or ψ_c (rad)	a_2^-	a_4^-	a_6^-	a_2^+	a_4^+	a_6^+
φ , A	53.1498	-1.35644	1.13993	0	0.35771	0.82287	0	0
φ , B	35.6254	-2.88178	1.62469	0	0.43748	1.90438	0.28168	0.23115
φ , C	31.1770	1.14492	2.38089	0.38803	0	2.07291	0	1.78939
ψ , A	28.0089	-0.60321	1.29464	0	0.02106	1.3024	0	0.08051
ψ , B	30.3457	2.65584	1.55338	0.13681	0.37975	1.47698	0	0.20224
ψ , C	14.6367	0.93443	0	0.25603	0.01605	0.45829	0.22928	0.06936

3.5.1.3. Adjusting dihedral modes

With the dihedral modes in hand, the bias potential, using $V_\varphi(\varphi)$ as an example, is constructed as a superposition of modes. In the first step, we construct a rough $\tilde{V}_\varphi(\varphi)$ via three parameters p_A , p_B and p_C , provided by the user, as

$$\tilde{V}_\varphi(\varphi) = \sum_{k=A,B,C} \min\{-k_B T \log p_k, M_k\} \times u_k(\varphi). \quad (\text{S3})$$

Eq. (S3) means that if the expected number of visits to mode k ($k = A, B, C$) is to be multiplied by p_k times, its magnitude in the bias potential is $\min\{-k_B T \log p_k, M_k\}$.

The min function annihilates the mode in case p_k is so small that $-k_B T \log p_k$ exceeds the intrinsic magnitude M_k .

To promote mode k , we can either increase p_k or reduce $p_{k'}$'s of other $k' \neq k$ modes. The latter produces a softer potential surface. $\tilde{V}_\varphi(\varphi)$ vanishes if all p_k 's are 1.0, and the method is reduced to a regular tempering. On the other hand, if all p_k 's are 0.0, $\tilde{V}_\varphi(\varphi)$ annihilates the intrinsic PMF $V_\varphi(\varphi)$ and recovers a flat distribution along either dihedral. A set of small p_k 's reduces magnitude of all modes and thus encourages transitions among them. The populations of modes in a production simulation would disagree with the p_k 's given by the user (even if the simulation were ran only at T_H) because the intrinsic PMFs were obtained from an extended state simulation, and that we ignored the correlations among residues.

The second (optional) step is to polish $\tilde{V}_\varphi(\varphi)$ to reduce the free energy barriers via the last parameter p_{\min} ($p_{\min} \geq 1.0$). We first construct an expected distribution $\rho_\varphi(\varphi) = \exp[-\beta V_\varphi^0(\varphi) - \beta \tilde{V}_\varphi(\varphi)]$, then trim it such that the expected distribution $\rho_\varphi^*(\varphi) = \max\{\rho_\varphi(\varphi), p_{\min} \min[\rho_\varphi(\varphi)]\}$. In this way, the highest free energy barrier is lowered by $|\log p_{\min}|/\beta$. The step does nothing if $p_{\min} = 1.0$.

Parameters p_A , p_B , p_C and p_{\min} of all trajectories are listed in Table 3.5.

Table 3.5. Trajectory parameters of α_3D , α_3W , Fap1-NR $_{\alpha}$ and S-836 and the mutants.

Prot.	ID	t^*	$\varphi: p_A, p_B, p_C, p_{\min}^{\dagger}$	$\psi: p_A, p_B, p_C, p_{\min}^{\ddagger}$	$r_s, r_v, r_c, \Delta x_{\text{PMF}}^{\#}$	RMSD $_{\min}/$ RMSD $_{\text{cls.}}^{\S}$
α_3D	0	1.7	1.0, 1.0, 1.0, 1.0	1.0, 1.0, 1.0, 1.0	7, 8, 10, 1.31	6.27/na
	1	1.0	1.0, 0.1, 0.3, 3.0	9.0, 0.4, 1.0, 3.0	7, 8, 10, 1.31	1.94/2.5 ₁
	2	1.3	1.0, 0.2, 0.3, 3.0	9.0, 0.4, 1.0, 3.0	7, 8, 10, 1.31	1.87/2.6 ₁
	3	1.2	1.0, 0.2, 0.5, 3.0	9.0, 0.5, 1.0, 3.0	7, 8, 10, 1.31	1.90/2.5 ₁
	4	1.3	0.15, 0.05, 0.1, 3.0	1.5, 0.5, 0.5, 3.0	7, 8, 10, 1.31	2.85/4.6 _{2, 99%}
	5	2.0	0.25, 0.05, 0.1, 1.0	3.0, 0.2, 0.2, 1.0	8, 9, 11, 1.42	1.97/2.7 ₁
	6	1.0	1.0, 0.3, 0.3, 1.0	1.0, 0.3, 0.3, 1.0	8, 9, 11, 1.42	2.12/2.7 ₁
α_3D_L	1	2.5	1.0, 0.3, 0.3, 1.0	1.0, 0.3, 0.3, 1.0	8, 9, 11, 1.31	na
	2	2.5	1.0, 0.5, 1.0, 1.0	1.0, 0.3, 0.5, 1.0	8, 9, 11, 1.31	na
	3	2.5	0.5, 0.1, 0.3, 1.0	2.0, 0.3, 0.5, 1.0	8, 9, 11, 1.31	na
α_3W	0	1.0	1.0, 1.0, 1.0, 1.0	1.0, 1.0, 1.0, 1.0	7, 8, 10, 1.33	7.18/na
	1	1.6	0.15, 0.05, 0.1, 1.0	1.5, 0.3, 0.3, 1.0	7, 8, 10, 1.33	1.47/2.2 ₁
	2	1.8	0.25, 0.05, 0.1, 1.0	2.0, 0.2, 0.2, 1.0	7, 8, 10, 1.33	1.39/1.7 ₁
	3	2.5	0.5, 0.1, 0.3, 1.0	5.0, 0.3, 0.5, 1.0	7, 8, 10, 1.33	1.38/2.2 ₁
	4	1.8	0.2, 0.05, 0.1, 1.0	2.0, 0.3, 0.3, 1.0	7, 8, 10, 1.33	1.40/2.4 ₁
	5	1.0	1.0, 0.1, 0.3, 3.0	9.0, 0.4, 1.0, 3.0	7, 8, 10, 1.33	1.83/3.6 _{2, 93%}
LQLQ	1	1.7	1.0, 0.3, 0.3, 1.0	1.0, 0.3, 0.3, 1.0	8, 9, 11, 1.33	na
	2	1.5	0.5, 0.1, 0.3, 1.0	5.0, 0.3, 0.5, 1.0	8, 9, 11, 1.33	na
Fap1-NR $_{\alpha}$	1	2.4	0.25, 0.05, 0.1, 1.0	3.0, 0.3, 0.3, 0.0	8, 9, 11, 1.46	1.00/1.4 _{2, 45%}
	2	2.5	0.2, 0.05, 0.1, 1.0	2.0, 0.25, 0.5, 1.0	8, 9, 11, 1.46	3.11/na
S-836	1	3.1	0.2, 0.05, 0.1, 1.0	2.0, 0.3, 0.3, 1.0	8, 10, 12, 1.45	2.09/3.8 ₁
	2	3.3	0.2, 0.05, 0.1, 1.0	2.0, 0.4, 0.0, 1.0	8, 10, 12, 1.45	2.21/3.8 ₁
	3	4.2	0.25, 0.05, 0.1, 1.0	2.5, 0.3, 0.1, 1.0	7, 8, 10, 1.25	2.30/4.3 ₁
	4	3.3	0.5, 0.1, 0.3, 1.0	5.0, 0.3, 0.5, 1.0	8, 9, 11, 1.43	2.13/2.5 ₁
	5	3.1	0.25, 0.05, 0.1, 1.0	3.0, 0.15, 0.3, 1.0	8, 9, 11, 1.43	7.31/na

The β range was (0.2, 0.42). The bin size $\delta\beta = 0.0001$, except for S-836 in which $\delta\beta = 0.00005$. The thermostat temperature $T_0 = 480\text{K}$. For the integral identity, $(\beta - \Delta\beta, \beta + \Delta\beta)$ with $\Delta\beta/\beta = 0.03$, except for S-836 in which $\Delta\beta/\beta = 0.02$. The time step Δt_{kT} for Eq. (10) was 2×10^{-5} (except for S-836, in which $\Delta t_{kT} = 10^{-5}$). For the adaptive averaging, $C_{\gamma} = 1.0$.

* The simulation time in μs .

\dagger, \ddagger The parameters of the dihedral modes.

$\#$ r_s and r_v : the switching and cutoff radii for vdW interactions; r_c and Δx_{PMF} : the real-space cutoff and Fourier grid spacing for PME.

\S The minimal and cluster-center backbone root mean square deviations (RMSDs) in \AA from the native structure; the latter was measured from the cluster containing the native conformation (RMSD $< 5 \text{\AA}$, na if no such cluster exists); the subscript was its rank in size, and if not 1, then followed by the population ratio to the largest cluster, e.g., 2.5₁ means the native cluster was the largest cluster and its RMSD was 2.5 \AA , 1.4_{2, 45%} means the native cluster was in the second largest, and its population ratio to the largest cluster was 45%. na: Not available.

3.5.2. Performance of the dihedral-biased tempering

3.5.2.1. Test case

We shall use the first protein α_3D [102] as a test case of the dihedral-biased tempering method. Starting from a fully-extended chain, we simulated the protein using three different methods: a room-temperature (300K) regular MD, a regular unbiased tempering, and a dihedral-biased tempering (this method). As a control, we also ran a regular 300K MD starting from the native structure.

For the dihedral-biased tempering, we ran multiple independent trajectories with different parameters for the bias potential (see Table 3.5).

3.5.2.2. Convergence of tempering

We first examine the convergence of the tempering part. We use trajectory 7 (Table 3.5) as an example. In Fig. 3.8(a) and 3.8(b), we show the time series for the instantaneous potential energy and temperature, both of which underwent many round-trips in their respective range.

The convergence can be checked from the histogram $H(\beta)$, which should be proportional to the intended temperature density $w(\beta)$. In Fig. 3.8(c), we show that the ratio $H(\beta)/w(\beta)$ indeed reached a constant.

We show in Fig. 3.8(d) 111 reconstructed potential energy histograms (from $\beta = 0.20$ to 0.42 with $\Delta\beta = 0.002$). A parallel tempering simulation would need

about 50 to 100 copies running in parallel to cover the same range with decent energy overlap, and the computational cost would be much higher.

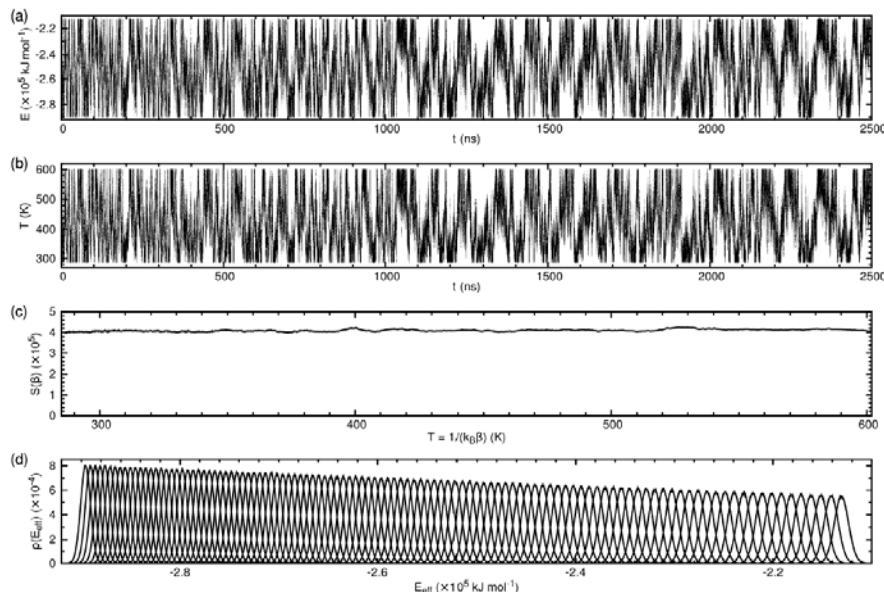


Figure 3.8. Folding trajectory 7 of $\alpha_3\text{D}$. (a) Instantaneous potential energy, (b) temperature versus time, (c) $H(\beta)/w(\beta)$, (d) energy histograms.

3.5.2.3. Folding progress (RMSD)

We monitored the progress of the backbone root-mean-square deviation (RMSD) from the experimental (NMR) structure.

As shown in Fig. 3.9(a), a typical RMSD was 3.2 \AA in the 300K native simulation. In the regular MD starting from a fully-extended conformation, a large spiral with $\text{RMSD} \approx 19 \text{ \AA}$, the RMSD lingered around $25 \sim 32 \text{ \AA}$.

In the unbiased tempering, the RMSD had a larger fluctuation from 6 \AA to 25 \AA , but a complete folding was not achieved in $1.7 \mu\text{s}$.

In trajectories using the dihedral biased tempering, the RMSD readily dropped below 3.2 \AA , indicating successful folding. Additionally, large-scale unfolding/refolding events occurred in both trajectories 2 and 7.

In sum, only the biased tempering method folded the protein quickly.

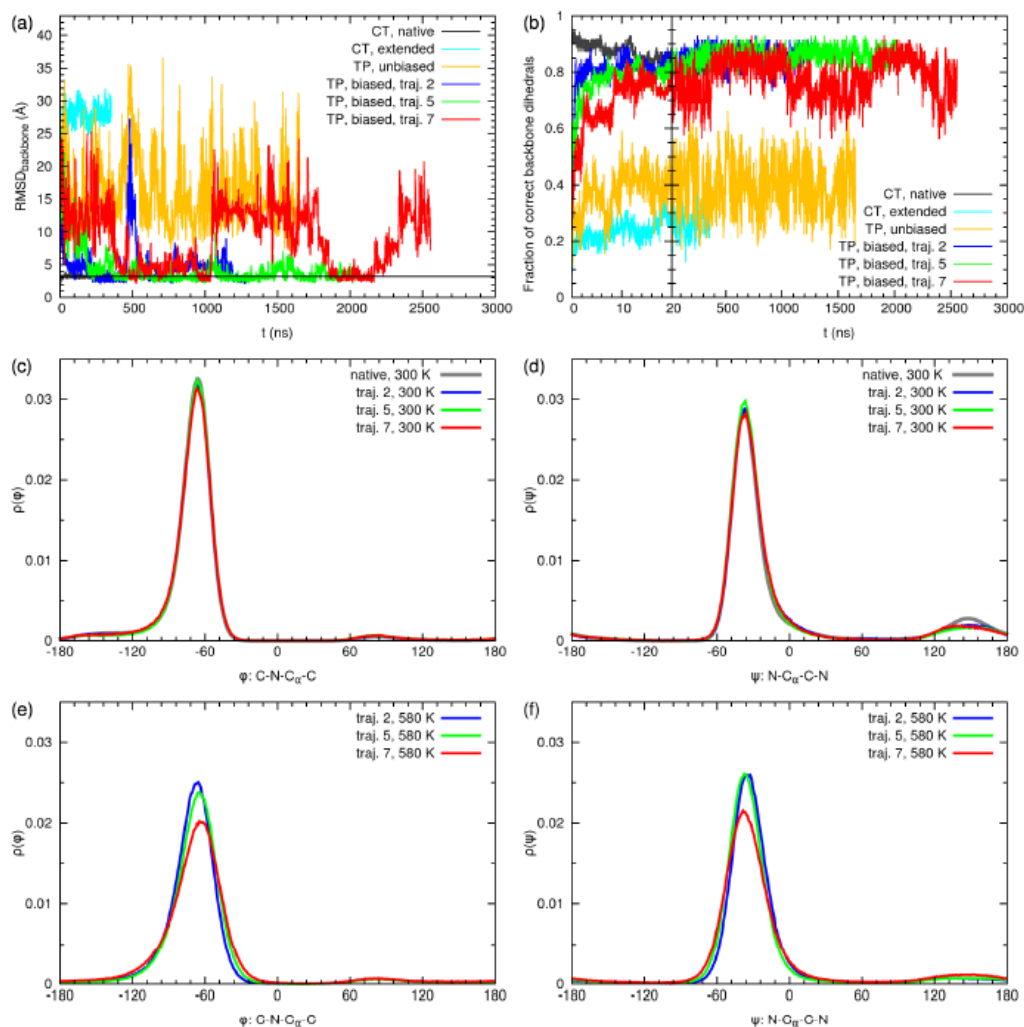


Figure 3.9. For α_3D : (a) backbone RMSD versus time for a regular constant-temperature molecular dynamics (CTMD) starting from a fully-extended chain, CTMD from the native, unbiased (TP) and dihedral-biased (this method, trajectories 2, 5 and 7) tempering from the extended chain; (b) the fraction of correct backbone dihedrals versus time; (c) and (d): residue-averaged backbone dihedral distributions of φ (C-N-C α -C) and ψ (N-C α -C-N) respectively (reweighted to 300K); (e) and (f): the corresponding distributions at 580K. We only included the folded state with RMSD $< 6 \text{ \AA}$ in (c)-(f) so that they represent only local dihedral equilibration, but not the true free energy landscape.

3.5.2.4. Folding progress (backbone dihedrals)

Similar to the previous case, we monitor the progress in the dihedral space by computing the fraction of correct backbone dihedrals (FCBD). We first define four backbone dihedrals conformations:

I: $\varphi < 0$ and $\psi \in [-100^\circ, 80^\circ)$

II: $\varphi < 0$ and $\psi \in [-180^\circ, -100^\circ) \cup [80^\circ, 180^\circ)$

III: $\varphi > 0$ and $\psi \in [-80^\circ, 100^\circ)$

IV: $\varphi > 0$ and $\psi \in [-180^\circ, -80^\circ) \cup [100^\circ, 180^\circ)$

For each residue, a dihedral conformation was considered correct if it fell into the category as the counterpart in the native structure. FCBD was then computed as the fraction of residues with the correct dihedral conformations (excluding the two terminal residues).

As shown in Fig. 3.9(b), the 300K native simulation yielded a FCBD about 80 to 90%, but not 100% possibly due to the difference at loop regions. The 300K regular MD from a fully-extended chain yielded a low FCBD about 15 to 35%. The regular (unbiased) tempering allowed a larger fluctuation that spanned from 20% to 60%, but failed to reach the native level.

In the dihedral biased tempering, a large FCBD was reached after the initial 1~10 ns, long before a complete folding occurred. Thus the bias helped the protein to quickly build up the helical content, while the folding process was still limited by the formation of correct tertiary structure.

3.5.2.5. Convergence in the dihedral space

We examined the convergence in the dihedral space, i.e., if trajectories with different dihedral bias potentials reached the same distributions at T_0 .

We computed the residue-averaged dihedral distributions at $T_0 = 300\text{K}$ and 580K , using the multiple histogram method [54-56]. Since the Hamiltonian was unbiased only at T_0 , the dihedral distributions with different biases should agree with each other at 300K , but not at 580K .

There was, however, a practical difficulty for a direct comparison. Although different trajectories shared the same native conformation, they sampled different nonnative ones, with each having slightly different dihedral distributions; and the convergence of sampling nonnative conformations was not achieved in our simulations. But here we only concern the equilibration in the dihedral space. To avoid this distraction, we only included frames in the folded states by imposing the condition $\text{RMSD} < 6\text{\AA}$, and filtered out nonnative conformations. We emphasize that the filtered distributions can only be used for this test, and they do not represent the actual free energy landscape.

As shown in Fig. 3.9(c)-(f), the dihedral distributions at 300K agreed, but those at 580K differed.

3.5.3. Geometric measures

We specify mathematical definition of 1) the chiral distance of helix-packing, 2) distance between two helices and 3) angle of two helices.

3.5.3.1. Representing rod of a helix

We needed to model a helix by a representative rod. We first compute the eigenvalues of the moments of inertia $\mathbf{I} = \{I_{\alpha\beta}\}$ from all alpha-carbon (C_α) atoms on the helix, where $I_{\alpha\beta} = \sum_i (r_{i\alpha} - r_{c\alpha})(r_{i\beta} - r_{c\beta})$ with $\alpha, \beta = x, y, z$; $\mathbf{r}_i = \{r_{ix}, r_{iy}, r_{iz}\}$ and $\mathbf{r}_c = \{r_{cx}, r_{cy}, r_{cz}\}$ are the coordinates of the i th C_α atom on the helix and the center of mass, respectively. Geometrically, the eigenvectors and eigenvalues of the matrix \mathbf{I} correspond to the directions and lengths of the principle axes of the representative ellipsoid. For the representative rod, we choose the eigenvector \mathbf{v}_1 ($|\mathbf{v}_1| = 1$) with the largest eigenvalue λ_1 as the direction, and construct the two ends \mathbf{b}_\pm by extending from the center of mass \mathbf{r}_c oppositely along the direction as $\mathbf{b}_\pm = \mathbf{r}_c \pm \sqrt{3\lambda_1} \mathbf{v}_1$. It is easy to see that if atoms are densely and uniformly distributed on a thin rod of length l along x , then $I_{xx} = l^2/12$, and all other $I_{\alpha\beta}$'s are zeros. Since $\lambda_1 = l/(2\sqrt{3})$, $\mathbf{r}_c \pm (l/2)\mathbf{v}_1$ recovers the ends of the rod as expected.

3.5.3.2. Chiral distance for packing helices

We now define a chiral distance D for three helices A, B and C. If helices A and B are parallel, D equals the signed distance from helix C to the plane extended by A and B. The definition is generalized below for nonparallel A and B. First, the middle helix B is modeled as a rod, with \mathbf{b}_0 and \mathbf{b}_1 being the two ends (connected to A and C, respectively). We then compute, for any two points \mathbf{a} and \mathbf{c}

$$D(\mathbf{a}, \mathbf{b}_0, \mathbf{b}_1, \mathbf{c}) = \frac{(\mathbf{b}_0 - \mathbf{a}) \times (\mathbf{b}_1 - \mathbf{b}_0)}{\|(\mathbf{b}_0 - \mathbf{a}) \times (\mathbf{b}_1 - \mathbf{b}_0)\|} \cdot (\mathbf{c} - \mathbf{b}_1). \quad (\text{S4})$$

Finally, we let \mathbf{a} run through all C_α atoms on helix A and \mathbf{c} through those on helix C, and compute the average as,

$$D(A, B, C) = \langle D(\mathbf{a}, \mathbf{b}_0, \mathbf{b}_1, \mathbf{c}) \rangle_{\substack{\mathbf{a} \text{ on helix A} \\ \mathbf{c} \text{ on helix C}}}.$$

$D(A, B, C)$ is positive if viewed along helix B from \mathbf{b}_0 to \mathbf{b}_1 , helix A can be rotated clockwise to the position of helix C by an angle less than 180° , negative otherwise.

3.5.3.3. Helix distance

We compute the distance between two helices A and B as follows. First, for a C_α atom \mathbf{a} on helix A, we compute the minimal distance d_a to any C_α atom on helix B. Similarly d_b is computed for a C_α atom \mathbf{b} on helix B. The average of all d_a 's and d_b 's is defined as the distance between helices A and B.

3.5.3.4. Helix angle

For two helices A and B, their angle is computed from the angle of the two corresponding representative rods.

3.5.3.5. Hydrophobic contact number

We compute the number of contacting hydrophobic residues as the number of pairs of C_α atoms on different helices within 12\AA .

3.5.4. Clustering method

3.5.4.1. The target function

Given a trajectory, the clustering method aims at forming a set of clusters of similar structures, or a *cluster configuration*. The cluster configuration should not depend on the order. We satisfy the condition by setting the cluster configuration to the one that minimizes some target function H . Secondly, H should allow each frame i to carry the weight w_i from the multiple histogram method [54-56] to filter out the high-temperature influence.

We used this target function

$$H = \frac{1}{2} \left(\sum_c w_c \bar{d}_c \right) + \frac{1}{2} N_c \mu W ,$$

where the sum is performed over all clusters c 's, $w_c = \sum_{i \in c} w_i$ is the total weight of all frames in cluster c , $\bar{d}_c = \sum_{i,j \in c} d_{ij} w_i w_j / (\sum_{i \in c} w_i)^2$ is the average distance among any two frames in cluster c (the distance d_{ij} was computed as the backbone RMSD of two protein conformations i and j after a mutual structural alignment); N_c is the number of clusters; μ is the energy cost of forming a new cluster, or the “chemical potential,” and W is the total weight of all frames in the trajectory.

3.5.4.2. Minimization of the target function

We used a global minimizer to minimize the target function [29]. It requires a statistical ensemble of clustering configurations, which we define as

$$Z = \sum (\prod_c n_c!) \exp(-\beta H),$$

where β is the inverse temperature used only for the clustering, independent of the one for sampling, n_c is the number of frames in cluster c . The factor $n_c!$ encourages clusters to change sizes as it varies drastically with the cluster size n_c .

The number of resulting clusters depends on μ . A larger μ increases the cost of forming a new cluster and thus leads to fewer clusters. We used $\mu = 0.7 \text{ \AA}$, which usually yielded a single cluster for a native simulation but a handful of clusters for a folding one.

The method is expensive, since it operates on a full RMSD matrix of all frame pairs. In practice, we skipped frames at a regular interval, and limit the total number of frames within 2000.

3.5.5. Initial structures

The initial structures for folding trajectories were all prepared as follows. For each protein, the initial structure was a large extended spiral that fits into the simulation box. Water molecules are added subsequently. A mild (usually less than 1000 steps) energy minimization was performed to remove strong frictions between the protein and its surrounding water molecules. A short 2 to 10 picoseconds MD simulation was then performed on the energy-minimized structure at 300K to raise the energy to a normal level. The resulting structure was then used as the starting point for all folding trajectories of the same protein. For the four existing proteins, we show in Fig. 3.10 the initial structures after the procedure.

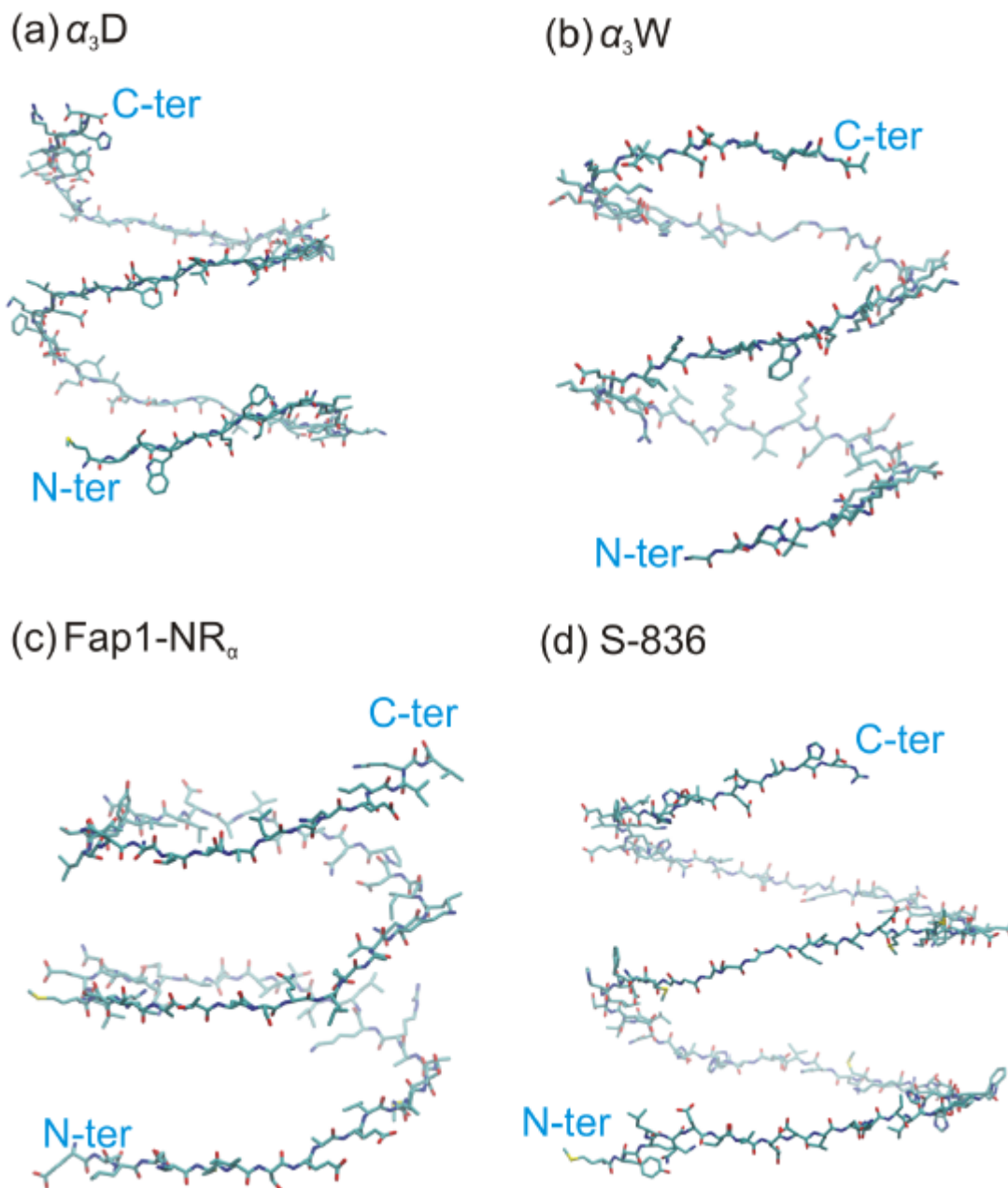


Figure 3.10. Initial extended conformations of (a) α_3D , (b) α_3W , (c) Fap1-NR $_{\alpha}$, (d) S-836. Water molecules are removed for clarity.

3.5.6. Representative structures at the room temperature

We illustrate typical structures found in two folding trajectories: trajectory 7 for α_3D and trajectory 2 for α_3D_L . In Fig. 3.11, we plotted the RMSD as a function of time with representative structures shown at roughly a 300~500 ns interval. The

representative structures must carry a weight $w > 0.5$ after reweighted to 300K to ensure that they were relevant there. It can be seen that, even in the nonnative conformations, there were still a fraction of residue helical content, c.f. panel (b) of Fig. 3.9. This was in agreement with a recent MD simulation on Anton [47]. Nevertheless, non-helical structures such as coils and β -strands were also common.

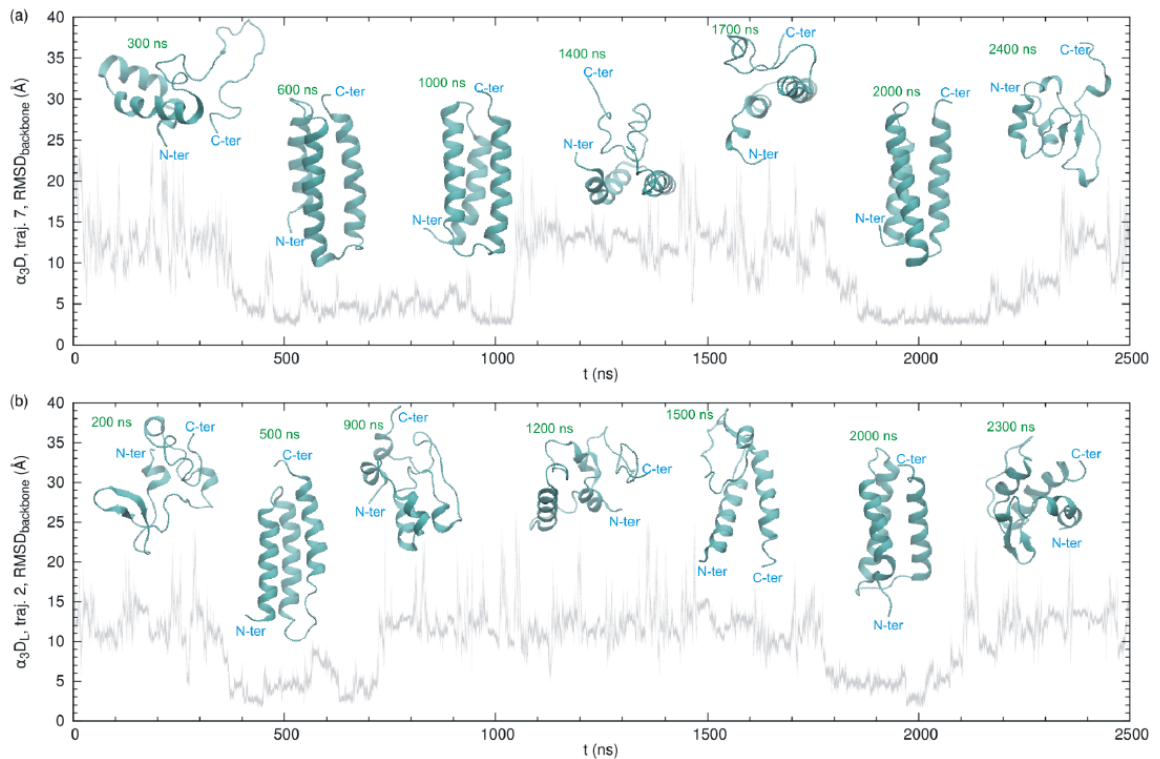


Figure 3.11. Representative structures (reweighted to 300K) along (a) trajectory 7 of α_3D and (b) trajectory 2 of the mutant α_3D_L .

Chapter 4

Improving statistical distribution

4.1. Introduction

The objective of this chapter is to present a method for estimating a general statistical distribution from data collected in a molecular simulation. The contents are largely identical to those in reference [120].

The method brings improvement upon the common approach of using a normalized histogram, which suffers from either a large noise when the bin size is too small or a systematic bias when the bin size is too large.

Our identity is akin to a previous one derived by Adib and Jarzynski [121], hence the AJ identity below, whereby the distribution density $\rho(x)$ at a point x is estimated from a weighted number of visits to a window surrounding x , plus a correction from integrating the derivative $\rho'(x)$. The AJ identity improves over the

histogram-based approach not only by eliminating the systematic bias from binning but also by smoothing out the resulting distribution, as the window contains much more data points than a single bin. But the identity is slightly inconvenient as it neither ensures a nonnegative output, nor determines its optimal parameters.

Here we present a new identity in which we construct a proper correction factor from integrating the “mean force,” which is the logarithmic derivative of the distribution density, and use it to *divide* the number of visits to a local window to get an unbiased estimate, as schematically shown in Fig. 4.1. It ensures a nonnegative distribution, and offers a simple estimate of the optimal window size.

4.2. Methods

4.2.1. Integral identity

We wish to find an expression for the distribution density $\rho(x)$ at $x = x^*$. We first approximate $\rho(x^*)$ by a histogram sum over a local window (x_-, x_+) enclosing $x = x^*$, and then apply a correction factor. Formally, we have

$$\rho(x^*) = \frac{\int_{x_-}^{x_+} \rho(x) dx}{\int_{x_-}^{x_+} \rho(x) / \rho(x^*) dx},$$

where the numerator $\int_{x_-}^{x_+} \rho(x) dx$ counts the fraction of x falling into the window (x_-, x_+) , and can thus be measured from the histogram sum over the window.

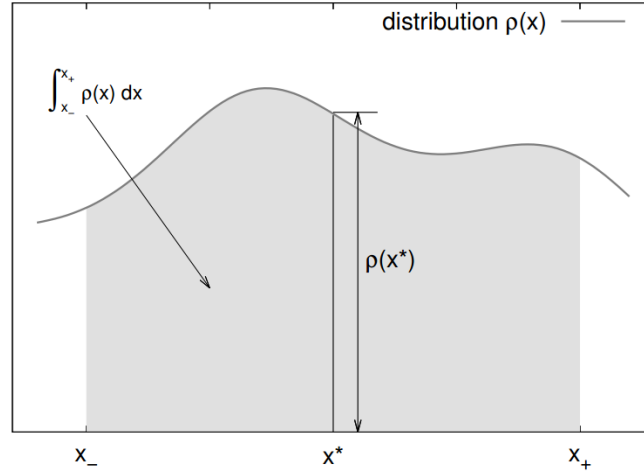


Figure 4.1. The fractional identity express the ratio of a histogram sum $\int_{x_-}^{x_+} \rho(x) dx$ (shaded) to the distribution density $\rho(x^*)$ as an integral of $(\log \rho)'(x)$.

We then take the logarithm of $\rho(x)/\rho(x^*)$, and write it as an integral of $(\log \rho)'(y)$ as

$$\rho(x)/\rho(x^*) = \exp[\log \rho(x) - \log \rho(x^*)] = \exp\left(\int_{x^*}^x (\log \rho)'(y) dy\right).$$

So

$$\rho(x^*) = \frac{\int_{x_-}^{x_+} \rho(x) dx}{\int_{x_-}^{x_+} \exp\left(\int_{x^*}^x (\log \rho)'(y) dy\right) dx}. \quad (36)$$

We refer to Eq. (36) as the *fractional identity*. Unlike in the AJ identity [121], the correction here is applied as a divisor instead of additively. Nevertheless, it can be derived as a near-optimal modification of the AJ identity, as shown in 4.5.1.

4.2.2. Mean force

The identity Eq. (36) requires a mean force $(\log \rho)'(x)$ in addition to a histogram. We now construct a conjugate force $f_x = f_x(\mathbf{r}^N, \mathbf{s})$, as a function of molecular coordinates \mathbf{r}^N and auxiliary ensemble variables \mathbf{s} , such that the ensemble average is the needed $(\log \rho)'(x)$. The expressions for f_x can be found in Eq. (40) and Eq. (39) or (39').

We first express x as a function $x = X(\mathbf{r}^N, \mathbf{s})$ of molecular coordinates \mathbf{r}^N and, optionally, of variables \mathbf{s} of the simulation ensemble, e.g., \mathbf{s} can be the volume in an isothermal-isobaric ensemble, or the temperature in a tempering simulation [20-25]. Note that $X(\mathbf{r}^N, \mathbf{s})$ denotes a *function* of \mathbf{r}^N and \mathbf{s} , while x its *value*.

The distribution density $\rho(x)$ is defined as

$$\rho(x) = \int \delta(X(\mathbf{r}^N, \mathbf{s}) - x) w(\mathbf{r}^N, \mathbf{s}) d\mathbf{r}^N d\mathbf{s}, \quad (37)$$

where $\delta(\dots)$ is the δ -function, and $w(\mathbf{r}^N, \mathbf{s})$ is the weight for coordinates \mathbf{r}^N and parameters \mathbf{s} , e.g., $w(\mathbf{r}^N, \mathbf{s}) \propto e^{-\beta U(\mathbf{r}^N)}$ in a canonical ensemble, with $U(\mathbf{r}^N)$ being the potential energy and β the inverse temperature. Eq. (37) is properly normalized, as

$$\int \rho(x) dx = \int \left(\int \delta(X(\mathbf{r}^N, \mathbf{s}) - x) dx \right) w(\mathbf{r}^N, \mathbf{s}) d\mathbf{r}^N d\mathbf{s} = \int w(\mathbf{r}^N, \mathbf{s}) d\mathbf{r}^N d\mathbf{s} = 1.$$

Similarly, the average $\langle A(\mathbf{r}^N, \mathbf{s}) \rangle_x$ at x for any quantity $A(\mathbf{r}^N, \mathbf{s})$ can be defined as

$$\langle A(\mathbf{r}^N, \mathbf{s}) \rangle_x = \frac{\int A(\mathbf{r}^N, \mathbf{s}) \delta(X(\mathbf{r}^N, \mathbf{s}) - x) w(\mathbf{r}^N, \mathbf{s}) d\mathbf{r}^N d\mathbf{s}}{\int \delta(X(\mathbf{r}^N, \mathbf{s}) - x) w(\mathbf{r}^N, \mathbf{s}) d\mathbf{r}^N d\mathbf{s}}, \quad (38)$$

where we have again used the δ -function to collect configurations with $X(\mathbf{r}^N, \mathbf{s})$ being x , and the denominator is equal to $\rho(x)$. Our objective is to find an quantity

$f_x(\mathbf{r}^N, \mathbf{s})$ such that $\langle f_x(\mathbf{r}^N, \mathbf{s}) \rangle_x = (\log \rho)'(x) = \rho'(x)/\rho(x)$.

We now evaluate the derivative of $\rho(x)$ as

$$\rho'(x) = \int -\frac{\partial}{\partial X} \delta(X(\mathbf{r}^N, \mathbf{s}) - x) w(\mathbf{r}^N, \mathbf{s}) d\mathbf{r}^N ds,$$

where we have used $\partial \delta(X - x)/\partial x = -\partial \delta(X - x)/\partial X$.

We proceed by introducing a vector field $\mathbf{v}(\mathbf{r}^N, \mathbf{s})$ such that $\mathbf{v} \cdot \nabla X = 1$, e.g.

$$\mathbf{v}(\mathbf{r}^N, \mathbf{s}) = \frac{\nabla X(\mathbf{r}^N, \mathbf{s})}{\nabla X(\mathbf{r}^N, \mathbf{s}) \cdot \nabla X(\mathbf{r}^N, \mathbf{s})}. \quad (39)$$

Generally, it can be constructed from an arbitrary vector field \mathbf{Y} ($\nabla X \cdot \mathbf{Y} \neq 0$) as

$$\mathbf{v}(\mathbf{r}^N, \mathbf{s}) = \frac{\mathbf{Y}(\mathbf{r}^N, \mathbf{s})}{\nabla X(\mathbf{r}^N, \mathbf{s}) \cdot \mathbf{Y}(\mathbf{r}^N, \mathbf{s})}. \quad (39')$$

Note that ∇ is defined for both \mathbf{r}^N and \mathbf{s} , so $\nabla = (\partial/\partial \mathbf{r}^N, \partial/\partial \mathbf{s})$.

We now insert $1 = \mathbf{v} \cdot \nabla X$ into the integrand and recall that $\delta(X(\mathbf{r}^N, \mathbf{s}) - x)$ depends on \mathbf{r}^N and \mathbf{s} only through X . So $\nabla X (\partial \delta(X - x)/\partial X) \rightarrow \nabla \delta(X - x)$, and

$$\begin{aligned} \rho'(x) &= \int -\mathbf{v}(\mathbf{r}^N, \mathbf{s}) \cdot \nabla \delta(X(\mathbf{r}^N, \mathbf{s}) - x) w(\mathbf{r}^N, \mathbf{s}) d\mathbf{r}^N ds \\ &= \int \delta(X(\mathbf{r}^N, \mathbf{s}) - x) \nabla \cdot [\mathbf{v}(\mathbf{r}^N, \mathbf{s}) w(\mathbf{r}^N, \mathbf{s})] d\mathbf{r}^N ds \\ &= \int \delta(X(\mathbf{r}^N, \mathbf{s}) - x) w(\mathbf{r}^N, \mathbf{s}) f_x(\mathbf{r}^N, \mathbf{s}) d\mathbf{r}^N ds, \end{aligned}$$

where we have integrated by parts to shift the ∇ to the rest of the integrand, and defined a conjugate force $f_x \equiv \nabla \cdot \mathbf{v} + \mathbf{v} \cdot \nabla \log w$. The last step follows from

$$\nabla \cdot (\mathbf{v} w) = \nabla \cdot \mathbf{v} w + \mathbf{v} \cdot \nabla w = (\nabla \cdot \mathbf{v} + \mathbf{v} \cdot \nabla \log w) w = f_x w.$$

Comparing to Eq. (38), we see that the mean force $(\log \rho)'(x) = \rho'(x)/\rho(x)$ is equal to the average of $f_x(\mathbf{r}^N, \mathbf{s})$ under a fixed x ,

$$(\log \rho)'(x) = \left\langle f_x(\mathbf{r}^N, \mathbf{s}) \right\rangle_x = \left\langle \nabla \cdot \mathbf{v}(\mathbf{r}^N, \mathbf{s}) + \mathbf{v}(\mathbf{r}^N, \mathbf{s}) \cdot \nabla \log w(\mathbf{r}^N, \mathbf{s}) \right\rangle_x. \quad (40)$$

For a canonical ensemble, the second term $\mathbf{v} \cdot \nabla \log w$ becomes $-\beta \mathbf{v} \cdot \nabla U$, i.e., the projection of the molecular force $-\nabla U = \mathbf{F}$ to the gradient of X , assuming Eq. (39). So the name mean force of $\langle f_x \rangle$ is justified. This special case was identical to the result derived by Ciccotti, Kapral, and Vanden-Eijnden [122].

Another special case of Eq. (40) is the dynamic temperature by Rugh [12]. Consider the canonical ensemble at infinite temperature $\beta \rightarrow 0$. The distribution of the total energy $E = H(\mathbf{r}^N)$ (\mathbf{r}^N now represents phase-space point) is proportional to the density of states $\Omega(E)$. The mean force $d \log \Omega(E)/dE$ should be the intrinsic temperature $\beta(E)$. By Eq. (40), it equals $\langle \nabla \cdot \mathbf{v} \rangle_E$, with $\mathbf{v} = \nabla H / (\nabla H \cdot \nabla H)$, we thus recover Rugh's dynamic temperature.

4.2.3. Optimal window size

We now determine the two window boundaries x_- and x_+ in Eq. (36) such that they minimize the statistical error in $\rho(x^*)$.

First, the histogram and mean-force data contribute independently to the numerator and denominator, respectively. The amount of contribution is however controlled by the window size. The output $\rho(x^*)$ is dominated by the histogram contribution (numerator) with a narrow window, but by the mean-force contribution (denominator) with a wide one. In the former case, the denominator is reduced to the window width, and thus the identity to a histogram average. At the other extreme, if the window covers the entire domain of x , the numerator becomes a constant, and the distribution is determined entirely by the mean-force integral on the denominator, i.e., $\rho(x^*) = \exp\left[\int^{x^*} (\log \rho)'(x) dx\right]$.

As the window size increases, the error of the numerator decreases as more data points reduces uncertainty, but that of the denominator increases as the error in the mean-force integral accumulates. The sum reaches a minimum at the optimal window size.

Quantitatively, the relative error of the numerator $\varepsilon(N)/N$ is $1/\sqrt{N}$, where $N = N(x_-, x_+)$ is the number of independent data points included in the window.

The relative error of the denominator D is harder to compute exactly and thus is estimated from an upper bound. First, since D is an integral of $\exp(\Delta \log \rho)$, the *relative* error of D is no larger than the *absolute* error of $\Delta \log \rho$. Next, since $\Delta \log \rho$ itself is an integral: $\Delta \log \rho(x) = \int_{x^*}^x \langle f_x \rangle(x') dx'$, the maximum occurs most likely at $x = x_{\pm}$. In the discrete version, the integral becomes a sum over bins as

$\Delta \log \rho = \sum_i \langle f_x \rangle(x_i) \delta x$ with δx being the bin size. Its error $[\varepsilon(\Delta \log \rho)]^2$, assuming no correlation among mean force at different bins, is $\sum_i \sigma_f^2(x_i) \delta x^2 / \delta n(x_i)$, where $\sigma_f^2(x_i)$ is the variance of the conjugate force at x_i , and $\delta n(x_i)$ is the number of independent data points in the bin at x_i .

On reaching the optimal window, including one more bin from either edge would keep the combined error $(\varepsilon(N)/N)^2 + (\varepsilon(D)/D)^2$ constant. So

$$-\frac{\delta n(x_{\pm})}{N(x_-, x_+)^2} + \frac{\sigma_f^2(x_{\pm})}{\delta n(x_{\pm})} \delta x^2 = 0,$$

where the first term is the decrease of error due to the increased sample size, while the second is the increase due to the mean-force integration. Thus

$$\frac{\delta n(x_{\pm})}{N(x_-, x_+)} = \sigma_f(x_{\pm}) \delta x.$$

For a relatively narrow window, we have $N \approx \delta n w / \delta x$, with w being the window width. If we further replacing $\sigma_f(x_{\pm})$ by a local mean $\bar{\sigma}_f$, then

$$w = \gamma / \bar{\sigma}_f, \tag{41}$$

where γ is a heuristic factor around 1.0. As we overestimate the error of the denominator, Eq. (41) somehow underestimates the optimal window size. In practice, we found the optimal γ was between 1.0 and 2.0.

On using Eq. (41), we emphasize that σ_f is the mean-force fluctuation at a fixed x , i.e., $\sigma_f^2(x) = \langle f^2 \rangle_x - \langle f \rangle_x^2$, and thus is evaluated at the bin at x . However, after

the intra-bin calculation, we can then average $\sigma_f(x)$ over a local or global window to improve the precision of $\bar{\sigma}_f$.

If the mean-force fluctuation is very small, Eq. (41) suggests abandoning the histogram data and switching to a mean-force integration. On the other hand, if the mean-force has a very large variance, one should stick to the histogram. Thus, the method is effective only if the mean-force fluctuation is small.

4.2.4. Summary and practical notes

To summarize the method, we first compute a mean force profile $(\log \rho)'(x)$ at any x from Eqs. (39) [or (39')] and (40), then plug it into Eq. (36). The combined formula looking like

$$\rho(x^*) = \frac{\int_{x_-}^{x_+} \rho(x) dx}{\int_{x_-}^{x_+} \exp \left[\int_{x^*}^x \left\langle \nabla \cdot \left(\frac{\nabla X}{\nabla X \cdot \nabla X} \right) + \frac{\nabla X \cdot \nabla \log w}{\nabla X \cdot \nabla X} \right\rangle_y dy \right] dx}, \quad (42)$$

and the window (x_-, x_+) size is determined by Eq. (41).

Practically, we assume both histogram and mean force data are collected by bins of size δx . To evaluate $\int_{x_-}^{x_+} \exp \left(\int_{x^*}^x (\log \rho)'(y) dy \right) dx$ in Eq. (36), we first compute

$\varphi(x, x^*) = \int_{x^*}^x (\log \rho)'(y) dy$, then $\int_{x_-}^{x_+} \exp[\varphi(x, x^*)] dx$. The step size for numerical

integration is always δx . For the inner integral, $(\log \rho)'$ is computed as the bin-

averaged value, and at every bin boundary x , $\varphi(x, x^*) \approx \sum_{x_i=x}^x (\log \rho)'(x_i) \delta x$. The outer integral is then evaluated by the trapezoidal rule as

$$\int_{x_-}^{x_+} f(x) dx \approx \left[\frac{f(x_-)}{2} + f(x_- + \delta x) + \dots + f(x_+ - \delta x) + \frac{f(x_+)}{2} \right] \delta x,$$

where $f(x) = \exp[\varphi(x, x^*)]$.

The statistical error of $(\log \rho)'(y)$ depends on the bin size; but that of the integral $\varphi(x, x^*)$, or $\rho(x^*)$, does not. To see this, we consider a small bin δx with δn data points. If the standard deviation of $(\log \rho)'(y)$ is σ , then the error of the bin is $\sigma^2/\delta n$. Its contribution to the error of $\varphi(x, x^*)$ should be multiplied by δx^2 and is thus $\sigma^2 \delta x^2/\delta n$. If we split the bin into two, then each sub-bin has roughly $\delta n/2$ points, each with an error of $2\sigma^2/\delta n$. But the contribution to the error of $\varphi(x, x^*)$ from the two new bins, $(2\sigma^2/\delta n)(\delta x/2)^2 \times 2 = \sigma^2 \delta x^2/\delta n$, remains the same.

Eq. (40) can fail if a bin is empty. In this case, we symmetrically enlarge the bin to a window such that it contains at least one data point, then use Eq. (40).

4.2.5. Extension to weighted histogram analysis method

We now extend Eq. (36) to a composite distribution, i.e., a superposition of several distributions under different conditions, which can result from an extended ensemble simulation, such as a tempering simulation [20-25]. For concreteness, we assume that the individual distributions are canonical ones $\rho(x, \beta_i)$ at different temperatures β_i (with i being its label).

The aim is to estimate the distribution $\rho(x, \beta)$ at β , which needs not to be one of the β_i 's. We will derive a mean-force-improved version of the weighted histogram analysis method (WHAM) [54-56, 123].

We first generalize Eq. (36) to

$$\rho(x^*, \beta) = \frac{\sum_i N_i \int_{x_-}^{x_+} \rho(x, \beta_i) dx}{\sum_i N_i \int_{x_-}^{x_+} \frac{\rho(x, \beta_i)}{\rho(x^*, \beta)} dx},$$

where N_i is the total number of independent data points from the simulation at the temperature β_i , and the sum is carried over different temperatures β_i . To proceed, we simultaneously multiple and divide $\rho(x^*, \beta_i)$ in the denominator,

$$\sum_i N_i \int_{x_-}^{x_+} \frac{\rho(x, \beta_i)}{\rho(x^*, \beta)} dx = \sum_i N_i \frac{\rho(x^*, \beta_i)}{\rho(x^*, \beta)} \int_{x_-}^{x_+} \frac{\rho(x, \beta_i)}{\rho(x^*, \beta_i)} dx,$$

where the x -independent $\rho(x^*, \beta_i)/\rho(x^*, \beta)$ has been moved out of the integral. We then convert $\rho(x, \beta_i)/\rho(x^*, \beta_i)$ to the mean force integral at a fixed β_i as before,

$$\rho(x^*, \beta) = \frac{\sum_i N_i \int_{x_-}^{x_+} \rho(x, \beta_i) dx}{\sum_i \left(N_i \frac{\rho(x^*, \beta_i)}{\rho(x^*, \beta)} \int_{x_-}^{x_+} \exp\left[\int_{x^*}^x (\log \rho)'(y, \beta_i) dy\right] dx \right)}. \quad (43)$$

For example, in the canonical ensemble, $w(U, \beta) = \exp(-\beta U)/Z(\beta)$ with $Z(\beta)$ being the partition function. So the potential energy U distribution

$$\rho(U^*, \beta) = \frac{\sum_i N_i \int_{U_-}^{U_+} \rho(U, \beta_i) dU}{\sum_i \left(N_i \frac{\exp[-\beta_i U^*]/Z(\beta_i)}{\exp[-\beta U^*]/Z(\beta)} \int_{U_-}^{U_+} \exp \left[\int_{U^*}^U (\langle \nabla \cdot \mathbf{v} \rangle_{U'} - \beta_i) dU' \right] dU \right)}, \quad (44)$$

where $\mathbf{v} = \nabla U / (\nabla U \cdot \nabla U)$. The regular WHAM [54-56, 123] is recovered with an infinitesimal window $U_- = U_+ = U^*$. Generally, Eq. (43) improves the histogram method by using the mean force data, e.g., the dynamic temperature $\langle \nabla \cdot \mathbf{v} \rangle_{U'}$ here. Since $\langle \nabla \cdot \mathbf{v} \rangle_{U'}$ is the same under any temperature β_i , the data from multiple temperatures can be combined.

4.3. Examples

4.3.1. Potential energy distribution

We first compute a potential energy distribution $\rho(U)$ in the canonical ensemble, in which $w(\mathbf{r}^N, \beta) = \exp[-\beta U(\mathbf{r}^N)]/Z(\beta)$ with β being the reciprocal temperature, and $Z(\beta)$ being the partition function. Eqs. (36) and (40) become

$$\rho(U^*) = \frac{\int_{U_-}^{U_+} \rho(U) dU}{\int_{U_-}^{U_+} \exp \left(\int_{U^*}^U (\log \rho)'(y) dy \right) dU},$$

$$(\log \rho)'(U) = \langle \nabla \cdot \mathbf{v} - \beta \rangle_U = \left\langle \nabla \cdot \left(\frac{\nabla U(\mathbf{r}^N)}{\nabla U(\mathbf{r}^N) \cdot \nabla U(\mathbf{r}^N)} \right) \right\rangle_U - \beta.$$

Since $(\log \rho)'(U)$ is the difference between the dynamic temperature [12, 13, 124-127] $\langle \nabla \cdot \mathbf{v} \rangle$ and the simulation temperature β , the distribution peaks at $(\log \rho)'(U) = 0$ where the two cancel.

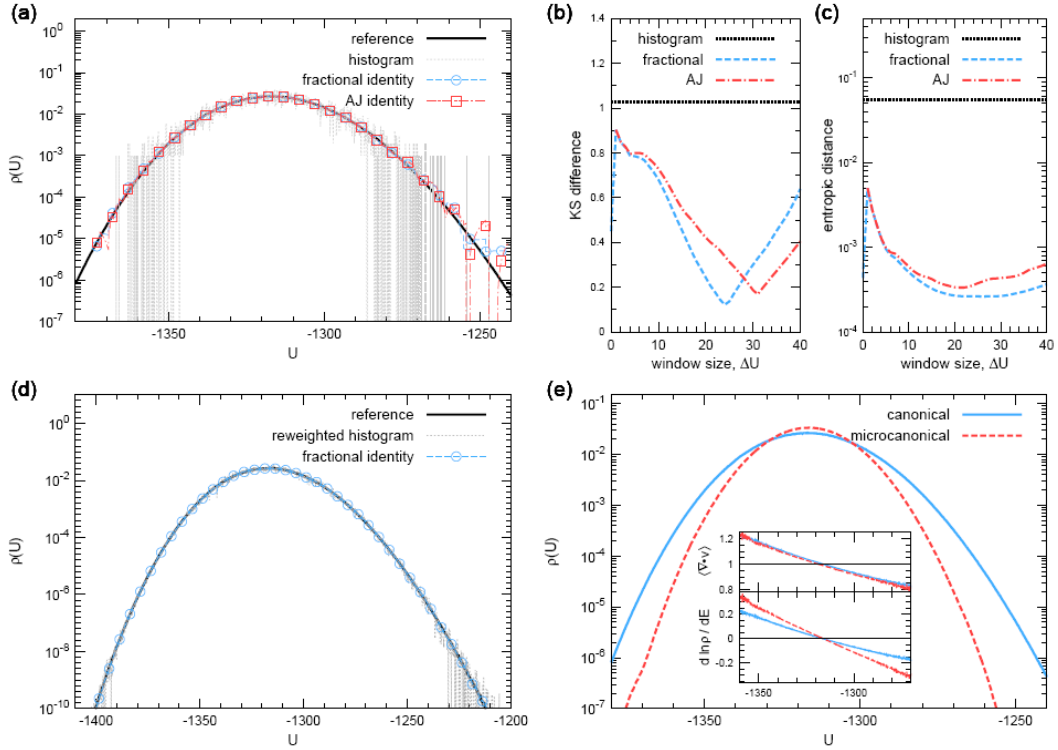


Figure 4.2. Potential energy distribution. (a) Histogram, fractional identity, and Adib-Jarzynski-like (AJ) identity. The same test sample were used for all methods. Symbol spacing $\Delta U = 5.0$. (b) and (c) Errors measured from the KS difference and entropic distance, respectively, as functions of window size ΔU . (d) The distributions from the original and improved weighted histogram method. (e) Canonical versus microcanonical ensembles.

We performed a molecular dynamics (MD) simulation on a 256-particle Lennard-Jones system under a smoothly switched potential (see 4.5.3, $r_s = 2.0$ and $r_c = 3.0$). The temperature $\beta = 1.0$, density $\rho = 0.8$, time step $\Delta t = 0.002$. Velocity rescaling was used as the thermostat [15] with a time step 0.01.

From a single trajectory of 10^7 steps, we constructed two samples. In the test sample, 10^4 frames (every 1000 steps) were collected; in the reference one, all frames were used. The setting avoided possible sampling inaccuracy to affect the comparison of different methods, as explained in 4.5.4. The bin size for histogram-like was always $\delta U = 0.1$. Unless specified otherwise, the test sample was used.

We first demonstrate the use of the fractional identity Eq. (36) with a fixed symmetric window of size $\Delta U = U_+ - U_- = 12.4$, a value determined from Eq. (41) ($\gamma = 1.0$). The mean force $(\log \rho)'(U)$ was computed from a single bin at U . As shown in Fig. 4.2(a), the resulting distribution was smoother than the histogram. For comparison, we used the AJ identity with the same window size. Though the results were generally similar, the AJ identity sometimes yielded negative values at the two ends, while the fractional identity appeared to be more robust and closer to the reference.

To show the gain from the integral identity approach, we define a KS difference as $\Delta_{\text{KS}} = (\sqrt{N} + 0.11 + 0.12/\sqrt{N})\Delta_{\text{CDF}}$, which is commonly used in the Kolmogorov-Smirnov (KS) test for detecting the difference between two distributions [128], where N is the sample size, and Δ_{CDF} is the maximal difference between the cumulative distribution function (CDF) $F(x) = \int_{-\infty}^x \rho(y) dy$ of the resulting distribution and that from the reference. The smaller the quantity is, the more accurate the test distribution is. As the measure is independent of the bin size, it mainly detects the systematic bias in the test distribution instead of the smoothness of distribution density. As the identity is not optimized for the CDF but for the distribution density, the KS difference serves as a stringent test.

The KS differences, computed for the histogram, the fractional identity Eq. (36) and the AJ identity Eq. (A1) are shown in Fig. 4.2(b). It is clear that that both identities rendered more accurate distributions than the histogram. We also show there was an optimal window size that minimized the error. However, for the

fractional identity, the optimal window size $\Delta U \approx 20.0$ was greater than the value 12.4 given by Eq. (41). Thus, a factor $\gamma \approx 1.5$ was used in other examples. Recall the KS difference scales with \sqrt{N} , thus from Fig. 4.2(b) we estimated about 20-fold increase of efficiency from using the optimal window. We also notice that with a smaller window, the fractional identity gave better estimates than the AJ identity. This was expected as that the fractional identity is the optimal modification of the AJ identity in this case, as shown in 4.5.1. With a larger window, the errors from both identities grew rapidly due to the larger involvement of the mean force data. As the fractional identity quickly switched to a pure mean-force-based integral with a large window, its growth was faster. The comparison shows that choosing the window size is crucial to the success of the integral identity, and an overly large window can be counterproductive.

We performed a similar comparison in terms of the entropic distance defined as $D(\rho \parallel \rho^{\text{ref.}}) = \int_{-\infty}^{\infty} \log[\rho(y)/\rho^{\text{ref.}}(y)]\rho(y)dy$ for two distributions $\rho(x)$ and $\rho^{\text{ref.}}(x)$. For the AJ identity, in case $\rho(x) < 0$, zero was assumed. Unlike the KS difference, this quantity directly compares the distribution densities. As shown in Fig. 4.2(c), the fractional identity consistently produced a smaller entropic distance than the AJ identity, suggesting an improved smoothness. Interestingly, the error of the entropic distance also had a minimal, which occurred at a similar location $\Delta U \approx 20.0$ to that from the KS difference.

We now demonstrate the mean-force-improved weighted histogram analysis method (WHAM) introduced in 4.2.5. In this case, we performed additional

simulations at two neighboring temperatures $T = 0.8$ and $T = 1.2$. The reweighted distributions to $T = 1.0$ from both the original WHAM and the improved version are shown in Fig. 4.2(d), and as expected, the latter was smoother.

We emphasize that the identity approach is ensemble-dependent because the mean force depends on the ensemble weight w . To show this, we simulated the same system by a regular MD, which targeted a microcanonical ensemble in which the total energy was kept as a constant. In the ensemble, the configuration weight, after averaging out momenta, is $w(\mathbf{r}^N) \propto \sqrt{K}^{N_f-2} = \sqrt{E_{\text{tot}} - U(\mathbf{r}^N)}^{N_f-2}$, where N_f is the number of degrees of freedom, and K , U and E_{tot} are the kinetic, potential and total energy, respectively. The mean force is $(\log \rho)'(U) = \langle \nabla \cdot \mathbf{v} \rangle_U - \frac{\frac{1}{2}N_f - 1}{E_{\text{tot}} - U}$, where $N_f = 3N - 6$, and the constant reference temperature β in the canonical ensemble is changed to an energy-dependent term $(\frac{1}{2}N_f - 1)/(E_{\text{tot}} - U)$.

The microcanonical simulation was similar to the canonical one. During equilibration, the kinetic energy was scaled regularly to match $\bar{T} \approx 1.0$, and was kept as a constant afterwards ($E_{\text{tot}} = -932$). As shown in Fig. 4.2(d), the distributions and mean forces (lower inset) from the two ensembles differed considerably, whereas the dynamic temperature $\langle \nabla \cdot \mathbf{v} \rangle$ (upper inset) matched. This example shows the importance of applying the correct formula for the mean force.

4.3.2. Volume distribution

In the second example, we compute a volume distribution $\rho(V)$ in an isothermal-isobaric ensemble [10, 129]. Unlike the previous case, the volume V is not a function of system coordinates, but an additional variable in the ensemble weight $w(\mathbf{r}^N, V)$. Particularly, the volume V serves as a scaling factor that translates the reduced (0 to 1) coordinates \mathbf{R}_i to the actual ones as $\mathbf{r}_i = \sqrt[3]{V}\mathbf{R}_i$. In terms of reduced coordinates, the ensemble weight can be written as

$$w(\{\mathbf{r}_i\}, V) d\mathbf{r}^N dV \propto \exp[-\beta U(\{\sqrt[3]{V}\mathbf{R}_i\}) - \beta p V] V^N d\mathbf{R}^N dV,$$

where β and p are the reciprocal temperature and the pressure, respectively.

According to Eq. (40), the conjugate force f_V is reduced to $\partial \log w / \partial V$ in this case (the vector field \mathbf{v} is the unit vector along the direction of the parameter V , so $\nabla \cdot \mathbf{v} = 0$, $\mathbf{v} \cdot \nabla = \partial / \partial V$). Thus,

$$\rho(V^*) = \frac{\int_{V_-}^{V_+} \rho(V) dV}{\int_{V_-}^{V_+} \exp\left(\int_{V^*}^V (\log \rho)'(y) dy\right) dV},$$

$$(\log \rho)'(V) = \frac{N}{V} - \frac{\langle \beta \mathbf{r} \cdot \nabla U \rangle_V}{3V} - \beta p = \beta \left[\langle p_c(\mathbf{r}^N) \rangle_V - p \right]$$

The latter represents the difference between the internal pressure

$p_c(\mathbf{r}^N) \equiv (N + \beta \langle \mathbf{r} \cdot \mathbf{F} \rangle_V / 3) / V$ and the ensemble parameter p .

For a open system, there is a subtle distinction between the apparent volume distribution $\rho(V)$ defined above and the actual physical one $\hat{\rho}(V)$. The difference

arises from the fact that the partition function $Z(\beta, V)$ in the canonical ensemble counts configurations with the volume *no larger than*, instead of equal to, the volume V of the simulation box. In other words, unless there are particles lying precisely at all six boundary faces of the simulation box, it is always possible to shrink the box slightly without leaving out any particles. Thus, the physical volume of a configuration is usually less than the volume of the box. Koper and Reiss [129] then introduced a *differential* partition function Z' [129] for all configurations with the volume precisely falling in $(V - dV, V)$ as $Z' \propto (\partial Z / \partial V) dV = \langle p_c \rangle_V Z dV$, and accordingly the actual physical volume distribution $\hat{\rho}(V)$ differs from $\rho(V)$ by a factor, i.e., $\hat{\rho}(V) \propto \langle p_c \rangle_V \rho(V)$.

The above correction does not apply to a periodic system. Nonetheless, we still calculated $\hat{\rho}(V)$ below only to show the process by pretending the system were non-periodic.

We performed an MD simulation on the 256 Lennard-Jones system using the switched potential (with $r_s = 2.5$ and $r_c = 3.5$) around the critical point: $T = 1.24$ and $p = 0.115$. Velocity rescaling was used as the thermostat [15] with a time step 0.01. For the pressure control, Monte Carlo volume moves were tried every two MD steps with a maximal magnitude of $\pm 2.0\%$ of the side length of the box. The trajectory contained 10^7 frames, and the time step $dt = 0.002$.

From the trajectory, we constructed two samples. In the test sample, one out of every 100 frames was used. In the reference one, all frames were used. The

setting avoided possible sampling inaccuracy to affect the comparison of different methods, as explained in 4.5.4. In both case, histogram-like data were collected using a bin width $\delta V = 1.0$. Unless specified otherwise, we used the test sample.

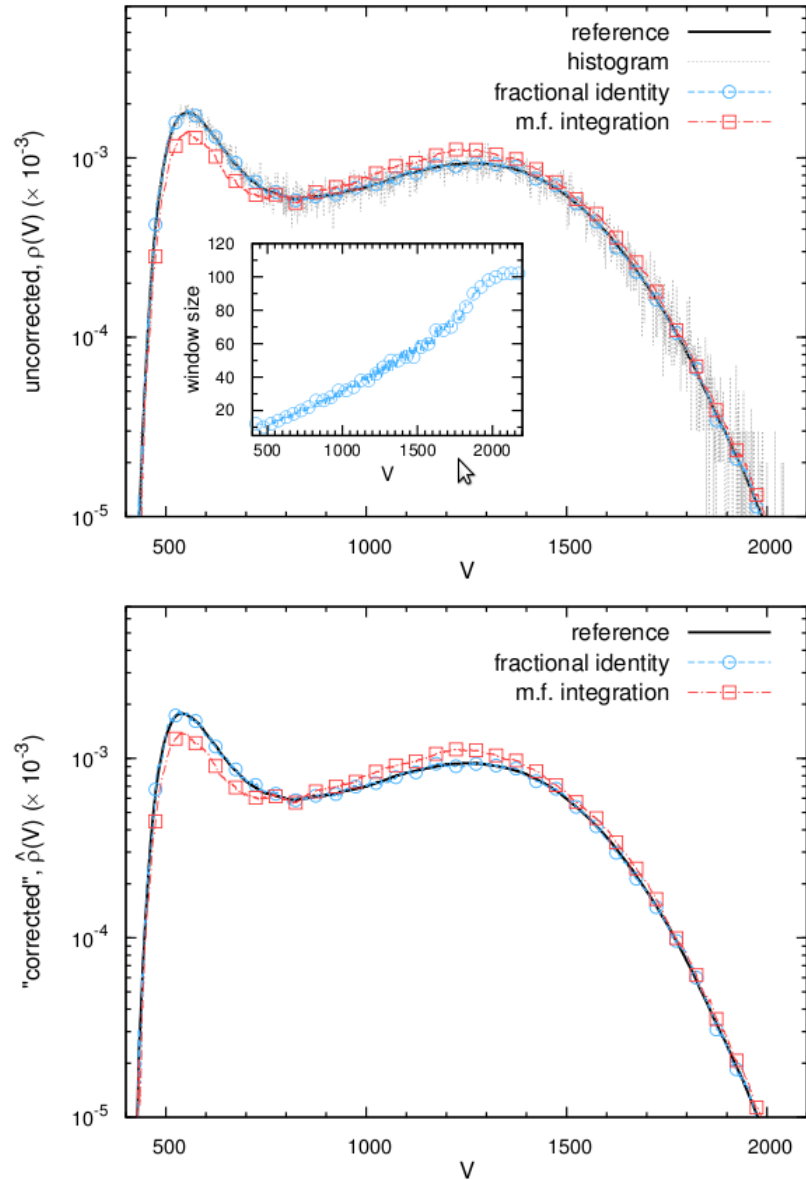


Figure 4.3. Volume distributions. (a) $\rho(V)$ and (b) $\hat{\rho}(V)$ (adjusted) at $p = 0.115$ and $T = 1.24$. Inset of (a): the window size. Symbol spacing $\Delta V = 50.0$.

Due to the wide volume range and that the mean force fluctuation $\sigma_f \propto 1/V$, we used a variable window size, and applied Eq. (41) with σ_f estimated from a local window, and $\gamma = 1.5$ (heuristic value).

To apply the correction, we further computed $\langle p_c \rangle_V$ from a second integral identity, Eqs. (A4) and (A5), in 4.5.2. The window size of the second identity was similarly determined from the local σ_f but with $\gamma = 3.0$.

As shown in Fig. 4.3, the volume distribution $\hat{\rho}(V)$ from the fractional identity was smoother than the histogram but still had some roughness. From the inset, we observe that the window size grew linearly with the volume V .

This example also clearly illustrates the danger of using an overly large window. We show in Fig. 4.3 the distribution from a pure mean-force integration $\rho(V) = \exp\left[\int^V (\log \rho)'(V') dV'\right]$, which is the limiting case of using an infinite window, showed a much larger deviation from the reference. But the deviation was not systematic and diminished with the sample size: when calculated from the larger reference sample, it was hardly noticeable, see Fig. 4.3(b). The example again illustrates the importance of proper window size.

4.3.3. Radial distribution function

In the third example, we compute a radial distribution function $g(r)$. Given a test particle is at the origin, $g(r)$ gives the relative probability density of finding

another particle at a distance r away, such that $g(r) = 1$ in a non-interacting system.

It relates to the radial distribution density $\rho(r)$ as

$$\rho(r) = 4\pi r^2 g(r) / V \quad (45)$$

with V being the volume of the simulation box, and $4\pi r^2 dr / V$ gives the probability of finding a different particle in a spherical shell of a radius r and thickness dr

around the test particle, if the particles were non-interacting. $\rho(r)$ is normalized as

$$\int_0^{\sqrt{3}L/2} \rho(r) dr = 1, \text{ where } L = \sqrt[3]{V} \text{ is the box size and } \sqrt{3}L/2 \text{ is maximal distance}$$

between two particle under the periodic boundary condition [10] [of course with

$r > L/2$, $\rho(r)$ becomes unphysical]. We modify Eq. (36) to

$$g(r^*) = \frac{\int_{r_-}^{r_+} \rho(r) dr}{\int_{r_-}^{r_+} 4\pi r^2 / V \exp\left[\int_{r^*}^r (\log g)'(y) dy\right] dr}.$$

To derive the mean force in the canonical ensemble, in which

$w(\mathbf{r}) \propto \exp[-\beta U(\mathbf{r}^N)]$, with β being the inverse temperature, we apply Eq. (40)

with a vector field $\mathbf{v}_i = \frac{1}{2} \hat{\mathbf{r}}_{12} (\delta_{1i} - \delta_{2i})$, where i is the particle index. Since

$$\nabla \cdot \mathbf{v} = 2/r_{12} \text{ with } r_{12} = |\mathbf{r}_{12}|, \text{ we have } (\log \rho)'(r) = \langle \nabla \cdot \mathbf{v} + \beta \mathbf{v} \cdot \mathbf{F} \rangle_r = 2/r + \frac{1}{2} \beta \langle \hat{\mathbf{r}}_{12} \cdot \mathbf{F}_{12} \rangle_r,$$

where $\hat{\mathbf{r}}_{12} = \mathbf{r}_{12} / r_{12}$ is the unit displacement vector from particles 2 to 1, $\mathbf{F}_{12} = \mathbf{F}_1 - \mathbf{F}_2$

is the difference between the forces exerted on particles 1 and 2, and the average is

evaluated at $r_{12} = r$. By Eq. (45),

$$(\log g)'(r) = (\log \rho)'(r) - 2/r = \frac{1}{2} \beta \langle \hat{\mathbf{r}}_{12} \cdot \mathbf{F}_{12} \rangle_r.$$

We simulated the 256 Lennard-Jones system with the density $\rho = 0.7$ under $T_1 = 0.85$ and $T_2 = 0.4$, using the switched potential ($r_s = 2.5$ and $r_c = 3.5$). Velocity rescaling with time step 0.01 was used as the thermostat [15].

After 10^6 steps of equilibration, we simulated another 10^7 steps with a time step $dt = 0.002$. We then constructed two samples from this trajectory; for the test sample, we picked 5 frames (from every 2×10^6 steps), and for the reference one, 5000 frames (every 2000 steps). The setting avoided possible sampling inaccuracy to affect the comparison of different methods, as explained in 4.5.4. Unless specified otherwise, we used the test sample. Each frame still contributes $256 \times 255 / 2 = 32640$ pairs of particles; but only half ($\pi/6 \approx 0.5$) of them satisfy $r < L/2$. The bin size $\delta r = 0.002$ was used in collecting histogram-like data.

Since this example was also used in the original paper from Adib and Jarzynski [121], it is instructive to compare the two identities. We include the AJ identity, Eq. (20) in reference [121], here for convenience

$$g(r^*) = \frac{e^{-\beta u(r^*)}}{V_{\Omega^*}/V} \left[\int_{R_1}^{R_{\max}} \rho(r) e^{\beta u(r)} dr + \beta \int_0^{R_{\max}} \rho(r) \phi(r, r^*) F_r(r) dr \right], \quad (46a)$$

$$\phi(r, r^*) = \frac{e^{\beta u(r)}}{3r^2} \left[(r^3 - R_1^3) \theta(r - R_1) + (R_1^3 - R_{\max}^3) \theta(r - r^*) \right], \quad (46b)$$

where r is the distance from the test particle, $u(r)$ is the pair potential (see 4.5.3),

$V_{\Omega^*} = (4\pi/3)(R_{\max}^3 - R_1^3)$, R_1 is a distance close to the repulsion core (we used $R_1 = 1.0$

here), R_{\max} is half of the simulation box size, $\theta(x)$ is the step function: 1 if $x > 0$, 0

otherwise, $F_r(r) = \langle \hat{\mathbf{r}} \cdot \mathbf{F}(\mathbf{r}) \rangle_{|\mathbf{r}|=r} + u'(r)$ is the radial mean force of a particle at a distance r away from the test particle, excluding the force from the test particle.

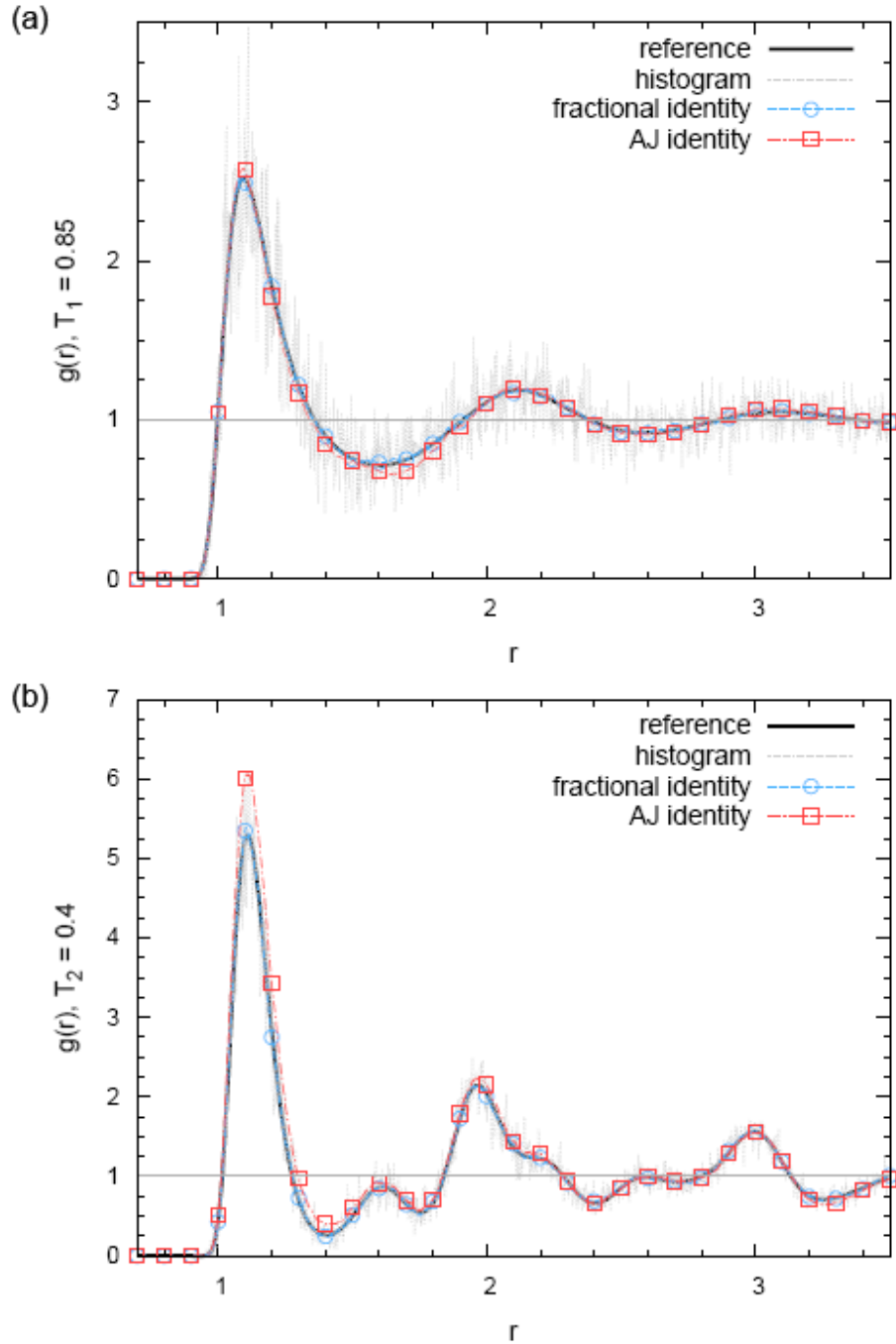


Figure 4.4. Radial distribution functions $g(r)$. (a) $T_1 = 0.85$; (b) $T_2 = 0.4$. Histogram, fractional identity, and original Adib-Jarzynski (AJ) identity. Symbol spacing $\Delta r = 0.1$.

As shown in Fig. 4.4, the fractional identity produced smooth distributions with good agreement with the respective references in both temperatures, despite a relatively small sample size. On the other hand, although the AJ identity also produced smooth distributions, there was an appreciable deviation at the lower temperature $T_2 = 0.4$, especially around the principle peak $r \approx 1.1$. The deviation was not systematic, as it was negligible when the calculation was performed on the reference sample, see Fig. 4.4(c) and (d). The large deviations from the AJ identity were similar to those observed in the previous example of the volume distribution when the mean force integration was used to produce the distribution. Thus, they were likely due to an overly large window, as the entire range of r , from 0 to R_{\max} , was used as the window by the AJ identity Eq. (46a). The error was larger at a lower temperature because the mean force changed more drastically there, hence larger mean force fluctuation. By contrast, in the fractional identity case, smaller windows, $\Delta r = 0.14$ for $T_1 = 0.85$ and $\Delta r = 0.09$ for $T_2 = 0.4$ were used according to Eq. (41) ($\gamma = 1.5$), and thus the output was more robust. We also note that the optimal window size shrunk at the lower temperature. The trend is universal, since f_x has a component $\beta \mathbf{v} \cdot \mathbf{F}$ in the canonical ensemble, as one increases β (or lowers the temperature), the fluctuation grows, and thus the window size shrinks. The example again illustrates the critical influence from the window size.

4.4. Conclusions and discussions

In conclusion, we presented an identity, Eqs. (36) and (40), for estimating a statistical distribution from data collected in molecular simulations. The new identity has broad applications (e.g., to any variable x and any ensemble) and at the same time offers a robust and precise output.

We also showed that the window size should be carefully chosen to maximize the benefit from the identity. An overly large window risks a large error from the mean-force integration, although it often yields a smoother result.

Finally, we distinguish the method from an explicit smoothing method [130, 131] in that this method does not assume a smooth distribution. Although the use of the mean force $(\log \rho)'$ implies a differentiable $\rho(x)$, the mean force itself can be as oscillatory as an apparent noise. However, it may be possible to improve the method by introducing elements of the explicit smoothing techniques with certain approximations.

4.5. Appendix

4.5.1. Alternative derivation of the fractional identity

We first rephrase the work of Adib and Jarzynski on the radial distribution function [121] in our context, i.e., with respect to a general distribution.

First, any $\rho(x)$ at $x = x^*$ can be evaluated as an integral over (x_-, x^*) as

$$\rho(x^*) = \rho(x^*) \phi(x^*) - \rho(x_-) \phi(x_-) = \int_{x_-}^{x^*} [\rho(x) \phi'(x) + \rho'(x) \phi(x)] dx,$$

where $\phi(x)$ is an arbitrary function under two conditions, $\phi(x_-) = 0$ and $\phi(x^*) = 1$; we have also converted the difference of $\rho(x)\phi(x)$ to an integral within the range.

The domain of integration can be enlarged to a window (x_-, x_+) that encloses x^* by applying the above equation to two windows (x_-, x^*) and (x^*, x_+) ($x_- < x^* < x_+$) with different $\phi(x)$'s, and then linearly combining them, see Fig. 4.5,

$$\rho(x^*) = \int_{x_-}^{x_+} \rho(x) \phi'(x) dx + \int_{x_-}^{x_+} \rho'(x) \phi(x) dx, \quad (\text{A1})$$

where the combined $\phi(x)$ satisfies

$$\begin{cases} \phi(x_+) = \phi(x_-) = 0, \\ \phi(x^{*-}) - \phi(x^{*+}) = 1, \end{cases} \quad (\text{A2})$$

with $\phi(x^{*-})$ and $\phi(x^{*+})$, the values of $\phi(x)$ immediately at the left and right of x^* respectively, serving as coefficients of combining the two windows. The function $\phi(x)$ is equivalent to the vector field $\mathbf{u}(\mathbf{r})$ in the original paper [121].

But Eq. (A1) does not always yield a positive output since the correction

$$\int_{x_-}^{x_+} \rho'(x) \phi(x) dx \text{ can accidentally overthrow the histogram } \int_{x_-}^{x_+} \rho(x) \phi'(x) dx.$$

We now derive the fractional identity Eq. (36) from Eq. (A1). We start from a simple observation: for any continuous function $f(x)$ satisfying $f(x^*) = 1$, Eq. (A1) applies not only to $\rho(x)$ itself, but also to the product $\rho(x)f(x)$, i.e.,

$$\rho(x^*) = \int_{x_-}^{x_+} [\rho(x)f(x)] \phi'(x) dx + \int_{x_-}^{x_+} [\rho(x)f(x)]' \phi(x) dx.$$

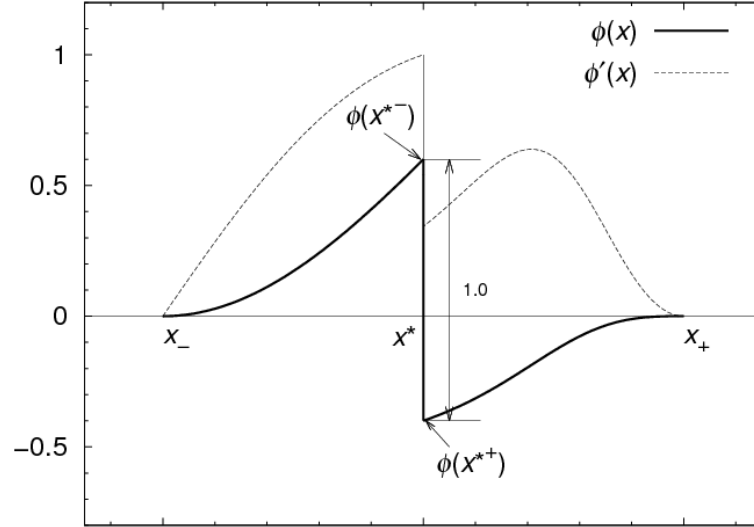


Figure 4.5. The auxiliary function $\phi(x)$ and its derivative $\phi'(x)$.

An arbitrary $f(x)$, or equivalently a reference distribution [121, 132], does not guarantee a non-negative output. But if we choose $f(x)$ such that $\rho(x)f(x)$ is a constant, the second term on the right hand side of the above equation vanishes, and

$$\rho(x^*) = \int_{x_-}^{x_+} [\rho(x)f(x)] \phi'(x) dx. \quad (\text{A3})$$

Thus $\rho(x^*)$ is nonnegative as long as $\phi'(x)$ is so. The function $f(x)$ is obtained by integrating the distribution mean force from the boundary $f(x^*) = 1$ as

$$f(x) = \exp\left\{-[\log \rho(x) - \log \rho(x^*)]\right\} = \exp\left(-\int_{x^*}^x (\log \rho)'(y) dy\right).$$

It is easily verified that $\frac{d}{dx} \log f(x) = -\frac{d}{dx} \log \rho(x)$ and hence $\frac{d}{dx} [\rho(x)f(x)] = 0$.

Finally, we determine $\phi(x)$ based on the observation that $\phi'(x)$ acts as a weight in Eq. (A3). Thus, to minimize statistical error, $\phi'(x)$ should be inversely proportional to the variance of $\rho(x)f(x)$ [10]. For a small window, we assume that the error of $\rho(x)f(x)$ comes mainly from the number of visits $\rho(x)$ instead of $f(x)$. Additionally, we assume the variance of $\rho(x)$ is proportional to $\rho(x)$, i.e., a Poisson distribution [10], so $\text{Var}[\rho(x)f(x)] = \text{Var}[\rho(x)] f^2(x) \propto \rho(x) f^2(x) \propto f(x)$.

$\phi'(x)$ can now be written as $C/f(x)$, where C is determined from Eqs. (A2) as

$$1 = \phi(x^{*-}) - \phi(x_-) + \phi(x_+) - \phi(x^{*+}) = \int_{x_-}^{x_+} \phi'(x) dx \text{ with the singularity at } x = x^* \text{ ignored.}$$

Solving the equation gives $C = 1 / \int_{x_-}^{x_+} \exp\left(\int_x^{x_+} (\log \rho)'(y) dy\right) dx$, hence Eq. (36).

4.5.2. Mean force improvement

We derive an improved formula for $(\log \rho)'(x)$. If $(\log \rho)''(x)$ is available, one can apply an Adib-Jarzynski-like identity (see 4.5.1) as:

$$(\log \rho)'(x_0) = \int_{x_-}^{x_+} [\varphi'(y) (\log \rho)'(y) + \varphi(y) (\log \rho)''(y)] dy, \quad (\text{A4})$$

where $\varphi(x)$ satisfies $\varphi(x_-) = \varphi(x_+) = 0$, $\varphi(x_0 - \delta) - \varphi(x_0 + \delta) = 1$. For simplicity, we particularly use a linear function $\varphi(x) = (x - x_b)/(x_+ - x_-)$, with $x_b = x_-$ if $x < x_0$ or $x_b = x_+$ otherwise. Note that the window (x_-, x_+) can be different from that in Eq. (36). An averaging expression for computing $(\log \rho)''(x)$ can be found by taking the derivative of Eq. (40)

$$(\log \rho)''(x) = \langle (\Delta f_x)^2 \rangle_x + \langle \mathbf{v}_x \cdot \nabla f_x \rangle_x, \quad (\text{A5})$$

where \mathbf{v}_x denotes the vector field given by Eq. (39) or (39') for the quantity x .

Eqs. (A4) and (A5) are particularly useful in computing the volume distribution, in which a smooth multiplicative correction term $\beta \langle p_c(V) \rangle_V$ can be obtained from the mean force $(\log \rho)'(V) = \beta (\langle p_c(V) \rangle_V - p)$ using the above method.

We list the formulas of $\mathbf{v}_x \cdot \nabla f_x$ for the first three examples in 4.3.

For the potential energy distribution in the canonical ensemble,

$f_U = \nabla \cdot \mathbf{v} - \beta$, and

$$\mathbf{v}_U \cdot \nabla f_U = -\frac{\mathbf{F} \cdot \nabla \nabla^2 U}{(\mathbf{F} \cdot \mathbf{F})^2} - \frac{\nabla^2 U M + \mathbf{h} \cdot \mathbf{h} - 2\mathbf{F}\mathbf{F}\mathbf{F} : \nabla \nabla \nabla U}{(\mathbf{F} \cdot \mathbf{F})^3} + \frac{2M^2}{(\mathbf{F} \cdot \mathbf{F})^4},$$

where $\mathbf{F} = -\nabla U$ is the molecular force, $M \equiv 2\mathbf{F} \cdot \nabla \nabla U \cdot \mathbf{F}$, $\mathbf{h} = 2\nabla \nabla U \cdot \mathbf{F}$, and the “:” denotes the triple dot product between two tensors of order three. For the microcanonical ensemble, we add $-(\frac{1}{2}N_f - 1)/(E_{\text{tot}} - U)^2$ to the formula.

For the volume distribution, $\mathbf{v} \cdot \nabla \rightarrow \partial/\partial V$, $f_V = N/V - \beta \partial U/\partial V$, and

$$\mathbf{v}_V \cdot \nabla f_V = \frac{\partial f_V}{\partial V} = -\frac{N}{V^2} - \frac{\beta \partial^2 U}{\partial V^2} = -\frac{N}{V^2} - \frac{\beta \sum_{(m,n)} [\psi(r_{mn}) r_{mn}^4 - \phi(r_{mn}) r_{mn}^2]}{9V^2},$$

where we have assumed the potential energy U is a sum over particle pairs (m, n) for the pair potential $u(r)$, i.e., $U = \sum_{(m,n)} u(r_{mn})$, and $\phi(r) = u'(r)/r$, $\psi(r) = \phi'(r)/r$.

For the radial distribution function of a pair of particles 1 and 2,

$$\mathbf{v}_r \cdot \nabla f_r = -\beta[\psi(r_{12})r_{12}^2 + \phi(r_{12})] - \beta \sum_{k \neq 1,2} \left[\frac{\psi(r_{1k})(\mathbf{r}_{1k} \cdot \mathbf{r}_{12})^2 + \psi(r_{2k})(\mathbf{r}_{2k} \cdot \mathbf{r}_{12})^2}{4r_{12}^2} + \frac{\phi(r_{1k}) + \phi(r_{2k})}{4} \right],$$

where \mathbf{r}_{jk} is the displacement vector from k to j , and $r_{jk} = |\mathbf{r}_{jk}|$.

4.5.3. Switched Lennard-Jones potential

The Lennard-Jones potential $u(r) = 4\varepsilon[(\sigma/r)^{12} - (\sigma/r)^6]$ is switched at $r = r_s$ to a polynomial $\sum_{k=4}^7 a_k (r - r_c)^k$ and extended to zero at $r = r_c$. For simplicity, we assume the reduced unit, whereby both the energy unit ε and diameter σ are 1.0. In the example of the energy distribution, we need the potential and the first three derivatives to be continuous, since the derivative of the dynamic temperature requires up to the third-order derivative of the potential. The continuity at $r = r_c$ is guaranteed by the first four vanishing coefficients. To ensure the continuity up to third-order derivatives at $r = r_s$, we used

$$\begin{aligned} a_4 &= 4(35 r_s^3 A + 90 r_s^2 \Delta r B + 15 r_s \Delta r^2 C + 28 \Delta r^3 D) / (\Delta r^4 r_s^{15}), \\ a_5 &= -24(14 r_s^3 A + 39 r_s^2 \Delta r B + 7 r_s \Delta r^2 C + 14 \Delta r^3 D) / (\Delta r^5 r_s^{15}), \\ a_6 &= 4(70 r_s^3 A + 204 r_s^2 \Delta r B + 39 r_s \Delta r^2 C + 84 \Delta r^3 D) / (\Delta r^6 r_s^{15}), \\ a_7 &= -16(5 r_s^3 A + 15 r_s^2 \Delta r B + 3 r_s \Delta r^2 C + 7 \Delta r^3 D) / (\Delta r^7 r_s^{15}), \end{aligned}$$

where, $\Delta r = r_c - r_s$, $A = 1 - r_s^6$, $B = 2 - r_s^6$, $C = 26 - 7r_s^6$, $D = 13 - 2r_s^6$.

4.5.4. Reference distributions

In each of Sections 4.3.1, 4.3.2, and 4.3.3, we prepared both the test and reference samples from the same trajectory but with different sampling rates of

picking frames. Since frames in the test sample were just a subset of those in the reference one, any inaccuracy due to insufficient sampling, would be shared by both samples, and thus would not affect the comparison of methods.

We have used the fractional identity to produce the reference distributions, in Figs. 4.2, 4.3, and 4.4. But due to the large size of the reference sample, the distributions were insensitive to method we choose. In Fig. 4.6, we show that the results from the fractional identity agreed well with the properly normalized histograms, as well as those from alternative identities, compare Figs. 4.2 with 4.6(a), 4.3 with 4.6(b), and 4.4 with 4.6(c)-(d). The latter comparison also shows the alternative identities are unbiased, although less stable in handling smaller samples. We also used the WHAM version in producing the reference distribution in Fig. 4.2(a), which further improved over the one in Fig. 4.6(a) at the edges.

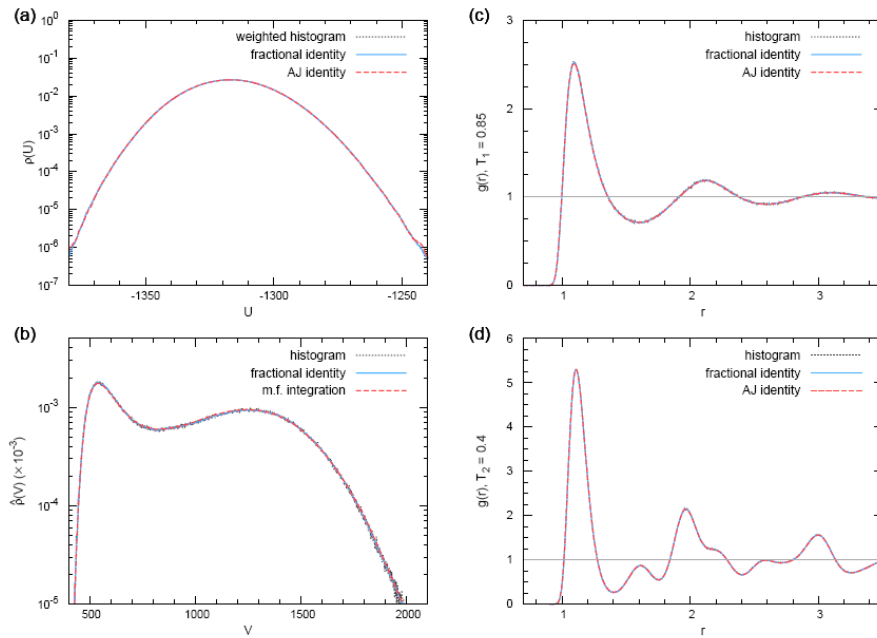


Figure 4.6. Distributions from the reference samples. (a) Potential-energy distributions; (b) volume distributions; (c) and (d) radial distribution functions at $T_1 = 0.85$ and $T_2 = 0.4$.

REFERENCES

1. Berendsen, H.J.C. and D. Van Der Spoel, *GROMACS: A message-passing parallel molecular dynamics implementation*. Computer Physics Communications, 1995. **91**(1-3): p. 43-56.
2. Lindahl, E., B. Hess, and D. van der Spoel, *GROMACS 3.0: A package for molecular simulation and trajectory analysis*. Journal of Molecular Modeling, 2001. **7**: p. 306-317.
3. Van Der Spoel, D., et al., *GROMACS: fast, flexible, and free*. Journal of Computational Chemistry, 2005. **26**(16): p. 1701-18.
4. Hess, B., et al., *GROMACS 4: Algorithms for Highly Efficient, Load-Balanced, and Scalable Molecular Simulation*. Journal of Chemical Theory and Computation, 2008. **4**(3): p. 435-447.
5. Humphrey, W., A. Dalke, and K. Schulten, *VMD: Visual molecular dynamics*. Journal of Molecular Graphics, 1996. **14**(1): p. 33-38.
6. Landau, L.D. and E.M. Lifshits, *Statistical Physics*. 3rd ed. Course of theoretical physics. 1980, Oxford: Pergamon Press.
7. Ma, S.-K., *Statistical Mechanics*. 1985, Philadelphia: World Scientific.
8. McQuarrie, D.A., *Statistical mechanics*. Harper's chemistry series. 1975, New York: Harper & Row.
9. Chandler, D., *Introduction to Modern Statistical Mechanics*. 1987, New York: Oxford University Press.
10. Frenkel, D. and B. Smit, *Understanding Molecular Simulation From Algorithms to Applications*. Second ed. Computational Science Series, ed. D. Frenkel, et al. Vol. 1. 2002: Academic Press.
11. Newman, M.E.J. and G.T. Barkema, *Monte Carlo Methods in Statistical Physics*. 1999, Oxford: Oxford University Press.
12. Rugh, H.H., *A dynamical approach to temperature* Physical Review Letters, 1997. **78**: p. 772-774.
13. Butler, B.D., et al., *Configurational temperature: Verification of Monte Carlo simulations*. The Journal of Chemical Physics, 1998. **109**(16): p. 6519-6522.

14. Ferdinand, A.E. and M.E. Fisher, *Bounded and Inhomogeneous Ising Models .I. Specific-heat Anomaly of a Finite Lattice*. Physical Review, 1969. **185**: p. 832-846.
15. Bussi, G., D. Donadio, and M. Parrinello, *Canonical sampling through velocity rescaling*. The Journal of Chemical Physics, 2007. **126**(1): p. 014101.
16. Metropolis, N., et al., *Equation of state calculations by fast computing machines*. The Journal of Chemical Physics, 1953. **21**: p. 1087-1092.
17. Swendsen, R.H. and J.S. Wang, *Nonuniversal Critical-Dynamics in Monte-Carlo Simulations*. Physical Review Letters, 1987. **58**(2): p. 86-88.
18. Wolff, U., *Collective Monte-Carlo Updating for Spin Systems*. Physical Review Letters, 1989. **62**(4): p. 361-364.
19. Manousiouthakis, V.I. and M.W. Deem, *Strict detailed balance is unnecessary in Monte Carlo simulation*. The Journal of Chemical Physics, 1999. **110**(6): p. 2753-2756.
20. Swendsen, R.H. and J.S. Wang, *Replica Monte-Carlo Simulation of Spin-Glasses*. Physical Review Letters, 1986. **57**(21): p. 2607-2609.
21. Geyer, C.J., *Proceedings of the 23rd Symposium on the Interface*. Markov chain Monte Carlo maximum likelihood, ed. E.M. Keramidas. 1991, New York: American Statistical Association.
22. Hukushima, K. and K. Nemoto, *Exchange Monte Carlo method and application to spin glass simulations*. Journal of the Physical Society of Japan, 1996. **65**(6): p. 1604-1608.
23. Hansmann, U.H.E., *Parallel tempering algorithm for conformational studies of biological molecules*. Chemical Physics Letters, 1997. **281**(1-3): p. 140-150.
24. Lyubartsev, A.P., et al., *New Approach to Monte-Carlo Calculation of the Free-Energy - Method of Expanded Ensembles*. The Journal of Chemical Physics, 1992. **96**(3): p. 1776-1783.
25. Marinari, E. and G. Parisi, *Simulated Tempering - a New Monte-Carlo Scheme*. Europhysics Letters, 1992. **19**(6): p. 451-458.
26. Park, S., *Comparison of the serial and parallel algorithms of generalized ensemble simulations: An analytical approach*. Physical Review E, 2008. **77**(1): p. -.

27. Zhang, C. and J. Ma, *Comparison of sampling efficiency between simulated tempering and replica exchange*. The Journal of Chemical Physics, 2008. **129**(13): p. 134112.
28. Wang, F.G. and D.P. Landau, *Efficient, multiple-range random walk algorithm to calculate the density of states*. Physical Review Letters, 2001. **86**(10): p. 2050-2053.
29. Zhang, C. and J. Ma, *Simulation via direct computation of partition functions*. Physical Review E, 2007. **76**: p. 036708.
30. Onuchic, J.N., Z. Luthey-Schulten, and P.G. Wolynes, *Theory of protein folding: the energy landscape perspective*. Annual Review of Physical Chemistry, 1997. **48**: p. 545-600.
31. Daggett, V. and A. Fersht, *The present view of the mechanism of protein folding*. Nat Rev Mol Cell Biol, 2003. **4**(6): p. 497-502.
32. Kubelka, J., J. Hofrichter, and W.A. Eaton, *The protein folding 'speed limit'*. Current Opinion in Structural Biology, 2004. **14**(1): p. 76-88.
33. Scheraga, H.A., M. Khalili, and A. Liwo, *Protein-folding dynamics: overview of molecular simulation techniques*. Annual Review of Physical Chemistry, 2007. **58**: p. 57-83.
34. Dill, K.A., et al., *The protein folding problem: when will it be solved?* Current Opinion in Structural Biology, 2007. **17**(3): p. 342-6.
35. Thirumalai, D., et al., *Theoretical perspectives on protein folding*. Annual Review of Biophysics, 2010. **39**: p. 159-83.
36. Duan, Y. and P.A. Kollman, *Pathways to a protein folding intermediate observed in a 1-microsecond simulation in aqueous solution*. Science, 1998. **282**(5389): p. 740-4.
37. Seibert, M.M., et al., *Reproducible polypeptide folding and structure prediction using molecular dynamics simulations*. Journal of Molecular Biology, 2005. **354**(1): p. 173-83.
38. Ensign, D.L., P.M. Kasson, and V.S. Pande, *Heterogeneity even at the speed limit of folding: large-scale molecular dynamics study of a fast-folding variant of the villin headpiece*. Journal of Molecular Biology, 2007. **374**(3): p. 806-16.
39. Juraszek, J. and P.G. Bolhuis, *Rate constant and reaction coordinate of Trp-cage folding in explicit water*. Biophysical Journal, 2008. **95**(9): p. 4246-57.

40. Kannan, S. and M. Zacharias, *Folding simulations of Trp-cage mini protein in explicit solvent using biasing potential replica-exchange molecular dynamics simulations*. Proteins, 2009. **76**(2): p. 448-60.
41. Freddolino, P.L. and K. Schulten, *Common structural transitions in explicit-solvent simulations of villin headpiece folding*. Biophysical Journal, 2009. **97**(8): p. 2338-47.
42. Zhang, C. and J. Ma, *Enhanced sampling and applications in protein folding in explicit solvent*. The Journal of Chemical Physics, 2010. **132**(24): p. 244101.
43. Shaw, D.E., et al., *Atomic-level characterization of the structural dynamics of proteins*. Science, 2010. **330**(6002): p. 341-6.
44. Best, R.B. and J. Mittal, *Balance between alpha and beta structures in ab initio protein folding*. The Journal of Physical Chemistry B, 2010. **114**(26): p. 8790-8.
45. Day, R., D. Paschek, and A.E. Garcia, *Microsecond simulations of the folding/unfolding thermodynamics of the Trp-cage miniprotein*. Proteins, 2010. **78**(8): p. 1889-1899.
46. Ikebe, J., et al., *Ab initio simulation of a 57-residue protein in explicit solvent reproduces the native conformation in the lowest free-energy cluster*. Protein Science, 2011. **20**(1): p. 187-96.
47. Lindorff-Larsen, K., et al., *How fast-folding proteins fold*. Science, 2011. **334**(6055): p. 517-20.
48. Liu, Y., et al., *Structural Characterization of λ -Repressor Folding from All-Atom Molecular Dynamics Simulations*. The Journal of Physical Chemistry Letters, 2012: p. 1117-1123.
49. Bowman, G.R., V.A. Voelz, and V.S. Pande, *Atomistic Folding Simulations of the Five-Helix Bundle Protein λ 6-85*. Journal of the American Chemical Society, 2011. **133**(4): p. 664-667.
50. Kyte, J. and R.F. Doolittle, *A simple method for displaying the hydrophobic character of a protein*. Journal of Molecular Biology, 1982. **157**(1): p. 105-132.
51. Li, H., M. Fajer, and W. Yang, *Simulated scaling method for localized enhanced sampling and simultaneous "alchemical" free energy simulations: a general method for molecular mechanical, quantum mechanical, and quantum mechanical/molecular mechanical simulations*. The Journal of Chemical Physics, 2007. **126**(2): p. 024106.

52. Gao, Y.Q., *An integrate-over-temperature approach for enhanced sampling*. The Journal of Chemical Physics, 2008. **128**(6): p. 064105.
53. Zhang, C. and J. Ma, *Enhanced sampling in generalized ensemble with large gap of sampling parameter: case study in temperature space random walk*. The Journal of Chemical Physics, 2009. **130**(19): p. 194112.
54. Ferrenberg, A.M. and R.H. Swendsen, *New Monte-Carlo Technique for Studying Phase-Transitions*. Physical Review Letters, 1988. **61**(23): p. 2635-2638.
55. Ferrenberg, A.M. and R.H. Swendsen, *Optimized Monte-Carlo Data-Analysis*. Physical Review Letters, 1989. **63**(12): p. 1195-1198.
56. Chodera, J.D., et al., *Use of the weighted histogram analysis method for the analysis of simulated and parallel tempering simulations*. Journal of Chemical Theory and Computation, 2007. **3**(1): p. 26-41.
57. Beale, P.D., *Exact distribution of energies in the two-dimensional ising model*. Physical Review Letters, 1996. **76**(1): p. 78-81.
58. Sorin, E.J. and V.S. Pande, *Exploring the helix-coil transition via all-atom equilibrium ensemble simulations*. Biophys. J., 2005. **88**(4): p. 2472-93.
59. Jorgensen, W.L., et al., *Comparison of simple potential functions for simulating liquid water*. The Journal of Chemical Physics, 1983. **79**(2): p. 926-935.
60. Essmann, U., et al., *A smooth particle mesh Ewald method*. The Journal of Chemical Physics, 1995. **103**(19): p. 8577-8593.
61. Miyamoto, S. and P.A. Kollman, *Settle: An analytical version of the SHAKE and RATTLE algorithm for rigid water models*. Journal of Computational Chemistry, 1992. **13**(8): p. 952-962.
62. Hess, B., *P-LINCS: A Parallel Linear Constraint Solver for Molecular Simulation*. Journal of Chemical Theory and Computation, 2008. **4**(1): p. 116-122.
63. Cochran, A.G., N.J. Skelton, and M.A. Starovasnik, *Tryptophan zippers: stable, monomeric beta -hairpins*. Proceedings of the National Academy of Sciences, 2001. **98**(10): p. 5578-83.
64. Zhang, J., M. Qin, and W. Wang, *Folding mechanism of beta-hairpins studied by replica exchange molecular simulations*. Proteins, 2006. **62**(3): p. 672-85.
65. Pitera, J.W., I. Haque, and W.C. Swope, *Absence of reptation in the high-temperature folding of the trpzip2 beta-hairpin peptide*. The Journal of Chemical Physics, 2006. **124**(14): p. 141102.

66. Yang, L., Q. Shao, and Y.Q. Gao, *Thermodynamics and folding pathways of trpzip2: an accelerated molecular dynamics simulation study*. The Journal of Physical Chemistry B, 2009. **113**(3): p. 803-8.
67. Snow, C.D., et al., *Trp zipper folding kinetics by molecular dynamics and temperature-jump spectroscopy*. Proceedings of the National Academy of Sciences, 2004. **101**(12): p. 4077-82.
68. Ulmschneider, J.P., M.B. Ulmschneider, and A. Di Nola, *Monte Carlo vs molecular dynamics for all-atom polypeptide folding simulations*. The Journal of Physical Chemistry B, 2006. **110**(33): p. 16733-42.
69. Roitberg, A.E., A. Okur, and C. Simmerling, *Coupling of replica exchange simulations to a non-Boltzmann structure reservoir*. The Journal of Physical Chemistry B, 2007. **111**(10): p. 2415-8.
70. Chen, C. and Y. Xiao, *Observation of multiple folding pathways of beta-hairpin trpzip2 from independent continuous folding trajectories*. Bioinformatics, 2008. **24**(5): p. 659-65.
71. Yang, W.Y., et al., *Heterogeneous folding of the trpzip hairpin: full atom simulation and experiment*. Journal of Molecular Biology, 2004. **336**(1): p. 241-51.
72. Hornak, V., et al., *Comparison of multiple Amber force fields and development of improved protein backbone parameters*. Proteins, 2006. **65**(3): p. 712-25.
73. Wang, J., P. Cieplak, and P.A. Kollman, *How Well Does a Restrained Electrostatic Potential (RESP) Model Perform in Calculating Conformational Energies of Organic and Biological Molecules?* Journal of Computational Chemistry, 2000. **21**(12): p. 1049.
74. McQuarrie, D.A., *Statistical Mechanics*. Harper's chemistry series. 1976, New York: Harper & Row.
75. Neidigh, J.W., R.M. Fesinmeyer, and N.H. Andersen, *Designing a 20-residue protein*. Nat Struct Biol, 2002. **9**(6): p. 425-30.
76. Qiu, L., et al., *Smaller and faster: the 20-residue Trp-cage protein folds in 4 micros*. Journal of the American Chemical Society, 2002. **124**(44): p. 12952-3.
77. Zhou, R., *Trp-cage: folding free energy landscape in explicit water*. Proceedings of the National Academy of Sciences, 2003. **100**(23): p. 13280-5.
78. Paschek, D., S. Hempel, and A.E. Garcia, *Computing the stability diagram of the Trp-cage miniprotein*. Proceedings of the National Academy of Sciences, 2008. **105**(46): p. 17754-9.

79. Juraszek, J. and P.G. Bolhuis, *Sampling the multiple folding mechanisms of Trp-cage in explicit solvent*. Proceedings of the National Academy of Sciences, 2006. **103**(43): p. 15859-64.
80. Yang, L., M.P. Grubb, and Y.Q. Gao, *Application of the accelerated molecular dynamics simulations to the folding of a small protein*. The Journal of Chemical Physics, 2007. **126**(12): p. 125102.
81. Simmerling, C., B. Strockbine, and A.E. Roitberg, *All-atom structure prediction and folding simulations of a stable protein*. Journal of the American Chemical Society, 2002. **124**(38): p. 11258-9.
82. Chowdhury, S., et al., *Ab initio folding simulation of the Trp-cage mini-protein approaches NMR resolution*. Journal of Molecular Biology, 2003. **327**(3): p. 711-7.
83. Snow, C.D., B. Zagrovic, and V.S. Pande, *The Trp cage: folding kinetics and unfolded state topology via molecular dynamics simulations*. Journal of the American Chemical Society, 2002. **124**(49): p. 14548-9.
84. Pitera, J.W. and W. Swope, *Understanding folding and design: replica-exchange simulations of "Trp-cage" miniproteins*. Proceedings of the National Academy of Sciences, 2003. **100**(13): p. 7587-92.
85. Streicher, W.W. and G.I. Makhatadze, *Unfolding thermodynamics of Trp-cage, a 20 residue miniprotein, studied by differential scanning calorimetry and circular dichroism spectroscopy*. Biochemistry, 2007. **46**(10): p. 2876-80.
86. Chiu, T.K., et al., *High-resolution x-ray crystal structures of the villin headpiece subdomain, an ultrafast folding protein*. Proceedings of the National Academy of Sciences, 2005. **102**(21): p. 7517-22.
87. Jayachandran, G., V. Vishal, and V.S. Pande, *Using massively parallel simulation and Markovian models to study protein folding: Examining the dynamics of the villin headpiece*. The Journal of Chemical Physics, 2006. **124**: p. 164902.
88. Lei, H. and Y. Duan, *Two-stage folding of HP-35 from ab initio simulations*. Journal of Molecular Biology, 2007. **370**(1): p. 196-206.
89. Snow, C.D., et al., *Absolute comparison of simulated and experimental protein-folding dynamics*. Nature, 2002. **420**(6911): p. 102-6.
90. Shen, M.Y. and K.F. Freed, *All-atom fast protein folding simulations: the villin headpiece*. Proteins, 2002. **49**(4): p. 439-45.

91. Zagrovic, B., et al., *Simulation of folding of a small alpha-helical protein in atomistic detail using worldwide-distributed computing*. Journal of Molecular Biology, 2002. **323**(5): p. 927-37.
92. Kubelka, J., W.A. Eaton, and J. Hofrichter, *Experimental tests of villin subdomain folding simulations*. Journal of Molecular Biology, 2003. **329**(4): p. 625-30.
93. Wang, M., et al., *Dynamic NMR line-shape analysis demonstrates that the villin headpiece subdomain folds on the microsecond time scale*. Journal of the American Chemical Society, 2003. **125**(20): p. 6032-3.
94. Duan, Y., et al., *A point-charge force field for molecular mechanics simulations of proteins based on condensed-phase quantum mechanical calculations*. Journal of Computational Chemistry, 2003. **24**(16): p. 1999-2012.
95. Berg, B.A. and W. Janke, *Wang-Landau multibondic cluster simulations for second-order phase transitions*. Physical Review Letters, 2007. **98**(4): p. 040602
96. Freddolino, P.L., et al., *Force field bias in protein folding simulations*. Biophysical Journal, 2009. **96**(9): p. 3772-80.
97. Kampen, N.G.v., *Stochastic processes in physics and chemistry*. 3rd ed. North-Holland personal library. 2007, Amsterdam ; Boston: Elsevier.
98. Zhang, C. and J. Ma, *Folding helical proteins in explicit solvent using dihedral-biased tempering*. Proceedings of the National Academy of Sciences, 2012. **109**(21): p. 8139-8144.
99. Zhou, Y. and M. Karplus, *Folding of a model three-helix bundle protein: a thermodynamic and kinetic analysis*. Journal of Molecular Biology, 1999. **293**(4): p. 917-51.
100. Jang, S., S. Shin, and Y. Pak, *Replica-exchange method using the generalized effective potential*. Physical Review Letters, 2003. **91**(5): p. 058305.
101. Bryson, J.W., et al., *From coiled coils to small globular proteins: design of a native-like three-helix bundle*. Protein Science, 1998. **7**(6): p. 1404-14.
102. Walsh, S.T., et al., *Solution structure and dynamics of a de novo designed three-helix bundle protein*. Proceedings of the National Academy of Sciences, 1999. **96**(10): p. 5486-91.
103. Johansson, J.S., et al., *A Native-Like Three-Alpha-Helix Bundle Protein from Structure-Based Redesign: A Novel Maquette Scaffold*. Journal of the American Chemical Society, 1998. **120**(16): p. 3881-3886.

104. Dai, Q.H., et al., *Structure of a de novo designed protein model of radical enzymes*. J Am Chem Soc, 2002. **124**(37): p. 10952-3.
105. Ramboarina, S., et al., *Structural insights into serine-rich fimbriae from Gram-positive bacteria*. Journal of Biological Chemistry, 2010. **285**(42): p. 32446-57.
106. Go, A., et al., *Structure and dynamics of de novo proteins from a designed superfamily of 4-helix bundles*. Protein Science, 2008. **17**(5): p. 821-32.
107. Best, R.B. and G. Hummer, *Optimized molecular dynamics force fields applied to the helix-coil transition of polypeptides*. The Journal of Physical Chemistry B, 2009. **113**(26): p. 9004-15.
108. Yang, J.S., et al., *All-atom ab initio folding of a diverse set of proteins*. Structure, 2007. **15**(1): p. 53-63.
109. Meinke, J.H. and U.H. Hansmann, *Free-energy-driven folding and thermodynamics of the 67-residue protein GS-alpha3W--a large-scale Monte Carlo study*. Journal of Computational Chemistry, 2009. **30**(11): p. 1642-8.
110. Czaplewski, C., et al., *Application of Multiplexed Replica Exchange Molecular Dynamics to the UNRES Force Field: Tests with alpha and alpha+beta Proteins*. Journal of Chemical Theory and Computation, 2009. **5**(3): p. 627-640.
111. Antonyuk, S.V., et al., *Carbon monoxide poisoning is prevented by the energy costs of conformational changes in gas-binding haemproteins*. Proceedings of the National Academy of Sciences, 2011. **108**(38): p. 15780-15785.
112. Arnesano, F., et al., *The solution structure of oxidized Escherichia coli cytochrome b562*. Biochemistry, 1999. **38**(27): p. 8657-70.
113. Vakonakis, I., et al., *Solution structure and sugar-binding mechanism of mouse latrophilin-1 RBL: a 7TM receptor-attached lectin-like domain*. Structure, 2008. **16**(6): p. 944-53.
114. Booth, V., et al., *Structure of a conserved domain common to the transcription factors TFIIIS, elongin A, and CRSP70*. Journal of Biological Chemistry, 2000. **275**(40): p. 31266-8.
115. Levy, Y., et al., *Symmetry and frustration in protein energy landscapes: A near degeneracy resolves the Rop dimer-folding mystery*. Proceedings of the National Academy of Sciences, 2005. **102**(7): p. 2373-2378.
116. Schug, A., et al., *Mutations as trapdoors to two competing native conformations of the Rop-dimer*. Proceedings of the National Academy of Sciences, 2007. **104**(45): p. 17674-17679.

117. Gambin, Y., et al., *Direct single-molecule observation of a protein living in two opposed native structures*. Proceedings of the National Academy of Sciences, 2009. **106**(25): p. 10153-10158.
118. Baltzer, L., H. Nilsson, and J. Nilsson, *De novo design of proteins--what are the rules?* Chem Rev, 2001. **101**(10): p. 3153-63.
119. Kannan, S. and M. Zacharias, *Enhanced sampling of peptide and protein conformations using replica exchange simulations with a peptide backbone biasing-potential*. Proteins, 2007. **66**(3): p. 697-706.
120. Zhang, C. and J. Ma, *Estimating statistical distributions using an integral identity*. The Journal of Chemical Physics, 2012. **136**(20): p. 204113.
121. Adib, A.B. and C. Jarzynski, *Unbiased estimators for spatial distribution functions of classical fluids*. The Journal of Chemical Physics, 2005. **122**(1): p. 14114.
122. Ciccotti, G., R. Kapral, and E. Vanden-Eijnden, *Blue Moon Sampling, Vectorial Reaction Coordinates, and Unbiased Constrained Dynamics*. ChemPhysChem, 2005. **6**(9): p. 1809-1814.
123. Kim, J., T. Keyes, and J.E. Straub, *Communication: Iteration-free, weighted histogram analysis method in terms of intensive variables*. The Journal of Chemical Physics, 2011. **135**(6): p. 061103.
124. Jepps, O.G., G. Ayton, and D.J. Evans, *Microscopic expressions for the thermodynamic temperature*. Physical Review E, 2000. **62**(4 Pt A): p. 4757-63.
125. Yan, Q. and J.J. de Pablo, *Fast calculation of the density of states of a fluid by Monte Carlo simulations*. Physical Review Letters, 2003. **90**(3): p. 035701.
126. Braga, C. and K.P. Trivisa, *A configurational temperature Nosé-Hoover thermostat*. The Journal of Chemical Physics, 2005. **123**: p. 134101.
127. Adib, A.B., *Entropy and density of states from isoenergetic nonequilibrium processes*. Physical Review E, 2005. **71**(5 Pt 2): p. 056128.
128. Press, W.H., et al., *Numerical Recipes in C: the Art of Scientific Computing*. 2nd ed. 1992, Cambridge: Cambridge University Press.
129. Koper, G.J.M. and H. Reiss, *Length Scale for the Constant Pressure Ensemble: Application to Small Systems and Relation to Einstein Fluctuation Theory*. The Journal of Physical Chemistry, 1996. **100**(1): p. 422-432.

130. Berg, B.A. and R.C. Harris, *From data to probability densities without histograms*. Computer Physics Communications, 2008. **179**: p. 443-448.
131. van Zon, R. and J. Schofield, *Constructing smooth potentials of mean force, radial distribution functions, and probability densities from sampled data*. The Journal of Chemical Physics, 2010. **132**(15): p. 154110.
132. Basner, J.E. and C. Jarzynski, *Binless estimation of the potential of mean force*. The Journal of Physical Chemistry B, 2008. **112**(40): p. 12722-9.